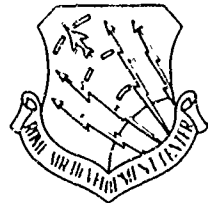
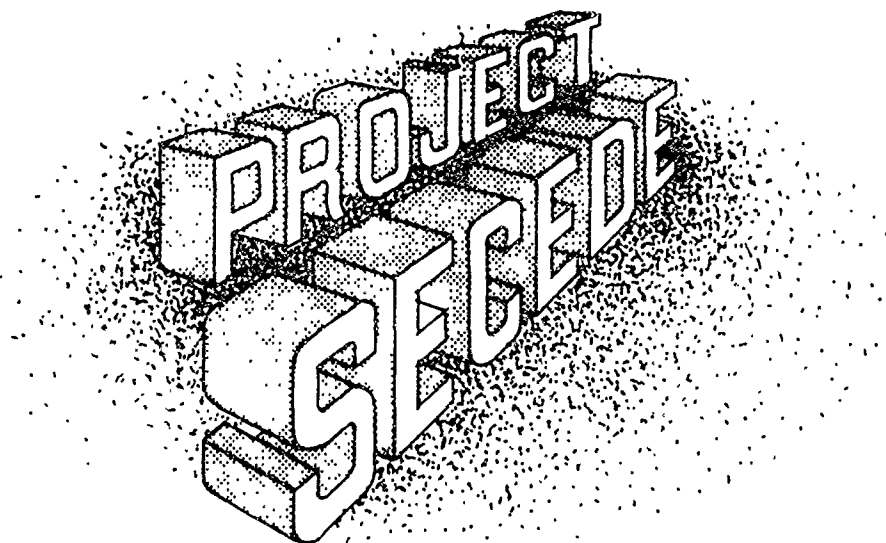


RADC-TR-71-313
Technical Report
March 1971



AD736040

Prepared By
Rome Air Development Center
Air Force Systems Command
Griffiss Air Force Base, New York 13440

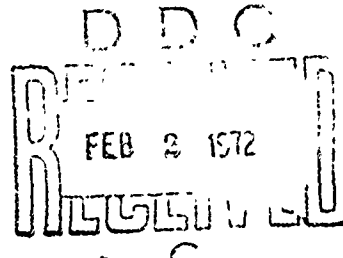


RAY TRACING SYNTHESIS OF HF RADAR SIGNATURES
FROM GAUSSIAN PLASMA CLOUDS

Raytheon Company, Sudbury Labs

Sponsored by
Advanced Research Projects Agency
ARPA Order No. 1057

Approved for public release;
distribution unlimited.



The views and conclusions contained in this document are those of the authors and should not be interpreted as necessarily representing the official policies, either expressed or implied, of the Advanced Research Projects Agency or the US Government.

UNCLASSIFIED

Security Classification

DOCUMENT CONTROL DATA - R&D

(Security classification of title, body of abstract and indexing annotation must be entered when the overall report is classified)

1 ORIGINATING ACTIVITY (Corporate author) RAYTHEON COMPANY, EQUIPMENT DEVELOPMENT LABORATORIES SUDSBURY, MASSACHUSETTS 01776	2a. REPORT SECURITY CLASSIFICATION UNCLASSIFIED
	2b. GROUP

3 REPORT TITLE

RAY TRACING SYNTHESIS OF HF RADAR SIGNATURES FROM GAUSSIAN PLASMA CLOUDS.

4 DESCRIPTIVE NOTES (Type of report and inclusive dates)

TECHNICAL REPORT NO. 3

5 AUTHOR(S) (Last name, first name, initial)

RAO, PENDYALA B.; ALLEN, E. MICHAEL; AND THOME, GEORGE D.

6. REPORT DATE MARCH 1971	7a. TOTAL NO. OF PAGES 92	7b. NO. OF REFS 13
8a. CONTRACT OR GRANT NO. F30602-68-C-0299	9a. ORIGINATOR'S REPORT NUMBER(S)	
b. PROJECT NO. ARPA ORDER NO. 1057	9b. OTHER REPORT NO(S) (Any other numbers that may be assigned this report) RADC-TR-71-313	
c.		
d.		

10. AVAILABILITY/LIMITATION NOTICES

APPROVED FOR PUBLIC RELEASE DISTRIBUTION UNLIMITED

11. SUPPLEMENTARY NOTES MONITORED BY JOSEPH J. SIMONS RADC OCSE, GRIFFISS AFB NY 13440	12. SPONSORING MILITARY ACTIVITY ADVANCED RESEARCH PROJECT AGENCY 1400 WILSON BOULEVARD ARLINGTON, VA 22209
13. ABSTRACT THE ELECTRON DENSITY DISTRIBUTION THROUGH IONIZED CLOUDS PRODUCED BY BARIUM RELEASES IS OFTEN TAKEN TO BE GAUSSIAN FOR WANT OF DIRECT EVIDENCE TO THE CONTRARY. MULTIPLE FREQUENCY HF RADAR OBSERVATIONS (SCATTERING CROSS-SECTION AND DOPPLER SHIFT VERSUS TIME) HAVE BEEN MADE DURING SEVERAL RELEASES FOR THE PRIMARY PURPOSE OF MEASURING PEAK ELECTRON DENSITY AS A FUNCTION OF TIME. OBSERVATIONS OF THIS SORT CANNOT BE USED TO COMPUTE THE ELECTRON DENSITY DISTRIBUTION DIRECTLY BECAUSE THE CLOUD ELONGATES ALONG THE EARTH'S MAGNETIC FIELD AND THUS THE DISTRIBUTION IS NOT ONE DIMENSIONAL. THESE OBSERVATIONS CAN HOWEVER BE USED TO TEST ASSUMED DISTRIBUTIONS BY RAY TRACING THROUGH A MODEL CLOUD AND COMPARING THE PREDICTED SIGNATURES WITH THE OBSERVATIONS. A DETAILED COMPARISON OF THIS NATURE HAS BEEN MADE USING A TIME-DEPENDENT GAUSSIAN CLOUD AND THE ITSA THREE-DIMENSIONAL RAY TRACING PROGRAM. THE RAY TRACING RESULTS HAVE BEEN COMPARED ALSO TO THAT OF A HARD EXPANDING ELLIPSOID MOD. - TO STUDY THE EFFECTS OF THE IONIZATION LYING BELOW THE REFLECTION LEVEL. SIGNIFICANT DIFFERENCES HAVE BEEN NOTED BETWEEN THE OBSERVED AND THE SYNTHESIZED SIGNATURES FROM THE RAY TRACING. THE DIFFERENCES ARE OF THE NATURE TO SUGGEST THAT THE ELECTRON DENSITY VARIATION OUTWARD FROM THE CENTER OF THE CLOUD IS MORE GRADUAL THAN THAT IN THE ADOPTED GAUSSIAN MODEL. DEFOCUSING DUE TO THE UNDERLYING IONIZATION IS FOUND TO REDUCE THE SCATTERING CROSS-SECTION BY A FACTOR THAT INCREASES WITH TIME FROM 3 AT THE PEAK CROSS-SECTION TO 30 JUST PRIOR TO SIGNAL DROP-OUT.	

DD FORM 1 JAN 64 1473

UNCLASSIFIED

Security Classification

UNCLASSIFIED

Security Classification

14 KEY WORDS	LINK A		LINK B		LINK C	
	ROLE	WT	ROLE	WT	ROLE	WT
THREE DIMENSIONAL RAY TRACING						
HF RADAR SIGNATURES						
GAUSSIAN PLASMA CLOUDS						
DOPPLER SHIFTS						
RADAR CROSS SECTIONS						
INSTRUCTIONS						
1. ORIGINATING ACTIVITY: Enter the name and address of the contractor, subcontractor, grantee, Department of Defense activity or other organization (<i>corporate author</i>) issuing the report.	imposed by security classification, using standard statements such as:					
2a. REPORT SECURITY CLASSIFICATION: Enter the overall security classification of the report. Indicate whether "Restricted Data" is included. Marking is to be in accordance with appropriate security regulations.	(1) "Qualified requesters may obtain copies of this report from DDC."					
2b. GROUP: Automatic downgrading is specified in DoD Directive 5200.10 and Armed Forces Industrial Manual. Enter the group number. Also, when applicable, show that optional markings have been used for Group 3 and Group 4 as authorized.	(2) "Foreign announcement and dissemination of this report by DDC is not authorized."					
3. REPORT TITLE: Enter the complete report title in all capital letters. Titles in all cases should be unclassified. If a meaningful title cannot be selected without classification, show title classification in all capitals in parenthesis immediately following the title.	(3) "U. S. Government agencies may obtain copies of this report directly from DDC. Other qualified DDC users shall request through _____."					
4. DESCRIPTIVE NOTES: If appropriate, enter the type of report, e.g., interim, progress, summary, annual, or final. Give the inclusive dates when a specific reporting period is covered.	(4) "U. S. military agencies may obtain copies of this report directly from DDC. Other qualified users shall request through _____."					
5. AUTHOR(S): Enter the name(s) of author(s) as shown on or in the report. Enter last name, first name, middle initial. If military, show rank and branch of service. The name of the principal author is an absolute minimum requirement.	(5) "All distribution of this report is controlled. Qualified DDC users shall request through _____."					
6. REPORT DATE: Enter the date of the report as day, month, year, or month, year. If more than one date appears on the report, use date of publication.	If the report has been furnished to the Office of Technical Services, Department of Commerce, for sale to the public, indicate this fact and enter the price, if known.					
7a. TOTAL NUMBER OF PAGES: The total page count should follow normal pagination procedures, i.e., enter the number of pages containing information.	11. SUPPLEMENTARY NOTES: Use for additional explanatory notes.					
7b. NUMBER OF REFERENCES: Enter the total number of references cited in the report.	12. SPONSORING MILITARY ACTIVITY: Enter the name of the departmental project office or laboratory sponsoring (<i>paying for</i>) the research and development. Include address.					
8a. CONTRACT OR GRANT NUMBER: If appropriate, enter the applicable number of the contract or grant under which the report was written.	13. ABSTRACT: Enter an abstract giving a brief and factual summary of the document indicative of the report, even though it may also appear elsewhere in the body of the technical report. If additional space is required, a continuation sheet shall be attached.					
8b, 8c, & 8d. PROJECT NUMBER: Enter the appropriate military department identification, such as project number, subproject number, system numbers, task number, etc.	It is highly desirable that the abstract of classified reports be unclassified. Each paragraph of the abstract shall end with an indication of the military security classification of the information in the paragraph, represented as (TS), (S), (C), or (U).					
9a. ORIGINATOR'S REPORT NUMBER(S): Enter the official report number by which the document will be identified and controlled by the originating activity. This number must be unique to this report.	There is no limitation on the length of the abstract. However, the suggested length is from 150 to 225 words.					
9b. OTHER REPORT NUMBER(S): If the report has been assigned any other report numbers (<i>either by the originator or by the sponsor</i>), also enter this number(s).	14. KEY WORDS: Key words are technically meaningful terms or short phrases that characterize a report and may be used as index entries for cataloging the report. Key words must be selected so that no security classification is required. Identifiers, such as equipment model designation, trade name, military project code name, geographic location, may be used as key words but will be followed by an indication of technical context. The assignment of links, rules, and weights is optional.					
10. AVAILABILITY/LIMITATION NOTICES: Enter any limitations on further dissemination of the report, other than those						

UNCLASSIFIED

Security Classification

RAY TRACING SYNTHESIS OF HF RADAR SIGNATURES
FROM GAUSSIAN PLASMA CLOUDS

Pendyala B. Rao
E. Michael Allen
George D. Thome

Contractor: Raytheon Company, Sudbury Labs
Contract Number: F30602-68-C-0299
Effective Date of Contract: 19 February 1968
Contract Expiration Date: 3 January 1972
Amount of Contract: \$640,251.000
Program Code Number: 8E20

Principal Investigator: Dr. George Thome
Phone: 617 443-9521-Ext 2203

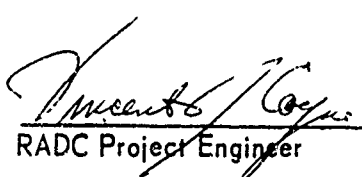
Project Engineer: Joseph J. Simons
Phone: 315 330-3451

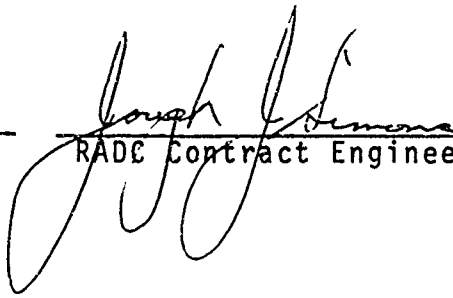
Approved for public release;
distribution unlimited.

This research was supported by the
Advanced Research Projects Agency
of the Department of Defense and
was monitored by Joseph J. Simons,
RADC (OCSE), GAFB, NY 13440 under
Contract F30602-68-C-0299.

PUBLICATION REVIEW

This technical report has been reviewed and is approved.


Francisco J. Coyle
RADC Project Engineer


Joseph L. Johnson
RADC Contract Engineer

ABSTRACT

The electron density distribution through ionized clouds produced by Barium releases is often taken to be Gaussian for want of direct evidence to the contrary. Multiple frequency hf radar observations (scattering cross-section and Doppler shift versus time) have been made during several releases for the primary purpose of measuring peak electron density as a function of time. Observations of this sort cannot be used to compute the electron density distribution directly because the cloud elongates along the Earth's magnetic field and thus the distribution is not one dimensional. These observations can however be used to test assumed distributions by ray tracing through a model cloud and comparing the predicted signatures with the observations. A detailed comparison of this nature has been made using a time-dependent Gaussian cloud and the ITSA three-dimensional ray tracing program. The ray tracing results have been compared also to that of a hard expanding ellipsoid model to study the effects of the ionization lying below the reflection level. Significant differences have been noted between the observed and the synthesized signatures from the ray tracing. The differences are of the nature to suggest that the electron density variation outward from the center of the cloud is more gradual than that in the adopted Gaussian model. Defocussing due to the underlying ionization is found to reduce the scattering cross-section by a factor that increases with time from 3 at the peak cross-section to 30 just prior to signal drop-out.

CONTENTS

<u>Section</u>		<u>Page</u>
	ABSTRACT	ii
	ILLUSTRATIONS	v
1	INTRODUCTION	1
2	THREE DIMENSIONAL RAY TRACING PROGRAM	4
2.1	Introduction	4
2.2	Governing Equations	4
2.3	Description of the Program	6
2.4	Application to Plasma Clouds	8
3	PLASMA CLOUD MODEL	10
3.1	Ambipolar Diffusion Model	10
3.2	Model Transformation to Geomagnetic Coordinate System	12
3.3	Ion Cloud Input Parameters	19
4	SYNTHESIS OF RADAR SIGNATURES	22
4.1	Ray Tracing Method	22
4.2	Hard Expanding Ellipsoid Method	30
4.3	Results and Discussion	37
5	EXPERIMENTAL RESULTS	59
5.1	Test Geometry and Instrumentation	59
5.2	Experimental Data	60
5.3	Results	66
6	COMPARISON BETWEEN EXPERIMENTAL AND RAY TRACING RESULTS	73
7	SUMMARY AND CONCLUSIONS	78

CONTENTS (CONTINUED)

<u>Appendix</u>		<u>Page</u>
A	GAUSS X ROUTINE AND SAMPLE RAY TRACE	81
B	A VECTOR METHOD TO CALCULATE CLOUD TRAJECTORY . .	85
ACKNOWLEDGMENTS	90
REFERENCES	91
DISTRIBUTION LIST		
DD 1473		

ILLUSTRATIONS

<u>Figure</u>	<u>Page</u>
3-1	Illustration to Show the Coordinate Transformation from Earth Centered Geomagnetic Dipole System (x_m , y_m , z_m) to Cloud Centered System (x , y , z). The Correspondence Between the Two Systems Requires One Translation and Two Rotations 13
3-2	The Trajectory, the Peak Electron Density and the Results from Microdensitometer Scans of the Filter Photographs of the Cloud. (Filled and Open Circles in the Trajectory Data Represent Determinations from Two Pairs of Optical Stations.) 20
4-1	Illustrates the Method for Determination of the 'Homing' Ray. A, B, C, D, etc., are the Ground Impact Points when a Bundle of Rays Incremented in Azimuth and Elevation are Transmitted 24
4-2	Geometry of an Electromagnetic Flux Tube Illuminating a Patch of Ground on Reflection from the Plasma Cloud 27
4-3	Illustration to Evaluate the Ranges R_1 and R_2 to the Reflection Point from the Transmitter and the Receiver 29
4-4	Coordinate System Adopted to Obtain an Expression for the Radar Cross-Section of the Ellipsoid 31
4-5	The Geometry to Express Unit Vector Normal to the Cloud Surface at the Specular Point from the Radar 33
4-6	Illustrate the Position of the Specular Point at Two Instants of Time to Calculate the Path Difference to it from the Radar 36
4-7	Illustrate the Limiting Process Involved in Obtaining the Doppler Shift from the Path Difference Calculation 38

ILLUSTRATIONS (CONTINUED)

<u>Figure</u>		<u>Page</u>
4-8	Ray Path Projection Plots in Both Vertical and Ground Planes at 100 Seconds After Release for the Three Modes, No Field, Ordinary and Extraordinary, at $F = 10.31$ MHz	39
4-9	The Vertical Ray Path Segments Close to the Reflection Level to Show How the Three Modes Refract through the Denser Regions of the Cloud	40
4-10a	The Azimuth and Elevation Angles of Transmission (ϕ_T, β_T) and Reflection Point (ϕ_R, β_R) for no field Ray at $F = 10.31$ MHz Along with that of the Cloud Center (ϕ_C, β_C)	42
4-10b	The Azimuth and Elevation Angles of Transmission (ϕ_T, β_T) and Reflection Point (ϕ_R, β_R) for Ordinary Ray at $F = 10.31$ MHz Along with that of the Center (ϕ_C, β_C)	43
4-10c	The Azimuth and Elevation Angles of Transmission (ϕ_T, β_T) and Reflection Point (ϕ_R, β_R) for Extraordinary Ray at $F = 10.31$ MHz Along with that of the Cloud Center (ϕ_C, β_C)	44
4-11a	The Azimuth and Elevation Angles of Transmission (ϕ_T, β_T) and Reflection Point (ϕ_R, β_R) for the Ordinary Ray at $F = 16.078$ MHz Along with that of the Cloud Center (ϕ_C, β_C)	45
4-11b	The Azimuth and Elevation Angles of Transmission (ϕ_T, β_T) and Reflection Point (ϕ_R, β_R) for the Extraordinary Ray at $F = 16.078$ MHz Along with that of the Cloud Center (ϕ_C, β_C)	46
4-12	The Azimuth and Elevation Angle Deviations Suffered by the Three Modes Due to Refraction Up to the Reflection Level at $F = 10.31$ MHz	47
4-13	Ray Path Projections in Vertical Plane of a Fine Bundle of Eleven Rays (Appears as Thick Line on the Plot) Transmitted Over an Elevation Scan Interval of 0.02 Degree. The Spread of the Rays on Reflection Illustrate the Defocussing Effects of the Cloud	48

ILLUSTRATIONS (CONTINUED)

<u>Figure</u>		<u>Page</u>
4-14	Ray Path Projections in Vertical Plane of a Fine Bundle of Eleven Rays (Appears as Thick Line on the Plot) Transmitted over an Azimuth Scan of Size 0.025 Degrees. The Spread of the Rays on Reflection Illustrate the Defocussing Effects of the Cloud	49
4-15	Ray Path Projections on the Ground Plane of a Fine Bundle of Eleven Rays (Thick Line on the Plot from TX) Scanned in Elevation by 0.02 Degree.	50
4-16	Ray Path Projections on the Ground Plane of a Fine Bundle of Eleven Rays (Thick Line on the Plot from TX) for an Azimuth Scan of Size 0.025 Degrees.	51
4-17	The Time History of the Doppler Shift and the Scattering Cross Section Synthesized by the Ray Tracing Method for No-Field, Ordinary and Extraordinary Modes at $F = 10.31$ MHz	53
4-18	The Time History of the Doppler Shift and the Scattering Cross Section Synthesized by the Ray Tracing Method for Ordinary and Extra-ordinary Modes at $F = 16.078$ MHz	54
4-19	The Time History of the Doppler Shift and the Scattering Cross Section Synthesized by the Hard Ellipsoid Method for $F = 10.31$ and 9.902 MHz. (The Two Frequencies Correspond to the Plasma Frequencies that Support the O and X Modes). . .	56
4-20	The Time History of the Doppler Shift and the Scattering Cross Section Synthesized by the Hard Ellipsoid Method for $F = 16.078$ and 15.673 MHz. (The Two Frequencies Correspond to the Plasma Frequencies that Support the O and X Modes). . .	57
5-1	Illustration to Show the Cloud Geometry with Respect to the Transmitting (TX) and Receiving (RX) Stations.	59
5-2	The Observed Doppler Signatures at $F = 10.31$ and 16.078 MHz for Test Mulberry	62

ILLUSTRATIONS (CONTINUED)

<u>Figure</u>		<u>Page</u>
5-3	Selected Scans of the Amplitude Spectra of the Signal at $F = 10.31$ MHz for Test Mulberry. (The Folding of the Spectral Components Lying Outside the Unambiguous Doppler Window Causes Images to Appear on the Display.)	63
5-4	Selected Scans of the Amplitude Spectra of the Signal at $F = 16.078$ MHz for Test Mulberry. (The Folding of the Spectral Components Lying Outside the Unambiguous Doppler Window Causes Images to Appear on the Display.)	64
5-5	The Calibration Curves Used to Convert the Arbitrary Units of Amplitude to Absolute Signal Power	65
5-6	The Amplitude (Arbitrary Scale) and the Power Variations of the Signal at 10.31 MHz. The Power Curve is Constructed from the Envelope of the Amplitude Plot. The Horizontal Dashed Lines Indicate the Average Noise and the Minimum Detectable Signal Levels	67
5-7	The Amplitude (Arbitrary Scale) and the Power Variations of the Signal at $F = 16.078$ MHz. The Power Curve is Constructed from the Envelope of the Amplitude Plot. The Horizontal Dashed Lines Indicate the Average Noise and the Minimum Detectable Signal Levels	68
5-8	The Variation with Time of the Ranges R_1 and R_2 to the Reflection Point Respectively from the Transmitter and Receiver	70
5-9	Time History of the Doppler Shift and the Scattering Cross Section Derived from the HF Measurements at $F = 10.31$ MHz	71
5-10	Time History of the Doppler Shift and the Scattering Cross Section Derived from the HF Measurements at $F = 16.078$ MHz	72

ILLUSTRATIONS (CONTINUED)

<u>Figure</u>		<u>Page</u>
6-1	The Doppler Shift Associated with the Drift of the Plasma Cloud for $F = 10.31$ and 16.078 MHz. . .	73
6-2	Comparison Between the Experimental and the Synthesized Time Histories of the Doppler Shift and the Scattering Cross Section at $F = 10.31$ MHz.	75
6-3	Comparison Between the Experimental and the Synthesized Time Histories of the Doppler Shift and the Scattering Cross Section at $F = 16.078$ MHz	76

SECTION 1. INTRODUCTION

The generation of artificial ion clouds in the upper atmosphere has proven to be a useful technique for studying plasma interaction with the electric and magnetic field environment of the Earth's ionosphere and magnetosphere. The technique, originally developed at the Max Planck Institute in Germany, employs rocket releases of Barium vapor which, on being exposed to the solar ultraviolet radiation, becomes partially ionized (Haerendel and Lust, 1969). The ionized and the non-ionized components of the Barium vapor form into two distinct clouds, an ion and a neutral cloud. A number of radio and optical methods have been devised to study the following characteristics of the clouds:

- a. Size, shape, particle number densities and their distributions as a function of time
- b. Diffusion and drift motions including the dynamics associated with the gross deformation and the striated structure exhibited by the ion cloud
- c. Radio wave scattering in the hf and vhf regimes.

The knowledge of the electron (ion) density distribution in the ionized cloud is of fundamental importance for a proper understanding of the ion cloud interaction with the ionospheric environment. There have not been as yet any reliable experimental measurements that would directly provide this information. Some evidence has been gathered, however, which tends to suggest a Gaussian profile for the distribution. First, the Gaussian model has stemmed out of the theoretical work of Holway (1965) which is based on the ambipolar diffusion of the cloud in the geomagnetic field neglecting the presence of an external electric field. In a recent study by Simon (1970), it

was shown that taking the electric field into account would still lead to a Gaussian distribution, but in a transformed drift frame of reference. The experimental evidence that seems to favor the Gaussian model is derived from the optical intensity measurements of the resonant scattering and the Thomson scatter radar observations. The deductions from optical measurements are made by microdensitometer scans of the filter photographs of the cloud. The variations of the line integral of the ions along selected scans are found to fit well to Gaussian distributions. It does not, however, follow immediately that the ion density distribution itself is Gaussian. Thomson scatter radar observations provide electron density profiles along the antenna beam direction with a spatial resolution defined by the pulse length and temporal resolution determined by the integration time. The electron density profiles measured by this technique using the AIO radar during one of the SECEDE I tests suggest that the distribution is at least approximately Gaussian. The measurements with a resolution of 2 km are rather coarse, however, with respect to the cloud dimensions and are subject to the uncertainties involved due to possible energy leakage through the sidelobes. Further evidence in support of the Gaussian distribution has come from an analysis by Oetzel and Chang (1969) who found that the observed Faraday fading and the history of the center point electron density derived from hf measurements are consistent to a greater extent with the Gaussian model than with other distributions.

In spite of all the positive evidence in support of the Gaussian model, the true distribution is still a matter of speculation because of an unexpected behavior of the hf Doppler. It is expected that an expanding Gaussian cloud will lead to a Doppler trace that goes negative shortly before the signal dropout on a given operating frequency. The observed Doppler records, however, exhibit no such negative tail.

For this to occur, two possibilities suggest themselves immediately: one, of course, is that the distribution is unlike Gaussian, and the other, which seems more probable, is that the signal is too weak to be detected during the contracting phase of a given plasma frequency contour, thus washing off the expected negative tail.

The problem taken up in this report is to investigate the two possibilities by synthesizing the radar signatures both in Doppler and signal strength by means of a three dimensional ray tracing program and Gaussian modeled ion clouds. The results will show to what extent the sensitivity of the receiving system limits the Doppler trace, and how accurately a Gaussian model could simulate an ion cloud. The 3-D ray tracing program used here was developed at ESSA by Dr. R.M. Jones and has proven to be quite versatile in its scope. A summary description of this program is given in Section 2. Section 3 deals with the ion cloud modeling in the geomagnetic dipole coordinate system as desired by the ray tracing program. The results of the ray tracing are presented in Section 4 along with those derived for the case of an expanding hard ellipsoid model. Experimental results are described in Section 5. Section 6 is devoted to a comparison between the theory and observations with the summary and conclusions given in Section 7.

SECTION 2. THREE DIMENSIONAL RAY TRACING PROGRAM

2.1 INTRODUCTION

A versatile computer program for tracing rays through a medium whose index of refraction varies in three dimensions has been developed by R. M. Jones at ESSA Laboratories in Boulder. The program was intended for ray tracing applications in the ionosphere and could successfully simulate a variety of radio propagation experiments. It was written in FORTRAN language and was made available on request to prospective users in two versions; one to run on a CDC 3600 and the other on an IBM 7090. A detailed description of the program along with instructions that include annotated listings of all routines, deck set-ups and the form of input and output has been published in the ESSA reports by Jones (1966, 1968). The efficiency of the program in computing the rays has been evaluated by Lemanski (1968).

2.2 GOVERNING EQUATIONS

The equations that govern ray paths in a three dimensional anisotropic medium have been derived using the method of Hamilton by Haselgrove (1954). The equations were expressed in a form suitable for integration by standard numerical methods using a digital computer. The Jones program calculates the ray paths by integrating the following six differential equations which are a slight modification to those described by Haselgrove.

$$\frac{dr}{dt} = \left[v_r - \text{Real} \left(n \frac{\partial n}{\partial v_r} \right) \right] / \text{Real} (n n') \quad (2-1)$$

$$\frac{d\theta}{dt} = \left[v_\theta - \text{Real} \left(n \frac{\partial n}{\partial v_\theta} \right) \right] / r \text{Real} (n n') \quad (2-2)$$

$$\frac{d\phi}{dt} = v_\phi - \text{Real}(n \frac{\partial n}{\partial v_\phi}) / r \sin \theta \text{Real}(n n') \quad (2-3)$$

$$\frac{dv_r}{dt} = \frac{\text{Real}(n \frac{\partial n}{\partial r})}{\text{Real}(n n')} + v_\theta \frac{d\theta}{dt} + v_\phi \sin \theta \frac{d\phi}{dt} \quad (2-4)$$

$$\frac{dv_\theta}{dt} = \frac{1}{r} \left[\frac{\text{Real}(n \frac{\partial n}{\partial \theta})}{\text{Real}(n n')} - v_\theta \frac{dr}{dt} + r v_\phi \cos \theta \frac{d\phi}{dt} \right] \quad (2-5)$$

$$\frac{dv_\phi}{dt} = \frac{1}{r \sin \theta} \left[\frac{\text{Real}(n \frac{\partial n}{\partial \phi})}{\text{Real}(n n')} - v_\phi \sin \theta \frac{dr}{dt} - r v_\phi \cos \theta \frac{d\theta}{dt} \right] \quad (2-6)$$

The variables r , θ , and ϕ are the spherical polar coordinates of a point on the ray path; v_r , v_θ , and v_ϕ are the components of the wave normal in the r , θ , and ϕ directions, normalized so that

$$v_r^2 + v_\theta^2 + v_\phi^2 = \text{Real}(n^2) \quad (2-7)$$

where n and n' are the complex phase and group refractive indices which are based on Appleton-Hartree formula. The independent variable t is group path length in these equations whereas it is phase path length in Haselgrove equations. This change of independent variable has the advantage of speeding up the program by automatically decreasing the step length in real path near the reflection height. In addition to the six basic equations necessary to calculate the ray path, the program integrates the following to give the phase path, the absorption, and the Doppler shift, respectively.

$$\frac{dP}{dt} = \frac{\text{Real}(n^2)}{\text{Real}(n n')} \quad (2-8)$$

$$\frac{dA}{dt} = \frac{10}{\log_e 10} \frac{2\pi f}{c} \frac{|\text{Imag}(n^2)|}{\text{Real}(n n')} \quad (2-9)$$

$$\frac{d\Delta f}{dt} = - \frac{f}{c} \frac{\text{Real}(n \frac{\partial n}{\partial t})}{\text{Real}(n n')} \quad (2-10)$$

2.3 DESCRIPTION OF THE PROGRAM

The program traces the path of a radio wave through the ionosphere when given along with the ionospheric models, the transmitter coordinates, the operating frequency, the direction of transmission, the height of the receiver and the maximum number of hops desired. The general set up of the program can take both the electron collisions and the Earth's magnetic field into account and trace the two types of ray paths (ordinary and extraordinary). It can, at our option, drop either or both of the collisions and the magnetic field. The automatic homing feature, common to some ray tracing programs, is not built into this program and it had to be achieved by trial and error, knowing the starting point for the approximate direction of transmission to the receiver.

The distributions of electron density, collision frequency and Earth's magnetic field constitute the input models that describe the ionosphere. Routines for several ionospheric models have been made available with the program. Five analytic models and tabular or true-height analysis profiles constitute the supplied electron density routines. Two collision frequency routines exist; one for tabular profiles and the other for a constant collision frequency. There are two routines that model the Earth's magnetic field; one is for an Earth-centered dipole, and the other is based on constant dip and gyro-frequency. The model routines are arranged in the programs in such a fashion that they can be replaced with any desired models with utmost ease provided, of course, the new routines follow the format already set.

The numerical integration of the ray tracing equations can be carried out by using either one of the two routines available; one based on Runge-Kutta method, and the other on Adams-Moulton method.

The integration routine by Adams-Moulton method has a built-in mechanism for checking errors and adjusting the integration step size accordingly. The maximum allowable error in any single step for any of the equations integrated in the routine is specified in the form of an input parameter. The step size is decreased to gain required accuracy if the error is larger than the specified maximum and increased to reduce the computing time if the error is smaller. A value of 10^{-4} is commonly used for the maximum allowable error as a compromise between cost and accuracy.

The program uses two spherical polar coordinate systems; one is geographic, and the other computational. The input data such as the location of the transmitter and the geomagnetic north pole is given in geographic coordinates; the transformation to the computational system is carried out within the program. When the dipole model is used for the Earth's magnetic field, the computational system is a geomagnetic coordinate system and both electron density and collision frequency must be defined in geomagnetic coordinates.

The input data to the program is arranged in a one dimensional array (W array) and read in with one parameter on each card. This array provides all the information needed for the ray trace including the parameters associated with the analytic models for electron density, collision frequency and magnetic field. The output is available in various forms individually or in any combination. During the course of the ray trace the program will print information giving the position of the current ray path point, the wave normal direction and cumulative values of the quantities like group path, phase path, absorption, and Doppler shift. The main results of the program can be obtained, if desired, in the form of punched cards called ray-sets which can be used as input for other programs. The

ray paths can be plotted in two projection planes; a ground plane and any given vertical plane. It is possible to show the lateral deviations in a blown-up scale on the ground plane plot.

2.4 APPLICATION TO PLASMA CLOUDS

The ray tracing program has been used here to investigate the scattering behavior of an expanding Gaussian plasma cloud by synthesizing hf direct echo signatures both in Doppler shift and signal strength. The rays that have been traced are intended to simulate the signatures of test Mulberry (Pre-SECEDE) for which high quality Doppler data is available. The ultimate objective here is to compare the results with observation and thus test the validity of the Gaussian model for the ion cloud. The program has been used in the mode that takes the collisions and magnetic field into account as well as in the modes that neglect either one or both. The ray paths have been calculated for all the three types of rays, namely, ordinary, extraordinary and no-field.

The models adopted for the electron density of the cloud, the collision frequency and the magnetic field are all analytic throughout. The ion cloud model, discussed in detail in the next section, is represented by a Gaussian distribution cylindrically symmetric about the direction of Earth's magnetic field and governed by anisotropic diffusive expansion. The relevant Gaussian parameters that determine the electron density in time and space are based upon experimental measurements. The electron collisions are represented by a piece-wise exponential function with parameters that best fit the models published by Thrane and Piggot (1966). It turned out, however, that the collisional effects are negligible and never amount to more than a fraction of a dB in absorption. This is due to the fact that the ion cloud considered here was released in the F region where collisions are small and at twilight when the contribution from the

ambient ionosphere is still negligible. The dipole model is chosen for the Earth's magnetic field with the geomagnetic north pole located at 78.3°N and 291°E (geographic). The equatorial value of the gyrofrequency is taken to be 0.8 MHz and this together with the dipole model determines its value at any point in space.

The method of Adams-Moulton with relative error check was chosen out of the four options provided in the program for integrating the ray trace equations. The maximum allowable single step error was given a value in the range 10^{-4} to 10^{-6} depending on how stringent the ray tracing conditions are at a given time of the cloud's life. It was assigned a smaller value (5×10^{-6} or 10^{-6}), to keep uniform accuracy as judged from the first column of the printout (see Appendix A), during the late phase when the plasma frequency contour supporting the signal return is small in size and rapidly collapsing to the center. Whenever this parameter was altered, suitable changes have also been made in other related parameters like initial integration step size and its minimum limit.

The ray tracing results were printed out in all cases, but plots in the two possible planes, vertical and ground, have been made only for some selected cases of interest. A sample plot and a printout are presented in Appendix A. The supplementary information on polarization, phase path and group path, obtained along with the Doppler results, will not be discussed here as they fall beyond the scope of this report.

SECTION 3. PLASMA CLOUD MODEL

3.1 AMBIPOLEAR DIFFUSION MODEL

The ion clouds of interest here are generated in the F region by means of rocket releases of metallic Barium vapor. The cloud, on formation, is subject as a whole to electrodynamic drift due to the presence of external electric field while at the same time expanding in a manner determined by diffusion. The charge neutrality, that is $n_i = n_e$, is satisfied in the cloud since the Debye shielding length is much smaller than the typical cloud dimensions and the diffusion is of ambipolar nature. The problem of ambipolar diffusion of the cloud in the geomagnetic field, neglecting the external electric field, has been studied by Holway (1965). The diffusion equation has been solved in cylindrical coordinate system (r, ϕ, z) with z axis taken along the Earth's magnetic field. In this system, because of the cylindrical symmetry, the azimuthal component of the particle flux is non-divergent and it is, therefore, necessary to consider only the components in the z and r directions. Using the above criterian and a relation that the ion flux is the same as the electron flux in both the radial and longitudinal directions, Holway derives the equation for the ambipolar diffusion of the ionized cloud as:

$$\frac{\partial n}{\partial t} = \frac{D_{||}}{\Omega_{ie}} \cdot \frac{1}{r} \cdot \frac{\partial}{\partial r} \left(r \frac{\partial n}{\partial r} \right) + D_{||} \left(\frac{\partial^2 n}{\partial z^2} \right) \quad (3-1)$$

where n is the ion (electron) number density, $\Omega_{ie} = (1 + \omega_i \omega_e / v_i v_e)$, and $D_{||} = D_i D_e (T_i + T_e) / (D_i T_e + D_e T_i)$ is the ambipolar diffusion coefficient.

The solution to Equation 3-1 for an ionized release of N_i ions, which is initially spherical with a Gaussian distribution of initial effective radius h_o , is:

$$n(r, z, t) = \left[\frac{N_i}{\pi^{3/2} z_1 r_1^2} \right] \exp \left[- \left(\frac{z}{z_1} \right)^2 - \left(\frac{r}{r_1} \right)^2 \right] \quad (3-2)$$

where

$z_1 = (h_o^2 + 4D_{||} t)^{1/2}$ and $r_1 = (h_o^2 + 4D_{||} t/\Omega_{ie})^{1/2}$ are the longitudinal and transverse Gaussian radii.

An extension has been made recently to the above solution by Simon (1970) by taking the presence of an external electric field into consideration. The diffusion equation in this case has been formulated, after making considerable simplification by Simon as:

$$\frac{\partial N}{\partial t} = D_{\perp} \nabla_{\perp}^2 N + D_{||} \nabla_{||}^2 N + \alpha \vec{U}_o \cdot \vec{\nabla} N + \beta \vec{U}_o \times \vec{b} \cdot \vec{\nabla} N \quad (3-3)$$

The solution to Equation 3-3, assuming that the plasma is created at the origin at $t = 0$ and the total number of ions created at that time is S_o , is

$$N(\vec{x}, t) = \left[\frac{S_o}{4\pi D_{\perp} t (4\pi D_{||} t)^{1/2}} \right] \exp \left[- \frac{(r_1^2 + \alpha \vec{U}_o + \beta \vec{U}_o \times \vec{b} t)^2}{4 D_{\perp} t} - \frac{z^2}{4 D_{||} t} \right] \quad (3-4)$$

Note that Equations 3-3 and 3-4 retain Simon's notation. If the initial condition is changed from a δ function to that of a spherical Gaussian distribution with radius h_o , the Gaussian radii of Equation 3-4 would transform to the same form as of Equation 3-2 in the manner discussed by Holway (1965). The solution given in Equation 3-4 is a cylindrically symmetric Gaussian moving with velocity $(-\alpha \vec{U}_o - \beta \vec{U}_o \times \vec{b})$. Since the Doppler associated with uniform drift velocity can be taken into account explicitly outside the ray tracing program, Equation 3-2 has been adopted here for the electron density distribution. The origin about which the expansion takes place was allowed to shift, however, on the basis of the trajectory information obtained from the optical measurements.

3.2 MODEL TRANSFORMATION TO GEOMAGNETIC COORDINATE SYSTEM

The ray tracing program calls for electron densities and their gradients in terms of geomagnetic spherical dipole coordinates. This requires a correspondence between the cloud centered cylindrical coordinate system and the Earth-centered dipole coordinate system. The transformation can be made first by relating two Cartesian systems, one cloud centered (x, y, z) and the other Earth centered (x_m, y_m, z_m) , since they are directly related to respective polar systems. The system (x, y, z) is defined such that z is anti-parallel to the magnetic field direction and y is directed toward geomagnetic east in the northern hemisphere. In (x_m, y_m, z_m) , z_m is along the dipole axis and directed toward the north pole, (x_m, z_m) defines a reference (0°) geomagnetic meridian plane and y_m is toward geomagnetic east. In general, it involves one translation and two rotations to bring correspondence between the two systems, as shown in Figure 3-1. The translation is along the vector joining the two origins and the rotations are in two orthogonal, geomagnetic latitude and meridian, planes. Let the cloud center in geomagnetic coordinates be

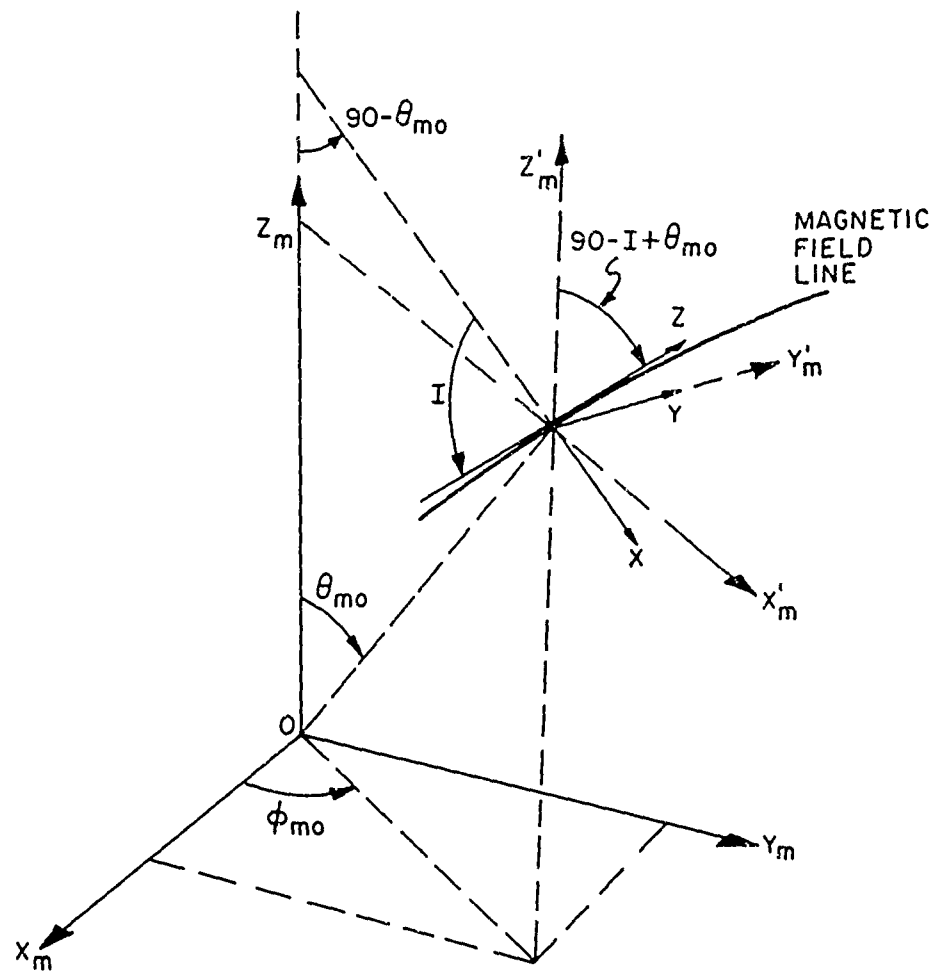


Figure 3-1 Illustration to Show the Coordinate Transformation from Earth Centered Geomagnetic Dipole System (x_m, y_m, z_m) to Cloud Centered System (x'_m, y'_m, z'_m). The Correspondence Between the Two Systems Requires One Translation and Two Rotations.

$(R_o, \theta_{mo}, \phi_{mo})$, θ_{mo} being geomagnetic co-latitude. When the system (x_m, y_m, z_m) is translated to the cloud center and rotated by ϕ_{mo} about the Z_m axis, an intermediate system (x'_m, y'_m, z'_m) with y'_m coinciding with y , would result as shown in Figure 3-1. (x'_m, y'_m, z'_m) is related to (x_m, y_m, z_m) as:

$$\begin{bmatrix} x'_m \\ y'_m \\ z'_m \end{bmatrix} = \begin{bmatrix} a' \\ b' \\ c' \end{bmatrix} + \begin{bmatrix} \cos \phi_{mo} & \sin \phi_{mo} & 0 \\ -\sin \phi_{mo} & \cos \phi_{mo} & 0 \\ 0 & 0 & 1 \end{bmatrix} \begin{bmatrix} x_m \\ y_m \\ z_m \end{bmatrix} \quad (3-5)$$

The matrix elements a' , b' , and c' are the result of the translation. Now a rotation by an angle χ_{mo} , which is equal to $(90 - I + \theta_{mo})$ as shown in Figure 3-1, in the plane (x'_m, z'_m) about the y'_m axis would bring the intermediate system to coincide with (x, y, z) . The relation between the two systems is given as:

$$\begin{bmatrix} x \\ y \\ z \end{bmatrix} = \begin{bmatrix} \cos \chi_{mo} & 0 & -\sin \chi_{mo} \\ 0 & 1 & 0 \\ \sin \chi_{mo} & 0 & \cos \chi_{mo} \end{bmatrix} \begin{bmatrix} x'_m \\ y'_m \\ z'_m \end{bmatrix} \quad (3-6)$$

combining Equations 3-5 and 3-6 we have

$$\begin{bmatrix} x \\ y \\ z \end{bmatrix} = \begin{bmatrix} a \\ b \\ c \end{bmatrix} + \begin{bmatrix} \cos \phi_{mo} \cos \chi_{mo} & \sin \phi_{mo} \cos \chi_{mo} & -\sin \chi_{mo} \\ -\sin \phi_{mo} & \cos \phi_{mo} & 0 \\ \cos \phi_{mo} \sin \chi_{mo} & \sin \phi_{mo} \sin \chi_{mo} & \cos \chi_{mo} \end{bmatrix} \begin{bmatrix} x_m \\ y_m \\ z_m \end{bmatrix} \quad (3-7)$$

The elements a, b and c denote the translation with respect to x, y, and z and can be evaluated by considering the origin of the cloud where:

$$\begin{bmatrix} x \\ y \\ z \end{bmatrix} = \begin{array}{l} x_m = x_{mo} = (R_\oplus + h) \sin \theta_{mo} \cos \phi_{mo} \\ y_m = y_{mo} = (R_\oplus + h) \sin \theta_{mo} \sin \phi_{mo} \\ z_m = z_{mo} = (R_\oplus + h) \cos \theta_{mo} \end{array} \quad (3-8)$$

R_\oplus is the radius of the Earth, h is the height and θ_{mo} , ϕ_{mo} are the geomagnetic colatitude and longitude of the cloud center. Substituting Equation 3-8 into Equation 3-7 gives

$$a = -x_{mo} \cos \phi_{mo} \cos \chi_{mo} - y_{mo} \sin \phi_{mo} \cos \chi_{mo} + z_{mo} \sin \chi_{mo} \quad (3-9a)$$

$$b = x_{mo} \sin \phi_{mo} - y_{mo} \cos \phi_{mo} \quad (3-9b)$$

$$c = x_{mo} \cos \phi_{mo} \sin \chi_{mo} - y_{mo} \sin \phi_{mo} \sin \chi_{mo} - z_{mo} \cos \chi_{mo} \quad (3-9c)$$

The position of the cloud center is made available usually in geographic coordinates and they are converted to geomagnetic coordinates using the following expressions:

$$\cos \theta_{mo} = \sin \theta_o \sin \theta_n + \cos \theta_o \cos \theta_n \cos (\phi_o - \phi_n) \quad (3-10a)$$

$$\sin \phi_{mo} = \frac{\cos \theta_o \sin (\phi_o - \phi_n)}{\sin \theta_{mo}} \quad (3-10b)$$

Where (θ_o, ϕ_o) are the geographic latitude and longitude of the cloud center and (θ_n, ϕ_n) are the geographic latitude and longitude of the geomagnetic north pole (note that θ_{mo} is the geomagnetic colatitude).

When the ray tracing program refers to the electron density subroutine with geomagnetic coordinates (R, θ_m, ϕ_m) , they are transformed to corresponding (x, y, z) through (x_m, y_m, z_m) . Further, by converting the cylindrical coordinates of Equation 3-2 to corresponding (x, y, z) we have:

$$n(R, \theta_m, \phi_m) = n(x, y, z) = \left[\left(\frac{N_i}{\pi^{3/2} z_1 r_1^2} \right) \right] \exp. \left[-\frac{(x^2 + y^2)}{r_1^2} - \frac{z^2}{z_1^2} \right] \quad (3-11)$$

3.2.1 DENSITY GRADIENT FIELD

The electron density partial derivatives are evaluated by using the following matrix relations.

$$\begin{bmatrix} \frac{\partial n}{\partial R} \\ \frac{\partial n}{\partial \theta_m} \\ \frac{\partial n}{\partial \phi_m} \end{bmatrix} = \begin{bmatrix} \frac{\partial x_m}{\partial R} & \frac{\partial y_m}{\partial R} & \frac{\partial z_m}{\partial R} \\ \frac{\partial x_m}{\partial \theta_m} & \frac{\partial y_m}{\partial \theta_m} & \frac{\partial z_m}{\partial \theta_m} \\ \frac{\partial x_m}{\partial \phi_m} & \frac{\partial y_m}{\partial \phi_m} & \frac{\partial z_m}{\partial \phi_m} \end{bmatrix} \begin{bmatrix} \frac{\partial n}{\partial x_m} \\ \frac{\partial n}{\partial y_m} \\ \frac{\partial n}{\partial z_m} \end{bmatrix} \quad (3-12)$$

$$\begin{bmatrix} \frac{\partial x_m}{\partial R} & \frac{\partial y_m}{\partial R} & \frac{\partial z_m}{\partial R} \\ \frac{\partial x_m}{\partial \theta_m} & \frac{\partial y_m}{\partial \theta_m} & \frac{\partial z_m}{\partial \theta_m} \\ \frac{\partial x_m}{\partial \phi_m} & \frac{\partial y_m}{\partial \phi_m} & \frac{\partial z_m}{\partial \phi_m} \end{bmatrix} = \begin{bmatrix} \sin \theta \cos \phi_m & \sin \theta_m \sin \phi_m & \cos \theta_m \\ R \cos \theta_m \cos \phi_m & R \cos \theta_m \sin \phi_m & -R \sin \theta_m \\ -R \sin \theta_m \sin \phi_m & R \sin \theta_m \cos \phi_m & 0 \end{bmatrix}$$

(3-13)

$$\begin{bmatrix} \frac{\partial n}{\partial x_m} \\ \frac{\partial n}{\partial y_m} \\ \frac{\partial n}{\partial z_m} \end{bmatrix} = \begin{bmatrix} \frac{\partial x}{\partial x_m} & \frac{\partial y}{\partial x_m} & \frac{\partial z}{\partial x_m} \\ \frac{\partial x}{\partial y_m} & \frac{\partial y}{\partial y_m} & \frac{\partial z}{\partial y_m} \\ \frac{\partial x}{\partial z_m} & \frac{\partial y}{\partial z_m} & \frac{\partial z}{\partial z_m} \end{bmatrix} \begin{bmatrix} \frac{\partial n}{\partial x} \\ \frac{\partial n}{\partial y} \\ \frac{\partial n}{\partial z} \end{bmatrix}$$

(3-14)

$$\begin{bmatrix} \frac{\partial x}{\partial x_m} & \frac{\partial y}{\partial x_m} & \frac{\partial z}{\partial x_m} \\ \frac{\partial x}{\partial y_m} & \frac{\partial y}{\partial y_m} & \frac{\partial z}{\partial y_m} \\ \frac{\partial x}{\partial z_m} & \frac{\partial y}{\partial z_m} & \frac{\partial z}{\partial z_m} \end{bmatrix} = \begin{bmatrix} \cos \phi_{mo} & \cos \chi_{mo} & -\sin \phi_{mo} & \cos \phi_{mo} & \sin \chi_{mo} \\ \sin \phi_{mo} & \cos \chi_{mo} & \cos \phi_{mo} & \sin \phi_{mo} & \sin \chi_{mo} \\ -\sin \chi_{mo} & 0 & \cos \chi_{mo} & & \end{bmatrix}$$

(3-15)

$$\begin{bmatrix} \frac{\partial n}{\partial x} \\ \frac{\partial n}{\partial y} \\ \frac{\partial n}{\partial z} \end{bmatrix} = \begin{bmatrix} n(R, \theta_m, \phi_m) \left[-\frac{2x}{r_1^2} \right] \\ n(R, \theta_m, \phi_m) \left[-\frac{2y}{r_1^2} \right] \\ n(R, \theta_m, \phi_m) \left[-\frac{2z}{z_1^2} \right] \end{bmatrix} \quad (3-16)$$

The time derivative $\partial n / \partial t$ is evaluated by writing n as

$$n(x, y, z, t) = \underbrace{\frac{N_i}{\pi^{3/2}}}_{f(t)} \underbrace{\frac{(1-e^{-t/\tau})}{z_1^2 r_1^2}}_{g(t)} e^{-\left(\frac{x^2 + y^2}{r_1^2}\right)} e^{-\left(\frac{z^2}{z_1^2}\right)} \quad (3-17)$$

$$\frac{\partial n}{\partial t} = \frac{N_i}{\pi^{3/2}} \left[\frac{\partial n}{\partial f} \frac{\partial f}{\partial t} + \frac{\partial n}{\partial g} \frac{\partial g}{\partial t} + \frac{\partial n}{\partial H} \frac{\partial H}{\partial t} \right] \quad (3-18)$$

$$= \frac{N_i}{\pi^{3/2}} \left[gH \frac{\partial f}{\partial t} + fH \frac{\partial g}{\partial t} + fg \frac{\partial H}{\partial t} \right]$$

$$\frac{\partial f}{\partial t} = \frac{e^{-t/\tau}}{\tau z_1^2 r_1^2} - \frac{f}{z_1^2 r_1^2} (4 z_1^2 D_{\perp} + 2D_{||} r_1^2) \quad (3-19a)$$

$$\frac{\partial g}{\partial t} = 4 D_{\perp} g \left[(x^2 + y^2) / r_1^4 \right] \quad (3-19b)$$

$$\frac{\partial H}{\partial t} = 4 D_{||} H (z^2 / z_1^4) \quad (3-19c)$$

3.3 ION CLOUD INPUT PARAMETERS

The coordinates of the center of the ion cloud and the parameters, total ion content N_i , ionization time constant τ , initial Gaussian radius h_o , and longitudinal and transverse diffusion coefficients $D_{||}$ and D_{\perp} form the input to set up the electron density distribution for the ray tracing. The numerical values of the parameters are appropriate to test Mulberry of Pre-SECEDE and are taken from Minkoff (1970). The positional data obtained by photographic means was available in the form of look angles (azimuth and elevation) from different observation sites. These observations taken from pairs of stations have been used to determine the coordinates of the cloud following a vector method described in Appendix B. The trajectory information is shown in Figure 3-2 for the period of interest of ray tracing.

The total ion content N_i is obtained by integrating Equation 3-2 over all space, from which:

$$N_i = n_p (t) \pi^{3/2} (h_o^2 + 4D_{||} t)^{1/2} (h_o^2 + 4D_{\perp} t)^{1/2} \quad (3-20)$$

The peak electron (ion) density $n_p (t)$ is taken from hf radar measurements. The Gaussian radii $(h_o^2 + 4D_{||} t)^{1/2}$ and $(h_o^2 + 4D_{\perp} t)^{1/2}$ are determined by means of microdensitometer scans of the filter photographs of the cloud. Figure 3-2 also presents the peak electron density variation with time and the results from the densitometer scans. The numerical values obtained for the parameters are given in Table 3-1.

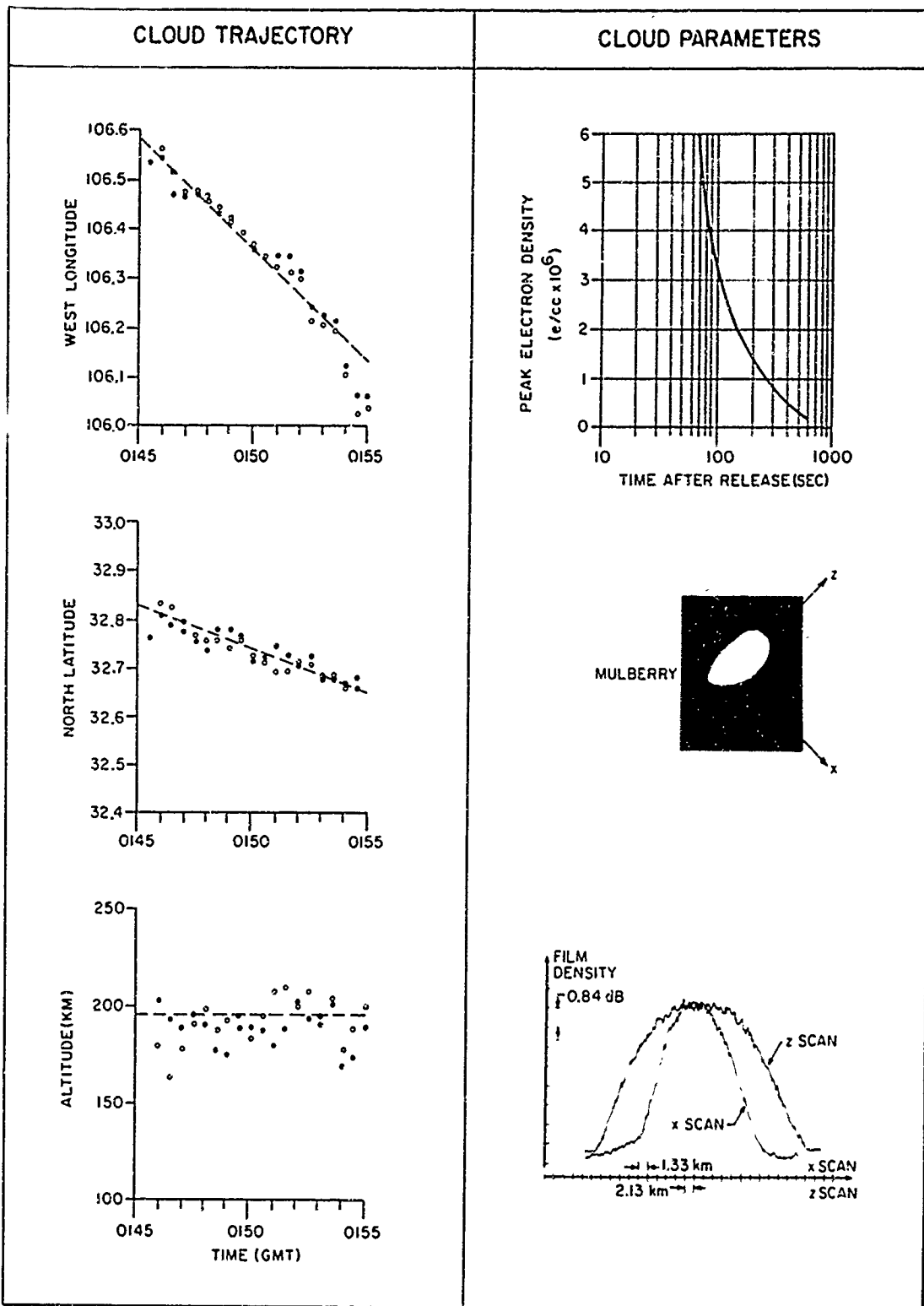


Figure 3-2 The Trajectory, the Peak Electron Density and the Results From Microdensitometer Scans of the Filter Photographs of the Cloud. (Filled and Open Circles in the Trajectory Data Represent Determinations from Two Pairs of Optical Stations).

TABLE 3-1
NUMERICAL VALUES FOR ION CLOUD PARAMETERS

Test	h_o (KM)	$D_{ }$ (KM ² /SEC)	D_{\perp} (KM ² /SEC)	N_i
Mulberry	3.0	0.13	0.045	3.0×10^{24}

The reader is referred to Minkoff (1970) for details on how these parameters are deduced.

SECTION 4. SYNTHESIS OF RADAR SIGNATURES

Two methods have been used for synthesizing radar signatures for the test Mulberry; one involves the rigorous ray tracing technique, and the other, an approximate technique meant primarily for the purpose of comparison, is based on an expanding hard ellipsoid model. This section is devoted to a description of the two methods and to a discussion of the results obtained.

4.1 RAY TRACING METHOD

There are two steps involved in synthesizing a radar signature. The first step is to determine the ray that homes in on the receiver when the transmitter-cloud-receiver configuration is given. The Doppler shift of interest is the one associated with this ray and it is listed in the output of the ray tracing program as a cumulative sum along the ray path. The next step is to determine the signal strength associated with this ray. It is evaluated in terms of radar scattering cross section of the cloud since it is a convenient parameter to compare different models and to gain some insight into the scattering behavior of the ion clouds. The process of homing-in on the receiver proceeds in steps and is as follows: First, the elevation and azimuth of the cloud center is calculated with respect to the transmitter location. This provides the initial guess for the direction of transmission at the starting time. Using this as reference direction, a matrix of nine rays (3×3 in elevation and azimuth) defining a rectangular solid angle are shot normally as a first trial. The angular increments in elevation and azimuth are selected such that the impact points form a contour that encloses the receiver location. The points, in general, describe a skewed quadrilateral because of the nonlinear nature of the cloud defocussing.

The next trial uses, in general, four rays for which the elevation and azimuth angles are arrived at by interpolating between the constant elevation and constant azimuth lines associated with the impact points. The rays, in this trial, converge toward the receiver to come usually within 25 km. Proceeding along the same lines, the next set of four trial rays shrink the impact area to typically a 5 km square. The 'homing in' ray is determined, finally, on the basis of the last set of four impact points. The ray is considered to have successfully 'homed in' if it returns to within 1 km of the receiver location. The 'homing in' ray for an initial time serves as a guide to arrive at the first guess trial rays for a subsequent time. Figure 4-1 illustrates the sequence of trials used to accomplish the homing of an extraordinary ray of 16.078 MHz transmitted at 70 seconds after the release of the cloud. It was found that, in practice, it is often easier to guess the bound rays in elevation than in azimuth and consequently instead of (3×3) , a (2×3) initial matrix of rays as shown in the figure was found sufficient to enclose the receiver. In selecting the next set of four rays, some account is made for the skewness of the elevation and azimuth lines instead of choosing the angles associated with four evenly spaced points around the receiver. The final set of four trial rays, however, are selected evenly to center the receiver. The sequence shown in the figure represent a shrink in the elevation angle increment from 0.08 to 0.0008° and azimuthal increment from 0.3 to 0.0052 . On obtaining the homing ray, the scattering cross section presented by the cloud to this ray is determined as described below.

4.1.1 RADAR CROSS SECTION OF THE CLOUD

The scattering cross section of the cloud σ , defined in terms of an equivalent isotropic scatter, is given by the bistatic radar equation as:

MULBERRY F=16.078 MHz X'RAORDINARY RAY

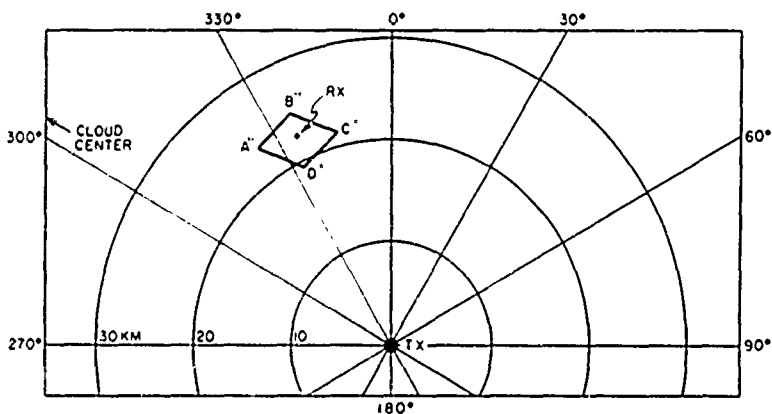
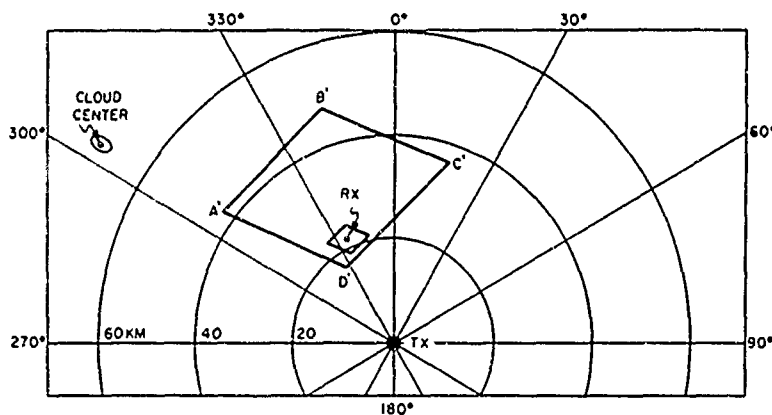
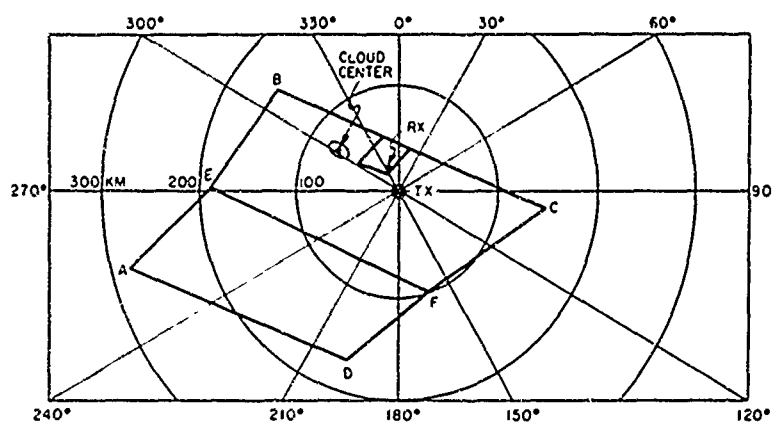


Figure 4-1 Illustrates the Method for Determination of the 'Homing' Ray. A, B, C, D, etc. are the Ground Impact Points When a Bundle of Rays Incremented in Azimuth and Elevation are Transmitted

$$\sigma = \frac{16\pi^2 R_1^2 R_2^2}{P_t G_t A_r} \cdot P_r \quad (4-1)$$

where

P_t = Transmitted power

G_t = Effective gain of the transmitting antenna

R_1 = Range to the scattering volume from the transmitter

R_2 = Range to the scattering volume from the receiver

P_r = Received power

A_r = Effective collecting area of the receiving antenna

A_r can be expressed as $G_R \lambda^2 / 4\pi$, where G_R is the effective gain of the receiving antenna and λ is the wavelength of the received signal. The scattering cross section of the cloud can be calculated from Equation 4-1 following the technique developed by Croft (1967) and generalized recently by Georges and Stephenson (1969) for 3D ray tracing simulation of hf ground backscatter signatures. The method derives an expression for the received power P_r which results in an expression for σ free of system parameters. This makes it possible to calculate σ solely on the basis of the ray tracing results. The method in brief is as follows:

A bundle of rays are transmitted about the direction of the homing ray in a small solid angle defined by an elevation angle increment of $\Delta\beta$ and azimuth angle increment of $\Delta\phi$. The flux of energy leaving in this solid angle will refract through the cloud and strike the ground on return over an area denoted as A . The amount of power reaching the impact area is a fraction K times the power fed into the flux tube of transmission where the fraction is determined by the

dissipation losses in the medium. When the transmission is centered at an elevation angle of β , then the solid angle into which the energy is injected becomes $\Delta\beta \Delta\phi \cos \beta$. The power leaving this solid angle is given as:

$$\Delta P_t = \frac{P_t G_t \Delta\beta \Delta\phi \cos \beta}{4\pi} \quad (4-2)$$

when this power approaches the impact area A at the elevation angle Ψ , then the received power P_r is given as:

$$P_r = \frac{P_t G_t \Delta\beta \Delta\phi \cos \beta A_r K}{4\pi A \sin \Psi} \quad (4-3)$$

The fraction K is given as $\exp(-X/4.343)$ where X is the total absorption in dB suffered by the homing ray. The Equation 4-3 for P_r applies strictly to a cw radar and in the case of a pulse radar it should be multiplied by a correction factor to take account of the pulse spreading in time. If τ and $\tau + \Delta\tau$ are the pulse lengths of the transmitted and received signals the correction factor is given approximately as $(\tau/\tau+\Delta\tau)$. This correction is considered small and neglected.

Substituting for P_r in Equation 4-1 leads to

$$\sigma = \frac{4\pi R_1^2 R_2^2 \Delta\beta \Delta\phi \cos \beta K}{A \sin \Psi} \quad (4-4)$$

In the Equation 4-4 for σ , the parameters β , $\Delta\beta$ and $\Delta\phi$ are the specified input to the ray tracing program. The output provides Ψ , K and all the information necessary to compute R_1 , R_2 and A . The geometry involved

to calculate A is the same as described by Goerges and Stephenson (1969) and is as shown in Figure 4-2. Consider a set of four rays that constitute a rectangular flux tube. The rays while passing through the cloud undergo lateral deviations and on hitting the ground form a spherical quadrilateral. The area of the quadrilateral can be calculated from the coordinates of the four corners supplied by the ray tracing program. In practice, the four rays of the flux tube

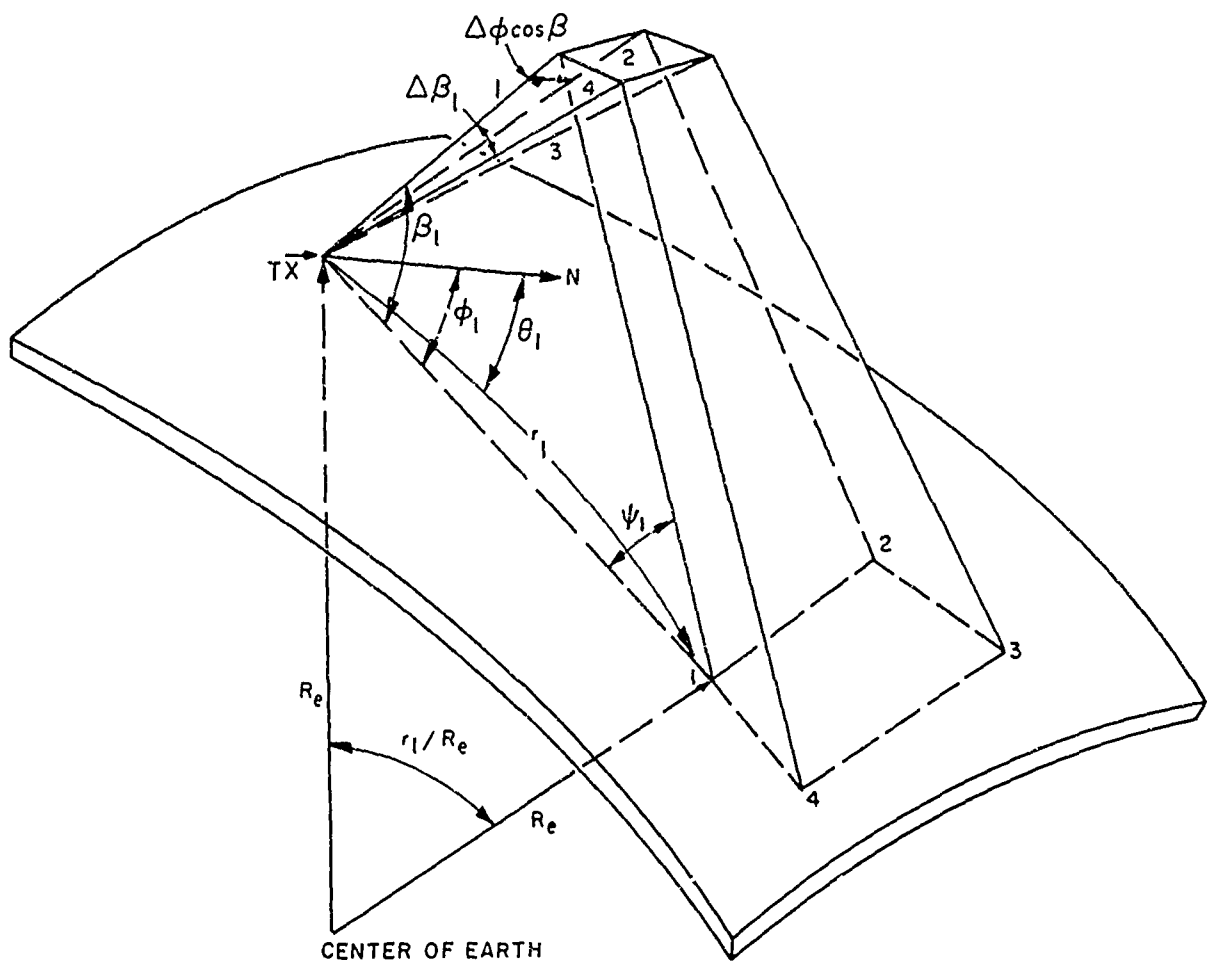


Figure 4-2 Geometry of an Electromagnetic Flux Tube Illuminating a Patch of Ground on Reflection from the Plasma Cloud

are so closely packed that the quadrilateral can be considered plane and a simple formula for the area can be applied. If r_1 , r_2 , r_3 and r_4 are the ground ranges to the four landing points and θ_1 , θ_2 , θ_3 and θ_4 are their azimuths then,

$$A \approx \frac{1}{2} \left| \frac{r_3 - r_1}{\sin \alpha} \right| \left| \frac{r_4 - r_2}{\sin \gamma} \right| \sin (\alpha + \gamma) \quad (4-5a)$$

where

$$\tan \alpha = \left| \frac{r_3 - r_1}{\theta_3 - \theta_1} \right| \left[R_E \sin \frac{r_3 + r_1}{2R_E} \right]^{-1} \quad (4-5b)$$

$$\tan \gamma = \left| \frac{r_4 - r_2}{\theta_4 - \theta_2} \right| \left[R_E \sin \frac{r_4 + r_2}{2R_E} \right]^{-1} \quad (4-5c)$$

and R_E is the radius of the Earth. This amounts to calculating the area of a quadrilateral by one-half the product of its diagonals times the sine of the angle between them. The area is calculated using the final set of trial rays such as shown in Figure 4-1 provided it is less than about 5 km square and the receiver is reasonably well centered. Otherwise, a new set of four rays closely spaced about the homing ray are used to meet the requirement.

The ranges R_1 and R_2 to the reflection point from the transmitter and the receiver are calculated by forming two triangles as shown in Figure 4-3. Considering the triangle TSO, the range R_1 is obtained as:

$$R_1 = \left[R_E \sin \xi_1 / \cos(\xi_1 + \beta) \right] \quad (4-6)$$

The ground range to the subreflection point TS' taken from the ray tracing output provides the central Earth angle ξ_1 .

The range R_2 is obtained, considering the Triangle RSO, as:

$$R_2 = \left[(R_E \sin \xi_2)^2 + (R_E - R_E \sin \xi_2 + h)^2 \right]^{1/2} \quad (4-7)$$

The ground range RS_1 which provides ξ_2 is calculated from the spherical triangle TRS_1 knowing the ranges TR and TS_1 and the azimuth of the subreflection point with respect to TR.

The scattering cross section σ is calculated by substituting the Equations 4-5, 4-6 and 4-7 in 4-4.

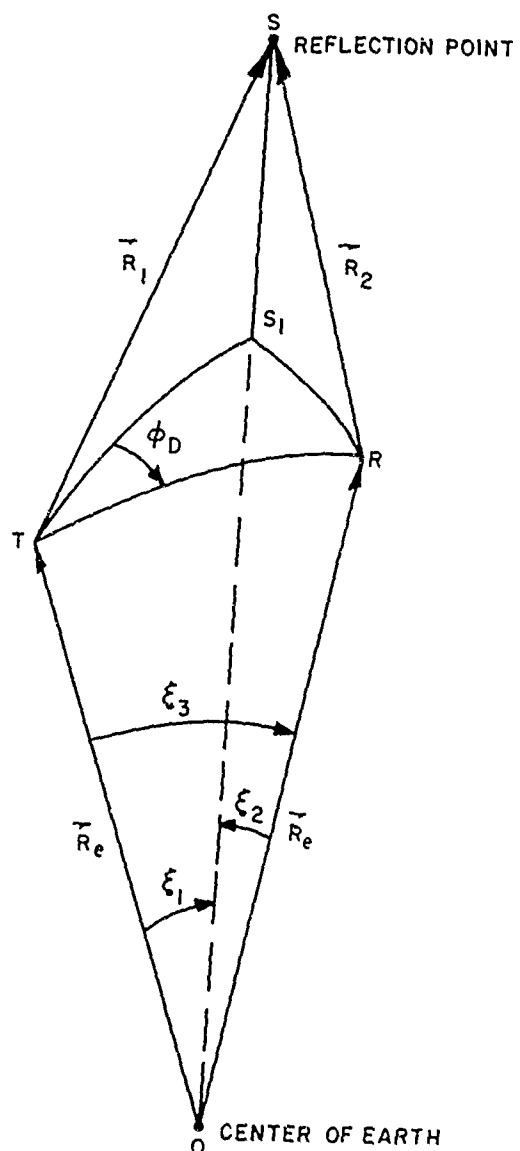


Figure 4-3 Illustration to Evaluate the Ranges R_1 and R_2 to the Reflection Point from the Transmitter and the Receiver

4.2 HARD EXPANDING ELLIPSOID METHOD

4.2.1 RADAR CROSS SECTION (RCS)

The radar cross section of a smooth body is given from considerations of geometric optics as (Crispin and Maffett, 1968):

$$\sigma \approx \pi R_1 R_2 \quad (4-8)$$

Where R_1 and R_2 are the principal radii of curvature at the specular reflection point and are both assumed to be large in comparison with the operating wavelength. If the equation of the target surface is expressed in the form $z = f(x, y)$, then

$$R_1 R_2 = \frac{(1 + f_x^2 + f_y^2)^2}{|f_{xx} f_{xy} - f_{xy}^2|} \quad (4-9)$$

where $f_x = \frac{\partial z}{\partial x}$, $f_y = \frac{\partial z}{\partial y}$, $f_{xx} = \frac{\partial^2 z}{\partial x^2}$, $f_{yy} = \frac{\partial^2 z}{\partial y^2}$ and $f_{xy} = \frac{\partial^2 z}{\partial x \partial y}$

The surface of interest here is that of an ellipsoid for which the equation can be written as:

$$\left(\frac{x}{a}\right)^2 + \left(\frac{y}{b}\right)^2 + \left(\frac{z}{c}\right)^2 = 1 \quad (4-10)$$

Using the coordinate system shown in Figure 4-4, the following expression can be derived for monostatic radar cross section of the general ellipsoid.

$$\sigma = \frac{\pi a^2 b^2 c^2}{[a^2 \sin^2 \theta \cos^2 \phi + b^2 \sin^2 \theta \sin^2 \phi + c^2 \cos^2 \theta]^2} \quad (4-11)$$

The Equation 4-11 for the case of Barium ion clouds, which can be approximated to a prolate spheroid ($a = b$), can be reduced to

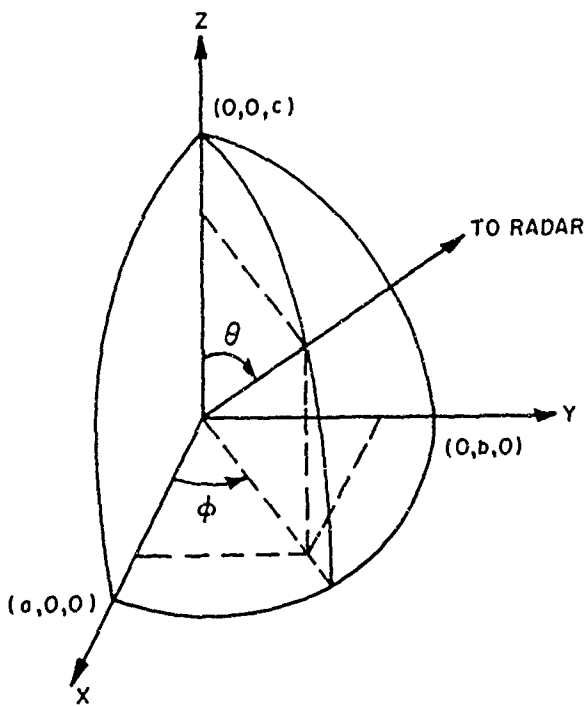


Figure 4-4 Coordinate System Adopted to Obtain An Expression for the Radar Cross Section of the Ellipsoid

$$\sigma = \frac{\pi b^4 c^2}{[b^2 \sin^2 \theta + c^2 \cos^2 \theta]^2} \quad (4-12)$$

The radar configuration in the experiment of interest here (test Mulberry) is approximately monostatic and, therefore, the Equation 4-12 can be used to calculate the cross section. The parameters c and b , the major and minor axes of the cloud, and the aspect angle θ to the specular point from the radar are evaluated at any given time as described in the following paragraphs.

4.2.1.1 Determination of c and b

The electron density in the cloud is given according to the Equation 3-2. The parameters c and b are the major and minor axes of the ellipsoidal contour with the electron density critical to the

operating frequency of the radar. If n_p denotes the critical density, it is given by considering the variation along the axis ($r = 0$) as:

$$n_p = \frac{N_i (1 - e^{-t/\tau}) \exp. \left[-c^2/(h_o^2 + 4D_{||}t) \right]}{\pi^{3/2} (h_o^2 + 4D_{||}t)^{1/2} (h_o^2 + 4D_{\perp}t)} \quad (4-13)$$

From Equation 4-13 one obtains

$$c = (h_o^2 + 4D_{||}t)^{1/2} \left[\ln \frac{N_i (1 - e^{-t/\tau})}{n_p \pi^{3/2} (h_o^2 + 4D_{||}t)^{1/2} (h_o^2 + 4D_{\perp}t)} \right]^{1/2} \quad (4-14)$$

similarly considering the variation along a radius vector at $z = 0$, one gets

$$b = (h^2 + 4D_{\perp}t)^{1/2} \left[\ln \frac{N_i (1 - e^{-t/\tau})}{n_p \pi^{3/2} (h^2 + 4D_{||}t)^{1/2} (h^2 + 4D_{\perp}t)} \right]^{1/2} \quad (4-15)$$

4.2.1.2 Determination of the Aspect Angle θ

Consider a cloud centered Cartesian system (x , y , z) as defined in Section 3 with z axis anti-parallel to the direction of the Earth's magnetic field. Let the coordinates of the radar in this system be (x_1, y_1, z_1) and those of the specular point be denoted as (x_o, y_o, z_o) . The coordinates of the specular point are evaluated by considering a unit vector normal to the surface at that point. The equations for the ellipsoid and the unit normal vector are:

$$z = \left[c^2 - c^2 \left(\frac{x^2 + y^2}{b^2} \right) \right]^{1/2} \quad (4-16)$$

$$\vec{N} = \frac{\vec{i} f_{x_0} + \vec{j} f_{y_0} - \vec{k}}{(f_{x_0}^2 + f_{y_0}^2 + 1)^{1/2}} \quad (4-17)$$

Where i , j , k are the unit vectors along x , y , z and f_{x_0} , f_{y_0} , are the partial derivatives $\frac{\partial z}{\partial x}$ and $\frac{\partial z}{\partial y}$ at the point (x_0, y_0, z_0) . Since the normal vector is along the line joining the specular point to the radar, the unit vector \vec{N} can also be expressed, using the geometry shown in Figure 4-5, as:

$$\vec{N} = \frac{\vec{PR}}{|PR|} = \frac{\vec{i}(x_1 - x_0) + \vec{j}(y_1 - y_0) + \vec{k}(z_1 - z_0)}{\left[(x_1 - x_0)^2 + (y_1 - y_0)^2 + (z_1 - z_0)^2 \right]^{1/2}} \quad (4-18)$$

Equating 4-17 and 4-18 and substituting $(-\frac{c^2}{b^2}, \frac{x_0}{z_0})$ for f_{x_0} and $(-\frac{c^2}{b^2}, \frac{y_0}{z_0})$ for f_{y_0} leads to

$$x_1 = x_0 \left[1 - \frac{c^2}{b^2} + \frac{c^2}{b^2} \frac{z_1}{z_0} \right] \quad (4-19)$$

$$y_1 = y_0 \left[1 - \frac{c^2}{b^2} + \frac{c^2}{b^2} \frac{z_1}{z_0} \right] \quad (4-20)$$

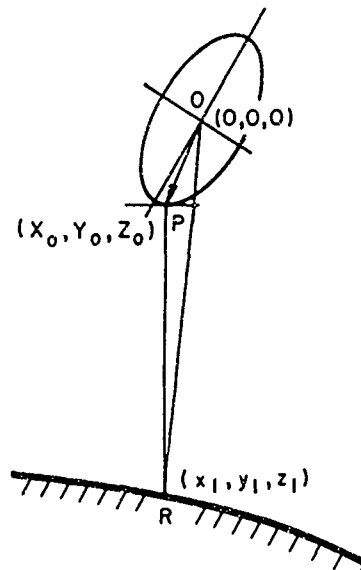


Figure 4-5 The Geometry to Express Unit Vector Normal to the Cloud Surface at the Specular Point from the Radar

Equations 4-19 and 4-20 are squared and then added to yield, on substitution of $[b^2 - (b^2/c^2)z_o^2]$ for $x_o^2 + y_o^2$, a quartic in z_o of the form

$$Az_o^4 + Bz_o^3 + Cz_o^2 + Dz_o + E = 0 \quad (4-21)$$

where

$$A = \left[\frac{b^2}{c^2} + \frac{c^2}{b^2} - 2 \right]$$

$$B = \left[2z_1 - 2 \frac{c^2}{b^2} z_1 \right]$$

$$C = \left[x_1^2 + y_1^2 + \frac{c^2}{b^2} z_1^2 - b^2 - \frac{c^4}{b^2} + 2c^2 \right]$$

$$D = \left[2 \frac{c^4}{b^2} z_1 - 2c^2 z_1 \right]$$

$$E = \left[- \frac{c^4}{b^2} z_1^2 \right]$$

Since the dimensions of the cloud are very small compared to the distance between the radar and the cloud, a good approximation to the solution of the Equation 4-21 can be obtained by dropping the higher order terms with coefficients A and B. The resulting equation is solved for z_o and of the two possible values, the one with favorable geometry for specular reflection is taken and substituted, in turn, in Equations 4-19 and 4-20 to get x_o and y_o . The coordinates of the radar that are used to calculate the specular point are given by:

$$\begin{bmatrix} x_1 \\ y_1 \\ z_1 \end{bmatrix} = \begin{bmatrix} a \\ b \\ c \end{bmatrix} + \begin{bmatrix} \cos \phi_{mo} & \cos \chi_{mo} & \sin \phi_{mo} & \cos \chi_{mo} & -\sin \chi_o \\ -\sin \phi_{mo} & & \cos \phi_{mo} & & 0 \\ \cos \phi_{mo} & \sin \chi_{mo} & \sin \phi_{mo} & \sin \chi_{mo} & \cos \chi_{mo} \end{bmatrix} \begin{bmatrix} x_{ml} \\ y_{ml} \\ z_{ml} \end{bmatrix}$$

(4-22)

The elements a , b^* and c^* and the transformation matrix are the same as in Equation 3-7. (x_{ml}, y_{ml}, z_{ml}) are the coordinates of the radar in the geomagnetic dipole coordinate system defined in paragraph 3.2. Knowing the coordinates of the specular point, the aspect angle θ can be calculated by taking the scalar product of the unit vector \vec{N} and a unit vector along the magnetic field \vec{B} .

Let

$$\vec{N} = \ell_1 \hat{i} + \ell_2 \hat{j} + \ell_3 \hat{k}$$

$$\vec{B} = m_1 \hat{i} + m_2 \hat{j} + m_3 \hat{k}$$

then

$$\cos \theta = \ell_1 m_1 + \ell_2 m_2 + \ell_3 m_3$$

The direction cosines are given as: $m_1 = m_2 = 0, m_3 = -1$
and $\ell_3 = -[f_{xo}^2 + f_{yo}^2 + 1]^{-1/2}$

* Not to be confused with major and minors axes of the ellipsoid.

substituting for f_{x_0} and f_{y_0} one obtains:

$$\cos \theta = \left[\frac{\frac{c^4}{b^4}}{\frac{(x_0^2 + y_0^2)}{z_0^2} + 1} \right]^{-1/2} \quad (4-23)$$

4.2.2 DETERMINATION OF DOPPLER SHIFT

Let (x_{01}, y_{01}, z_{01}) and (x_{02}, y_{02}, z_{02}) be the coordinates of the specular reflection points on the cloud at times t and $t + \Delta t$ as shown in Figure 4-6. The corresponding ranges to these reflection points from the radar are given as:

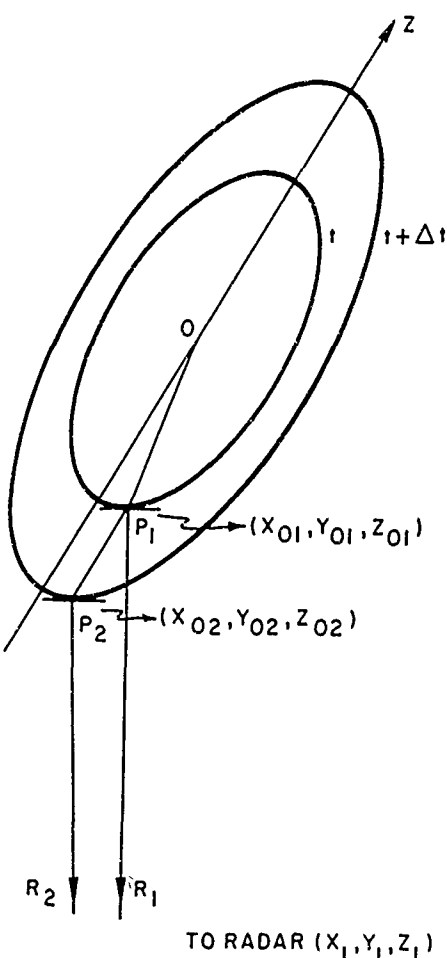


Figure 4-6 Illustrate the Position of the Specular Point at Two Instants of Time to Calculate the Path Difference to it from the Radar

$$R_1 = \left[(x_1 - x_{01})^2 + (y_1 - y_{01})^2 + (z_1 - z_{01})^2 \right]^{\frac{1}{2}} \quad (4-24)$$

$$R_2 = \left[(x_1 - x_{02})^2 + (y_1 - y_{02})^2 + (z_1 - z_{02})^2 \right]^{\frac{1}{2}} \quad (4-25)$$

Since the signal traverses in free space the difference between the two ranges $\Delta R (=R_2 - R_1)$ represents the difference in the phase path length to the reflection point. Hence the Doppler shift of the reflected signal at the radar is obtained by

$$\Delta f = \frac{-2\Delta R}{\lambda \Delta t} \quad (4-26)$$

The Doppler shift given in the Equation 4-26 is smeared over the time interval Δt . The time increment should, therefore, be made as small as possible without running into computer round off errors in calculating ΔR . Figure 4-7 shows a typical case to illustrate how the Doppler shift approaches its true value in an asymptotic manner as Δt is decreased from 0.5 to 0.01 seconds. If Δt is allowed to take lower values, it would result in a fluctuation in Δf . Since the lower limit of Δt is time dependent, it is allowed to vary over an interval at each time and the asymptotic value such as shown in the Figure 4-7 is picked for the Doppler shift.

4.3 RESULTS AND DISCUSSION

4.3.1 RAY TRACING RESULTS

Figure 4-8 shows ray path projection plots in both vertical and ground planes at 100 seconds after release for all the three modes namely, the no-field the ordinary and the extraordinary. The ray path segments close to the reflection level where there is an appreciable bending are plotted on an enlarged scale for the vertical plane in Figure 4-9 to show how the three modes refract in the denser regions of the cloud.

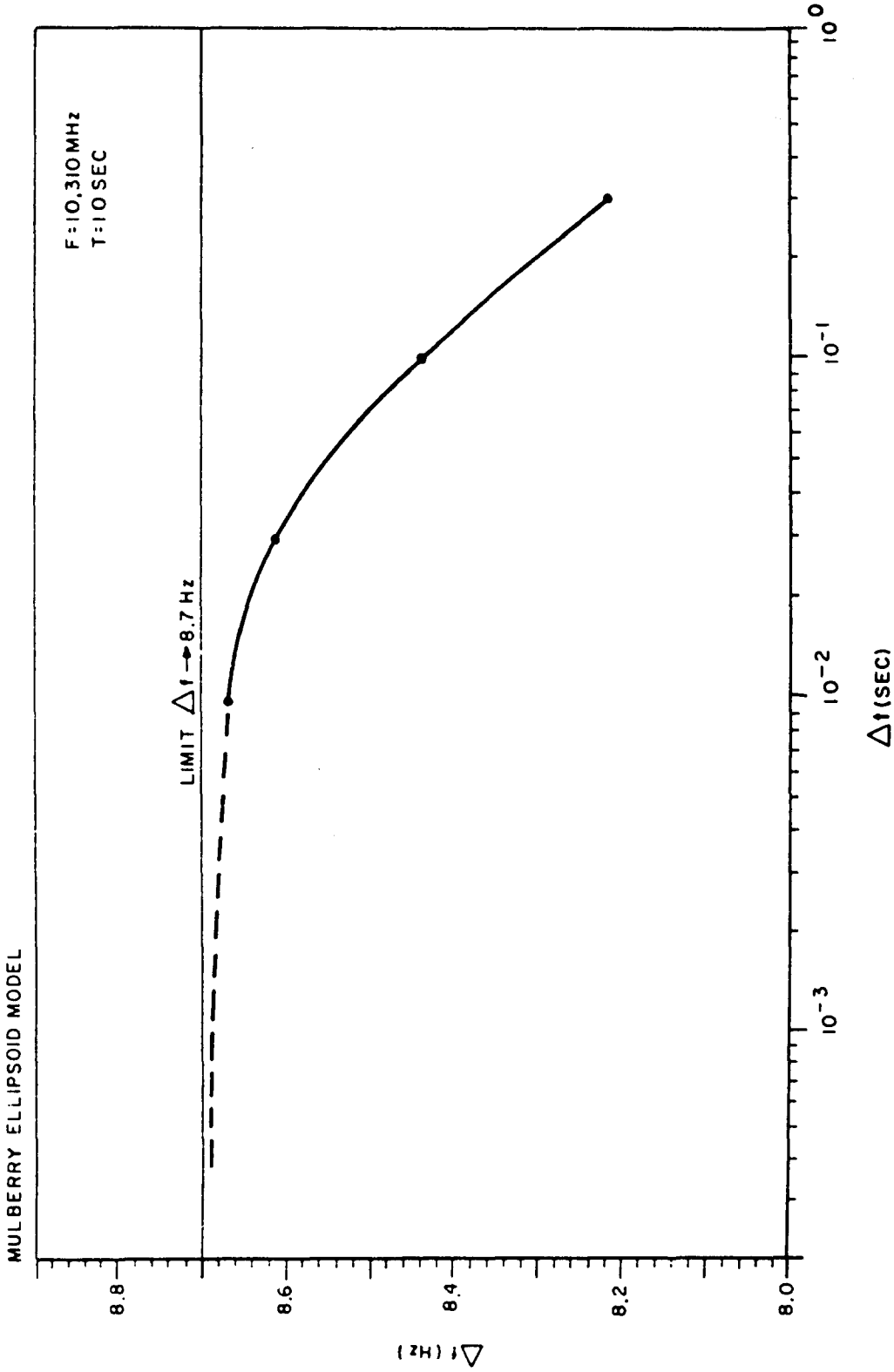


Figure 4-7 Illustrate the Limiting Process Involved in Obtaining the Doppler Shift from the Path Difference Calculation

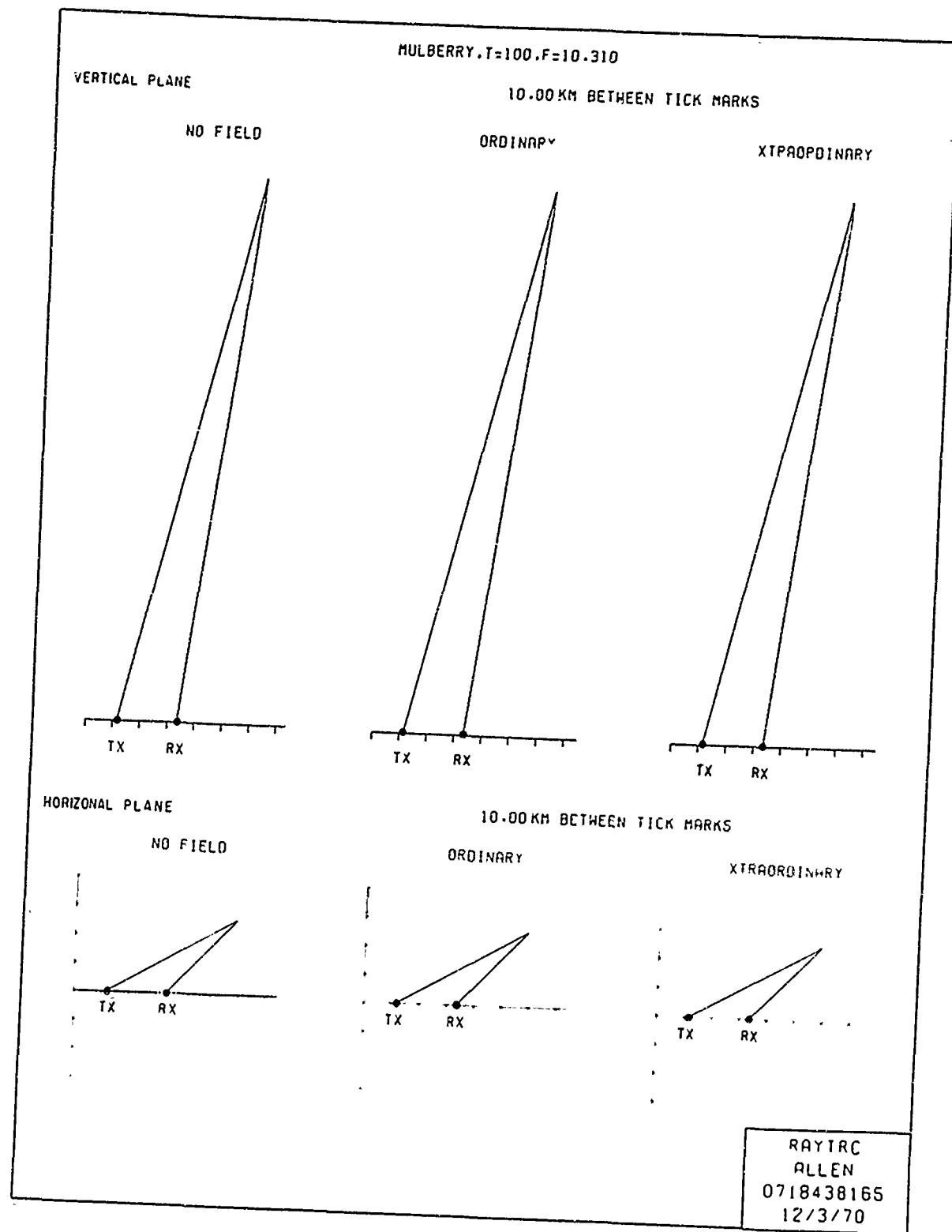


Figure 4-8 Ray Path Projection Plots in Both Vertical and Ground Planes at 100 Seconds After Release for the Three Modes, No Field, Ordinary and Extraordinary, at $F = 10.31$ MHz

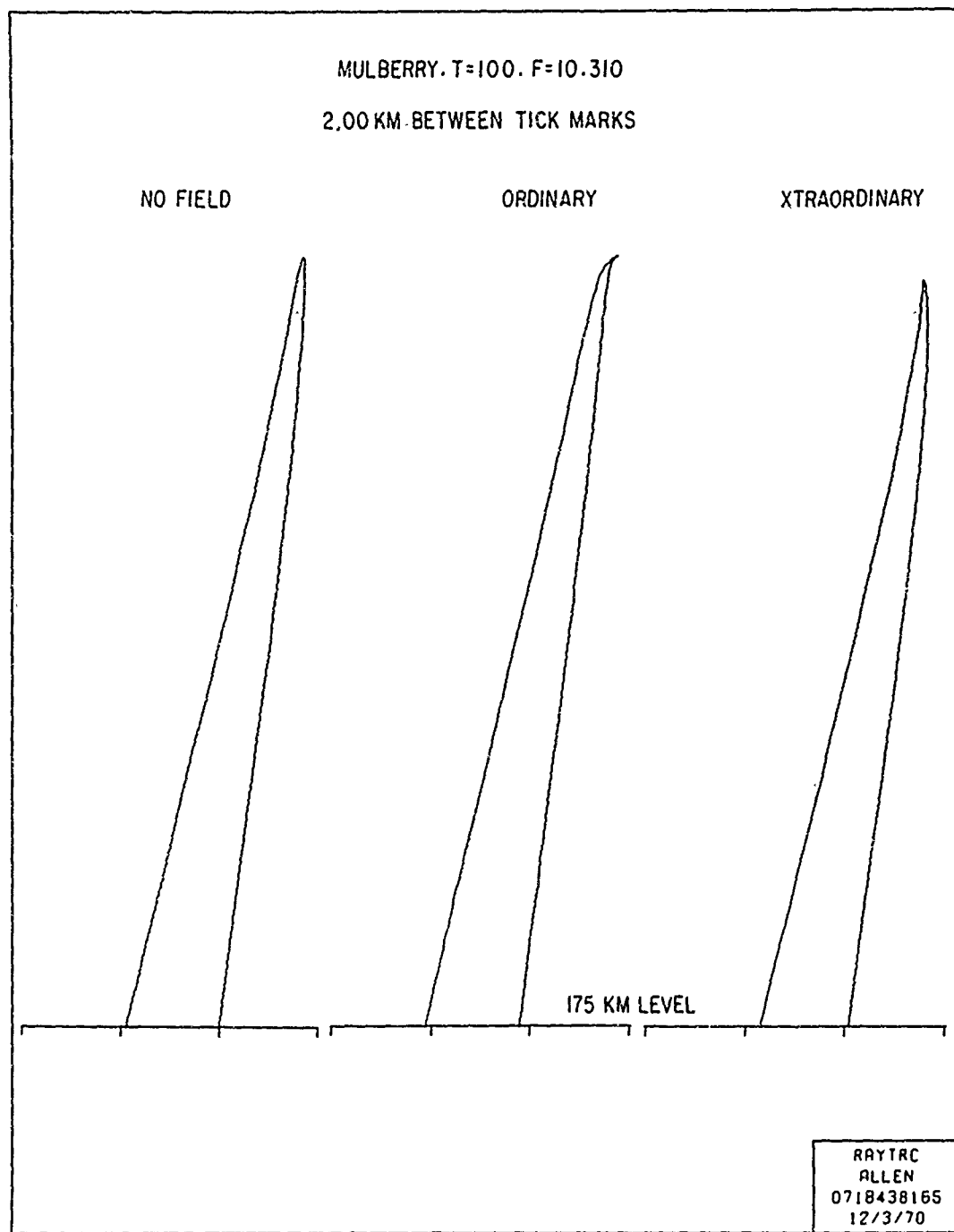


Figure 4-9 The Vertical Ray Path Segments Close to the Reflection Level to Show How the Three Modes Refract Through the Denser Regions of the Cloud

The movement of the reflection point with respect to the center of the cloud and the refraction suffered by the rays as function of time are shown in Figures 4-10a, b and c and 4-11a and b in terms of the azimuth and elevation angles of the cloud center, the reflection point and of transmission. It can be seen that the direction of the reflection point walks away from the center during the expansion phase as the cloud becomes elongated and walks back at later times as the reflection surface recedes toward the center. The deviations in azimuth and elevation due to refraction are of some importance and are therefore plotted separately in Figure 4-12. The refraction in the case of no-field ray is entirely due to the density gradients in the ionization at levels below the height of reflection. The deviation is nearly zero at the beginning and increases continuously at a rate that builds up rapidly with time. The O and X rays undergo refraction that is partly due to density gradients and partly due to the magnetic field. The refraction effects due to density gradients and the magnetic field are found to act in the same direction for the X ray while they get cancelled partially for the O ray. The curves for the O ray pass through zero indicating the time when the two effects cancel each other exactly. The refraction is found to be the highest for the X ray with azimuth and elevation deviations of 1.65° and -0.35° respectively (the $\Delta\phi$ is in the ground plane and should be multiplied with $\cos \beta$ to obtain it in the transmission plane). The cross over of the curves for the no-field and the X ray is due to the fact that the deviations increase most rapidly at the time of penetration which comes slightly earlier for the no-field ray.

The defocussing nature of the cloud is illustrated in Figures 4-13 to 4-16. The ray plots shown are for the frequency of 10.31 MHz and for the time of 180 seconds after release. The plots are projections of the ray paths on the ground and the vertical plane

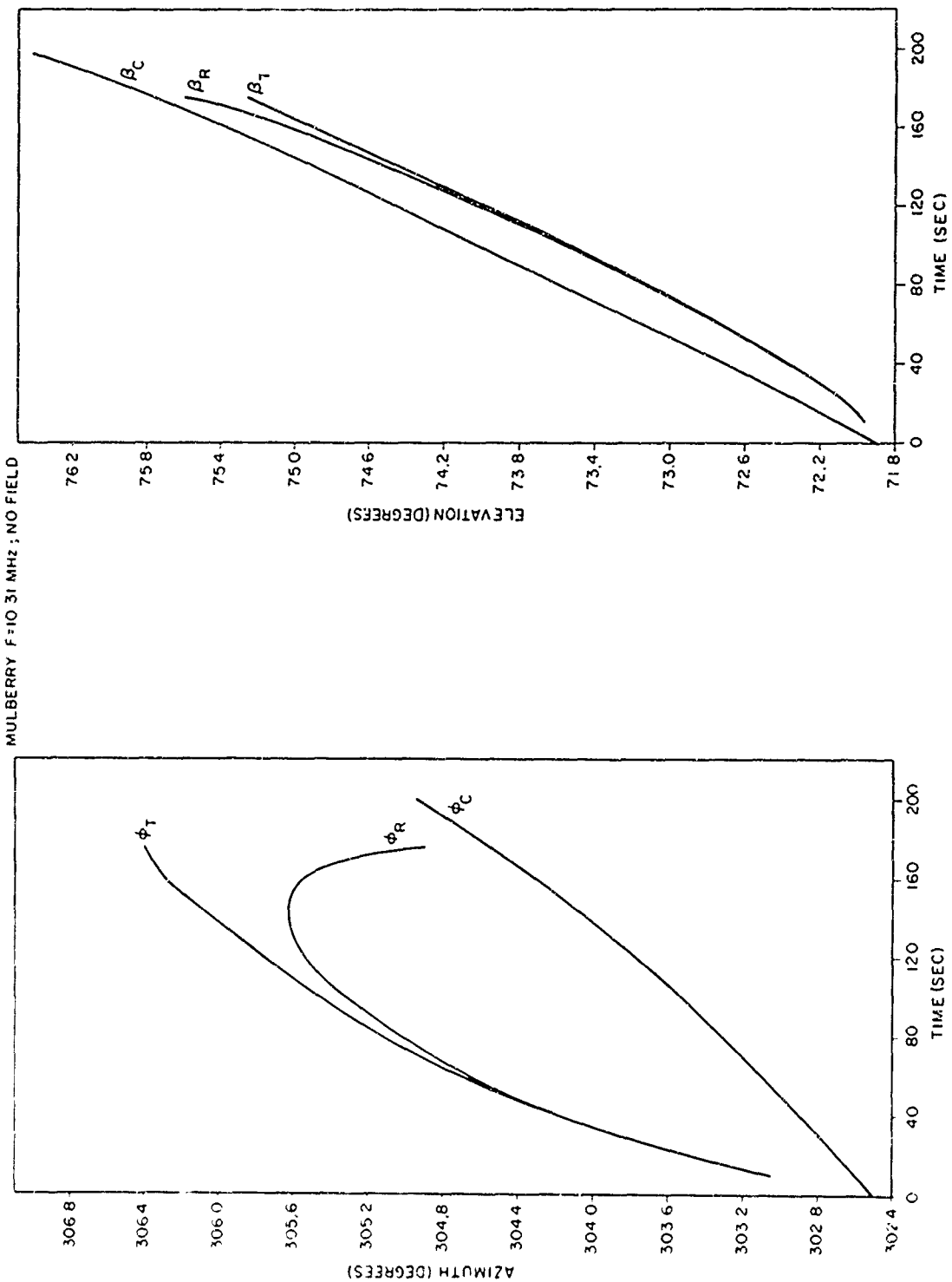


Figure 4-10a The Azimuth and Elevation Angles of Transmission (ϕ_T, β_T) and Reflection Point (ϕ_R, β_R) for no Field Ray at $F = 10.31$ MHz Along with that of the Cloud Center (ϕ_C, β_C)

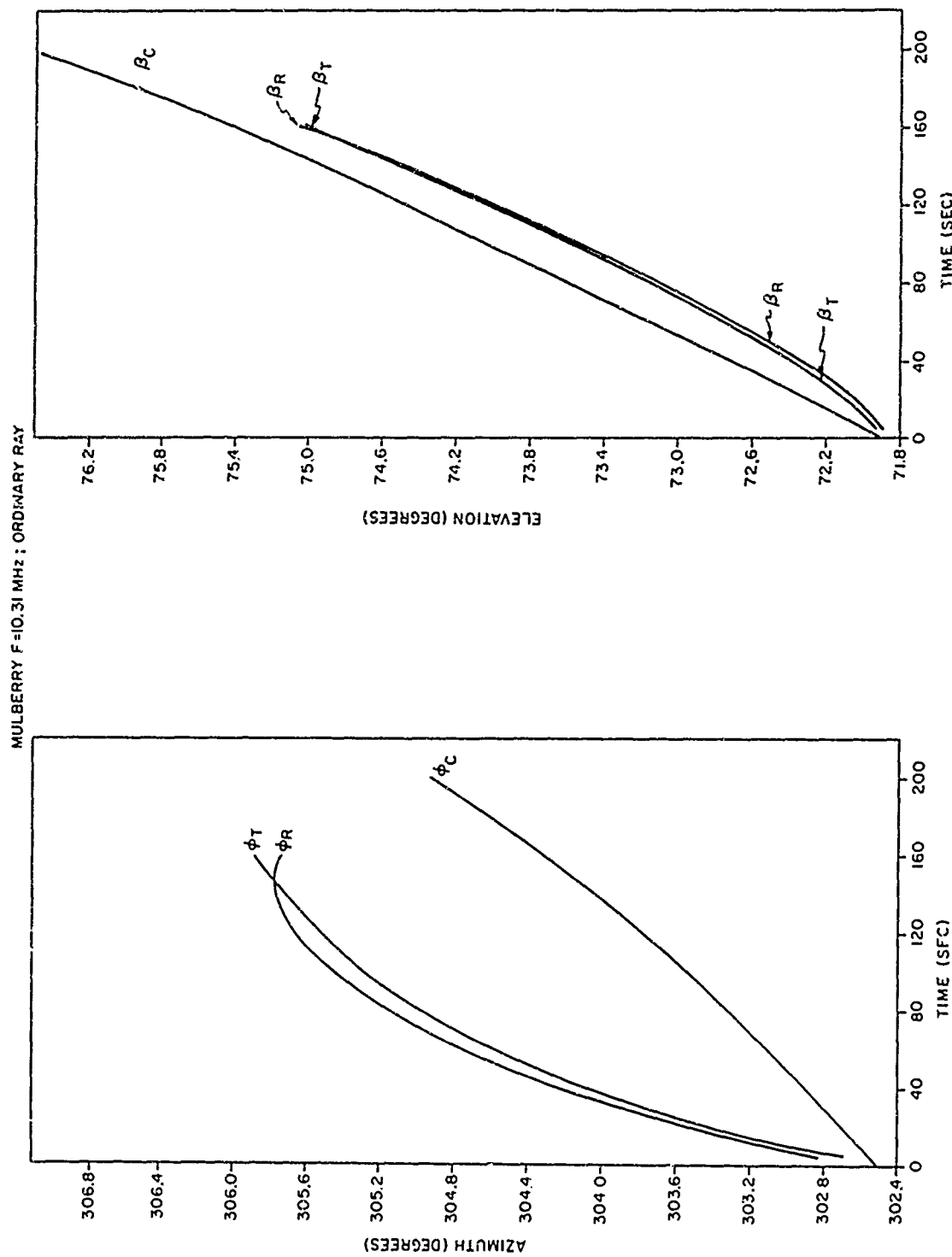


Figure 4-10b The Azimuth and Elevation Angles of Transmission (ϕ_T, β_T) and Reflection Point (ϕ_R, β_R) for Ordinary Ray at $F=10.31$ MHz Along with that of the Cloud Center (ϕ_C, β_C)

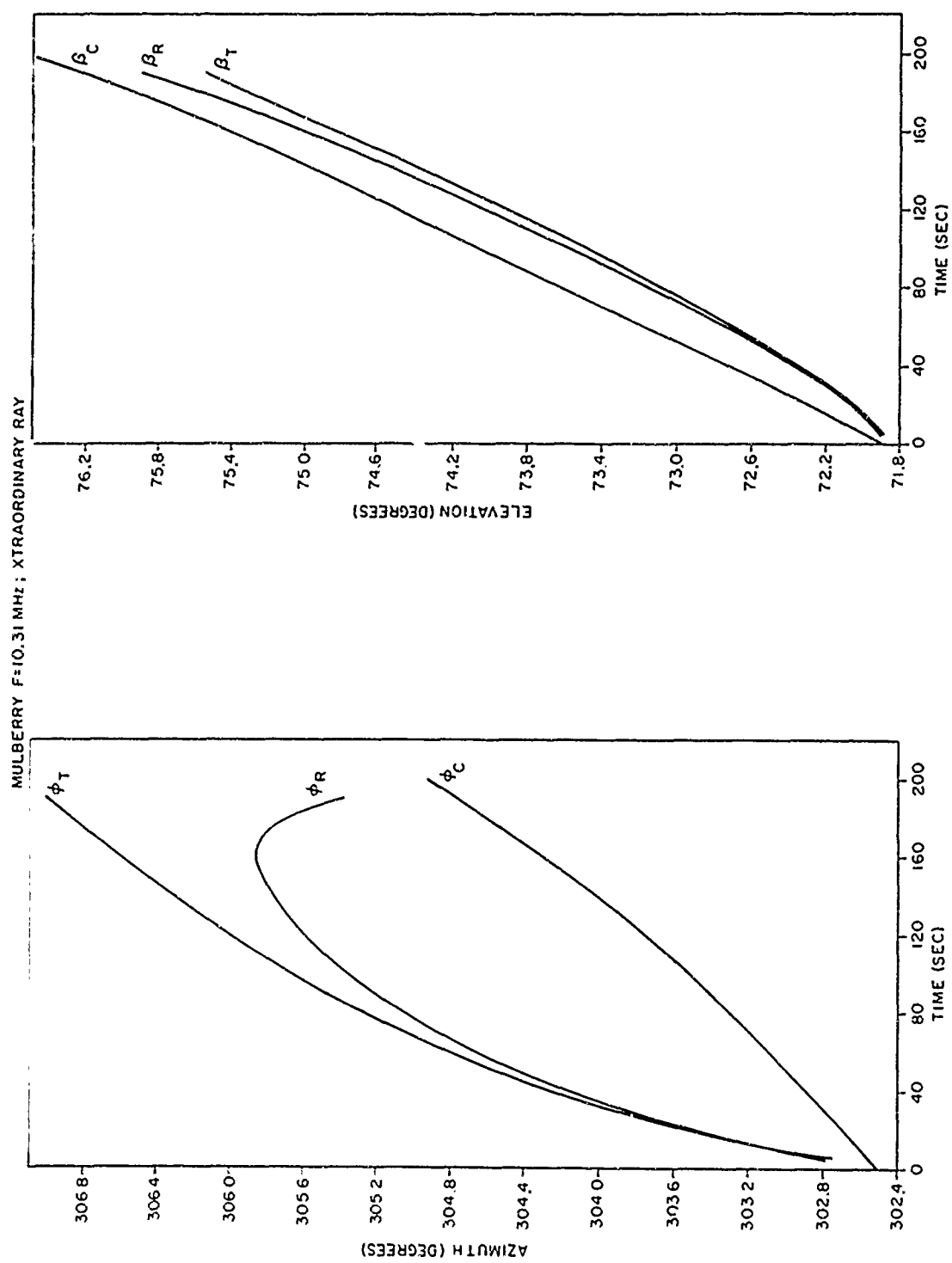


Figure 4-10c The Azimuth and Elevation Angles of Transmission (ϕ_T, β_T) and Reflection Point (ϕ_R, β_R) for Extraordinary Ray at $F = 10.31$ MHz Along with that of the Cloud Center (ϕ_C, β_C)

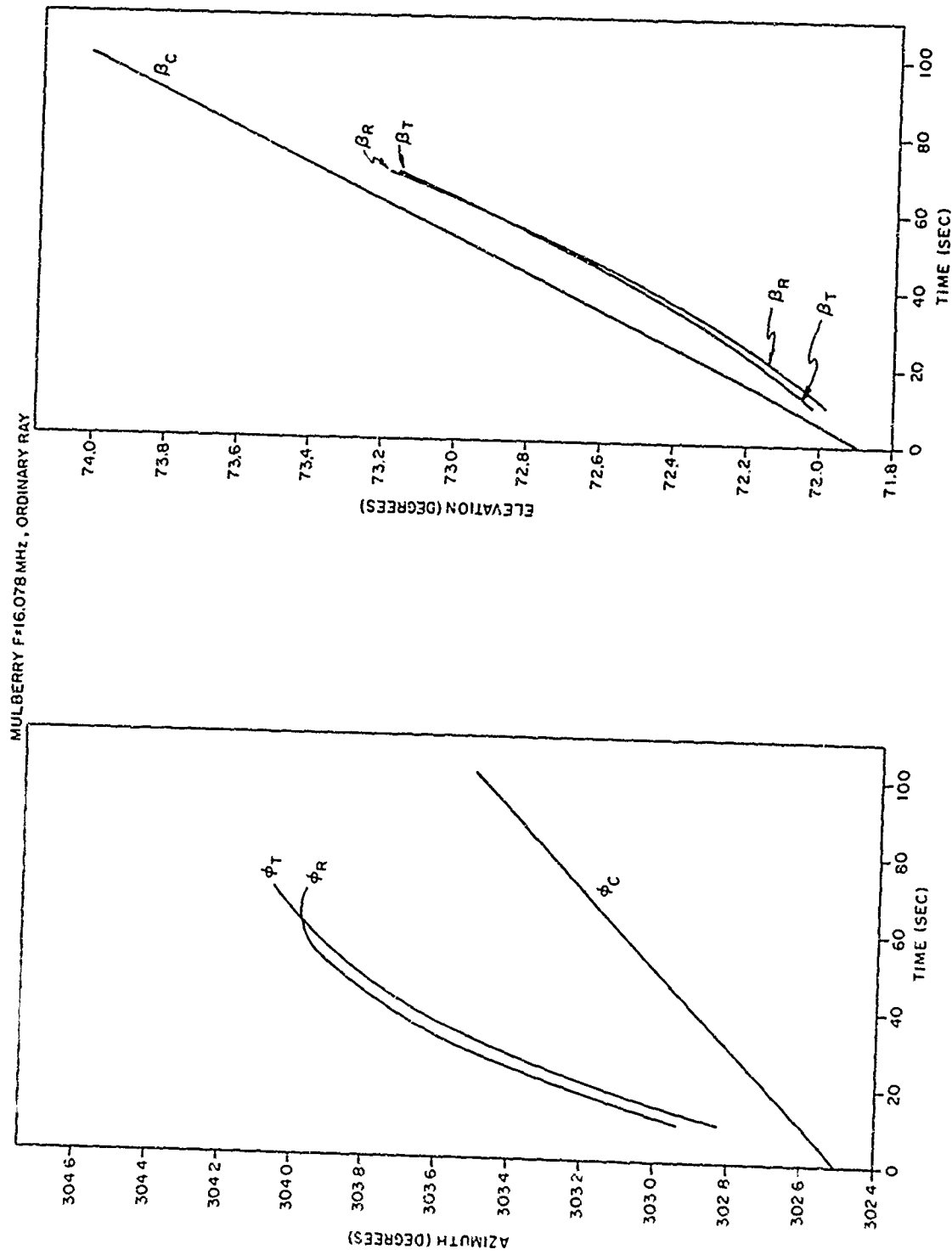


Figure 4-11a The Azimuth and Elevation Angles of Transmission (ϕ_T, β_T) and Reflection Point (ϕ_R, β_R) for the Ordinary Ray at $F = 16.078$ MHz Along with that of the Cloud Center (ϕ_C, β_C)

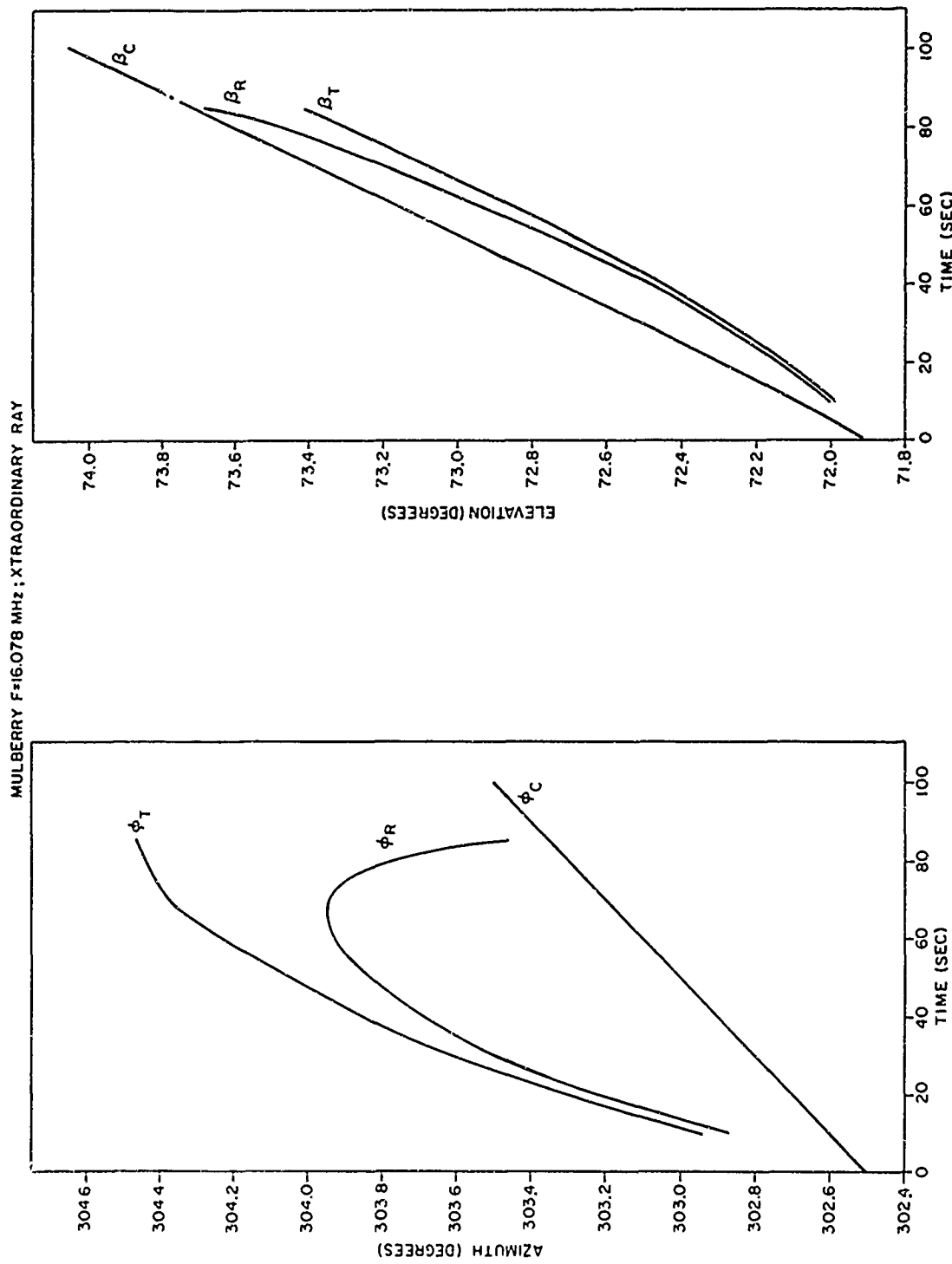


Figure 4-11b The Azimuth and Elevation Angles of Transmission (ϕ_T, β_T) and Reflection Point (ϕ_R, β_R) for the Extraordinary Ray at $F = 16.078$ MHz Along with that of the Cloud Center (ϕ_C, β_C)

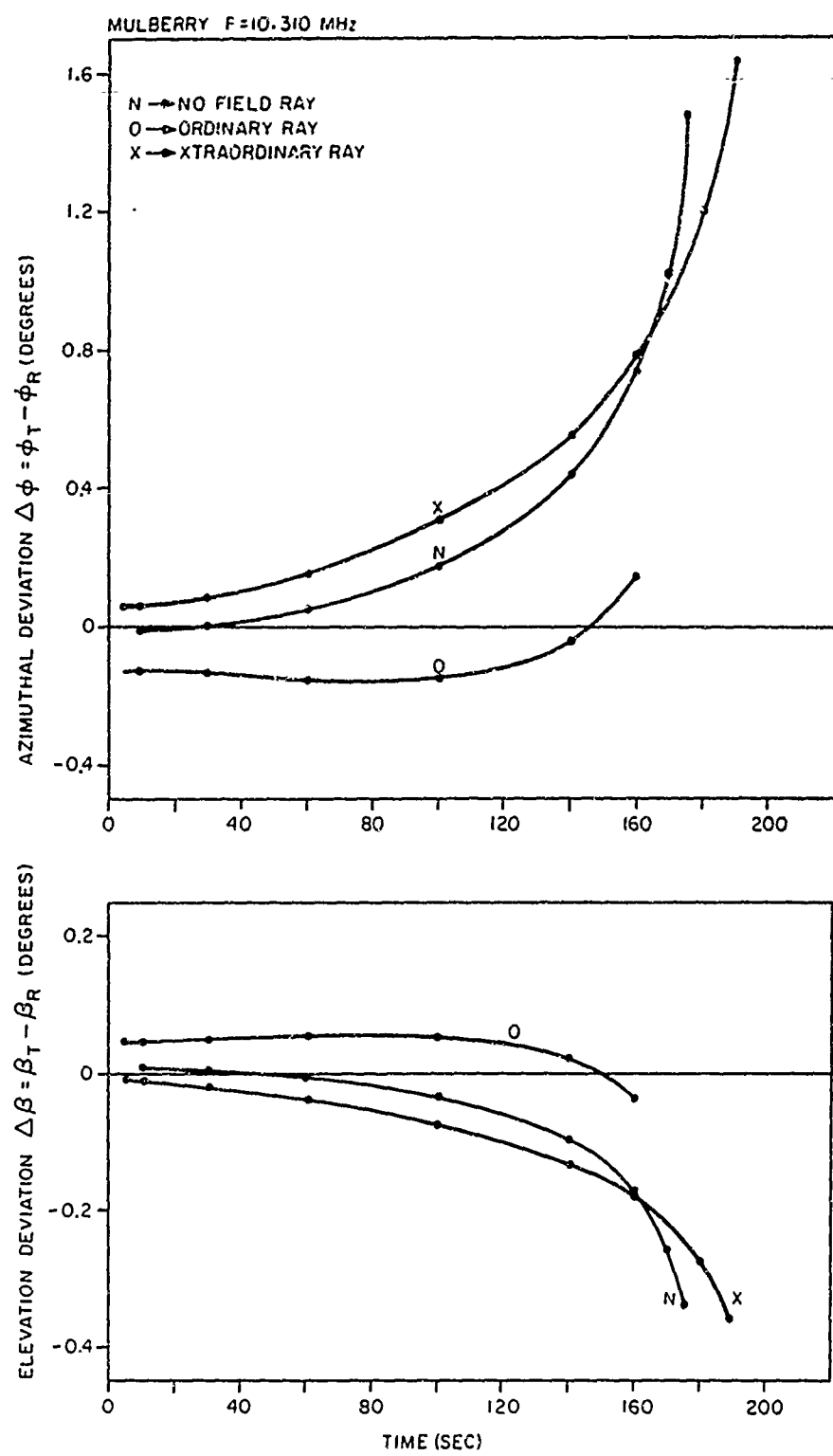


Figure 4-12 The Azimuth and Elevation Angle Deviations Suffered by the Three Modes Due to Refraction up to the Reflection Level at $F = 10.31$ MHz

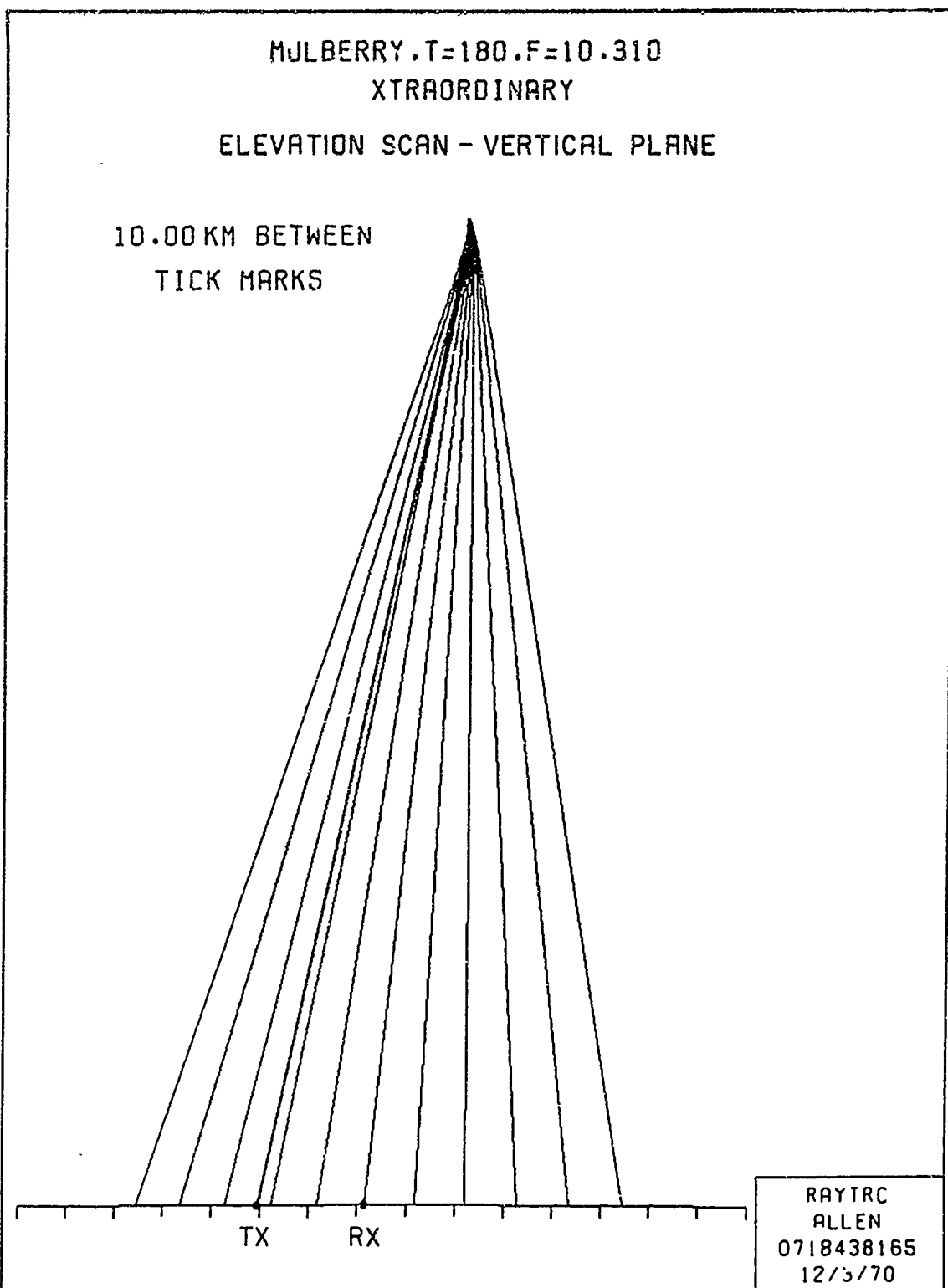


Figure 4-13 Ray Path Projections in Vertical Plane of a Fine Bundle of Eleven Rays (Appears as Thick Line on the Plot) Transmitted Over an Elevation Scan Interval of 0.02° . The Spread of the Rays on Reflection Illustrate the Defocussing Effects of the Cloud

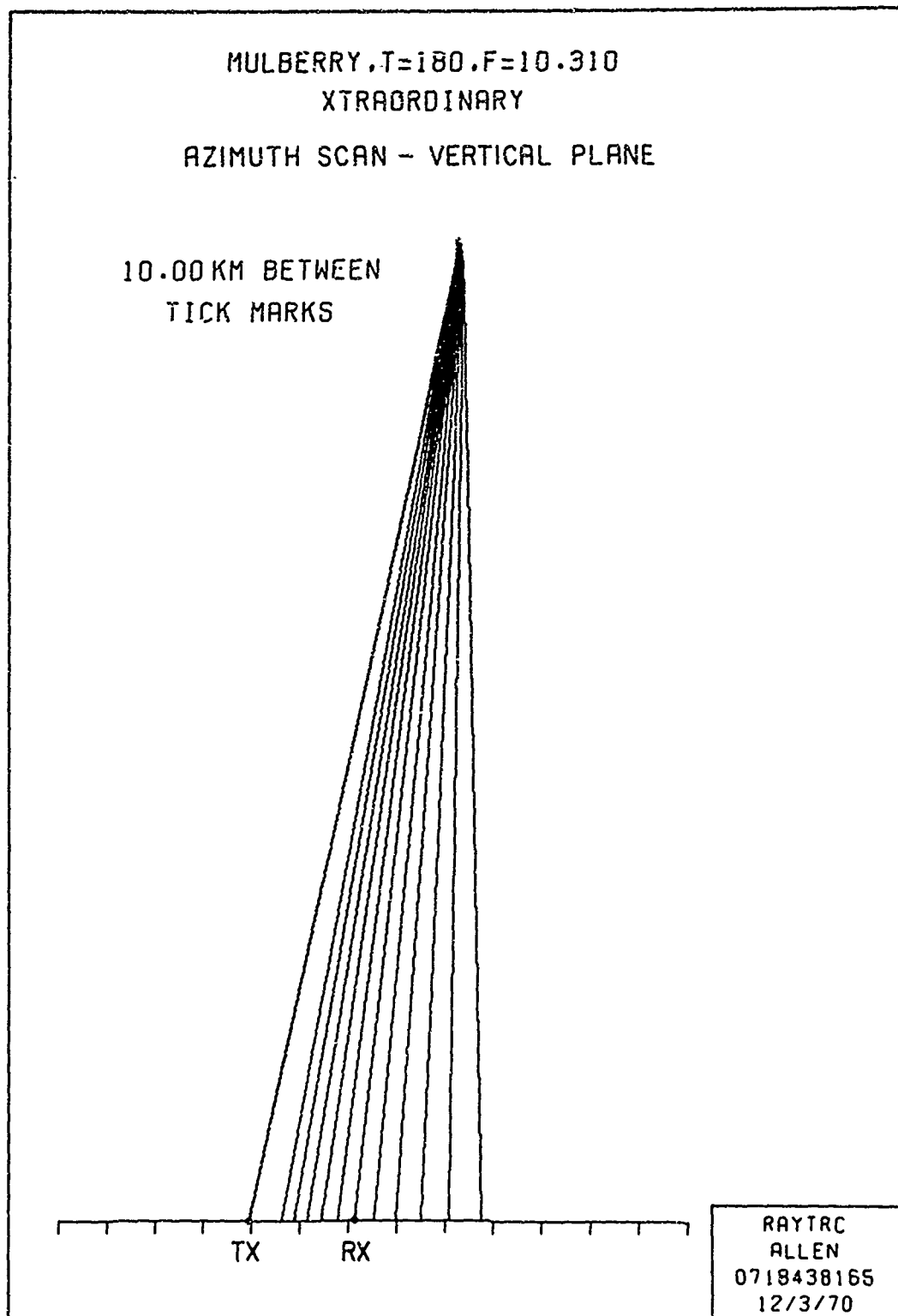


Figure 4-14 Ray Path Projections in Vertical Plane of a Fine Bundle of Eleven Rays (Appears as Thick Line on the Plot) Transmitted over an Azimuth Scan of Size 0.025°. The Spread of the Rays on Reflection Illustrate the Defocussing Effects of the Cloud

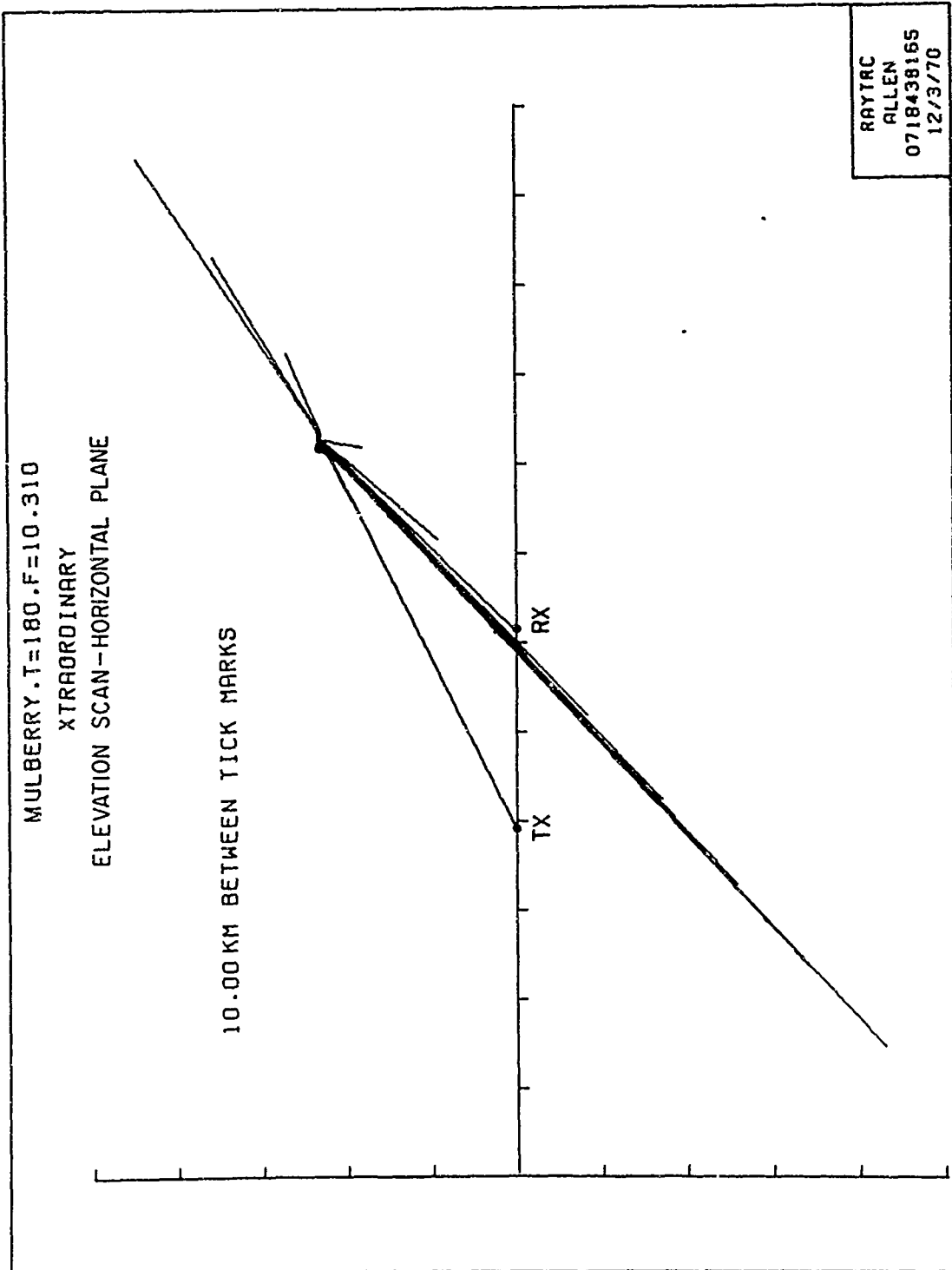
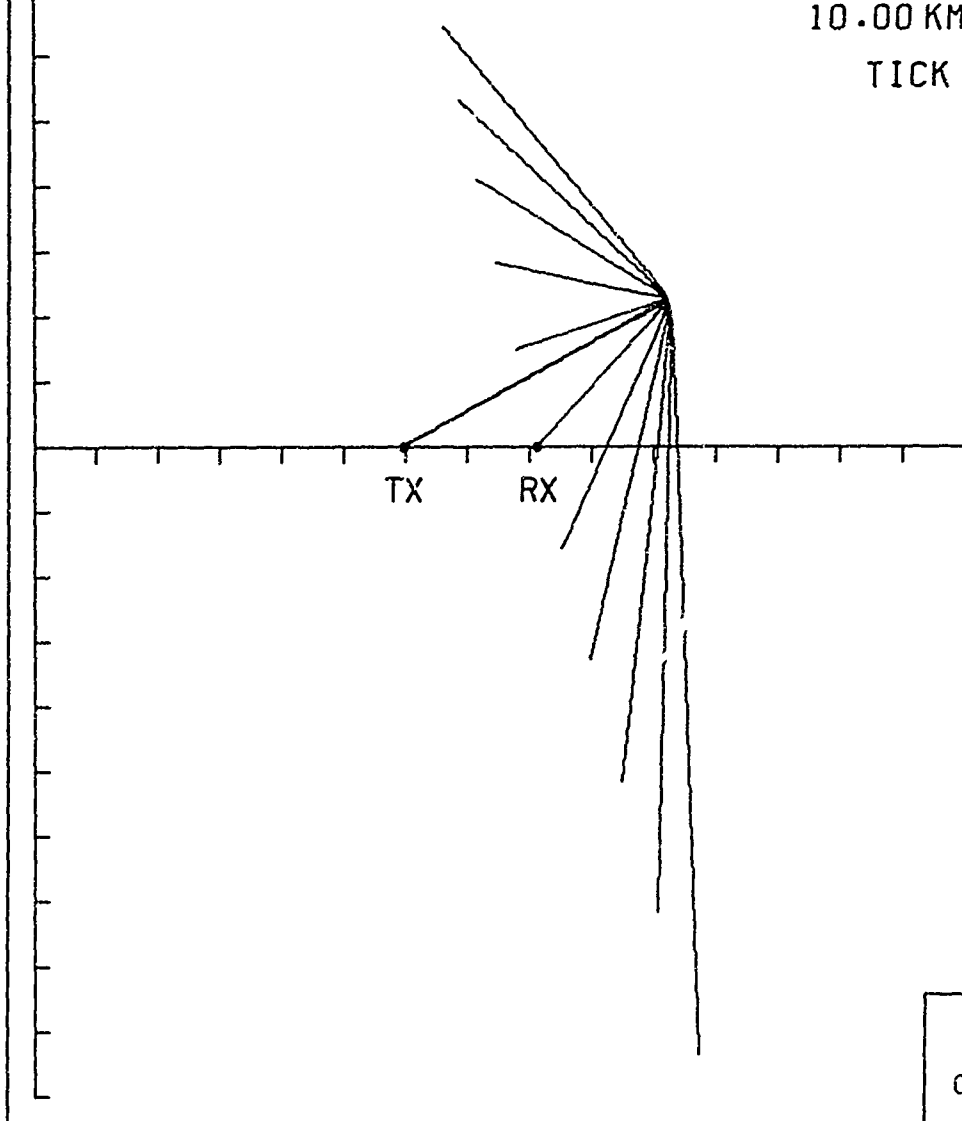


Figure 4-15 Ray Path Projections on the Ground Plane of a Fine Bundle of Eleven Rays
 (Thick Line on the Plot from TX) Scanned in Elevation by 0.02 Degree

MULBERRY.T=180,F=10.310
XTRAORDINARY
AZIMUTH SCAN - HORIZONTAL PLANE

10.00 KM BETWEEN
TICK MARKS



RAYTRC
ALLEN
0718438165
12/3/70

Figure 4-16 Ray Path Projections on the Ground Plane of a Fine Bundle of Eleven Rays (Thick Line on the Plot from TX) for an Azimuth Scan of Size 0.025°

connecting the transmitter and the receiver. They describe how a narrow beam of incident energy confined either to an elevation plane or an azimuth plane become defocussed on reflection from the cloud. The beam sizes $\Delta\phi \cos \beta$ and $\Delta\beta$ represented by the scans in azimuth and elevation are respectively 0.025 degrees and 0.02 degrees. They are so narrow in extent that they could be seen only as a thick line on the plots. The energy dispersion on the ground is found to be to an extent of about 130 km and 160 km corresponding to the elevation and azimuth scans of the ground plane plots. The spreading of the rays due to the defocussing effects of the cloud in this case are greater by a factor of about 8×10^5 relative to free space spreading. The defocussing effects are not uniform over the entire illuminated area since the rays, while equally incremented in the scan, seem to bunch closer in certain areas. It should be mentioned that some of the bunching effect seen especially with the azimuthal scan in the vertical plane is due to the distortion resulting from the projection. The cloud is found to become increasingly more defocussing with time as it gets more and more elongated. On the basis of the impact area calculation described in paragraph 4.1, it is found that the defocussing factor (relative to free space) for the X ray at 10.31 MHz increases from 7.6×10^3 to 1.85×10^7 over the interval 5 to 190 seconds. It will increase from 2.27×10^4 to 1.47×10^8 in the interval 10 to 85 seconds for 16.078 MHz.

The Doppler and the scattering cross section results synthesized by the ray tracing technique are presented in Figures 4-17 and 4-18 for the two operating frequencies 10.31 MHz and 16.078 MHz. In addition to the ordinary and extraordinary modes, results have been obtained also for the no-field case for 10.31 MHz to study the magnetic field effects. The shapes of the curves showing the variation of the Doppler and the cross section with time are found to be

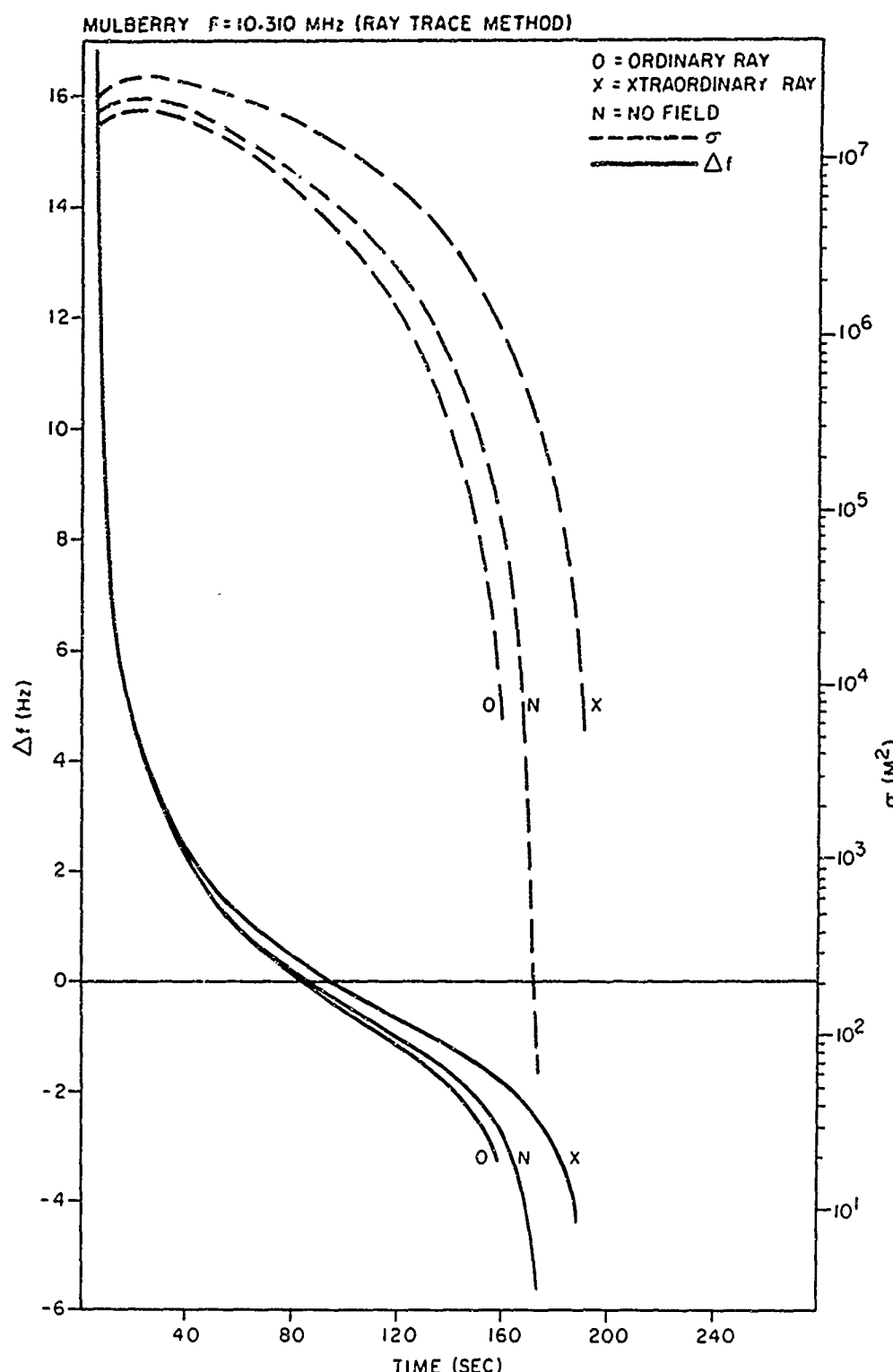


Figure 4-17 The Time History of the Doppler Shift and the Scattering Cross Section Synthesized by the Ray Tracing Method for No-Field, Ordinary and Extraordinary Modes at $F = 10.31$ MHz

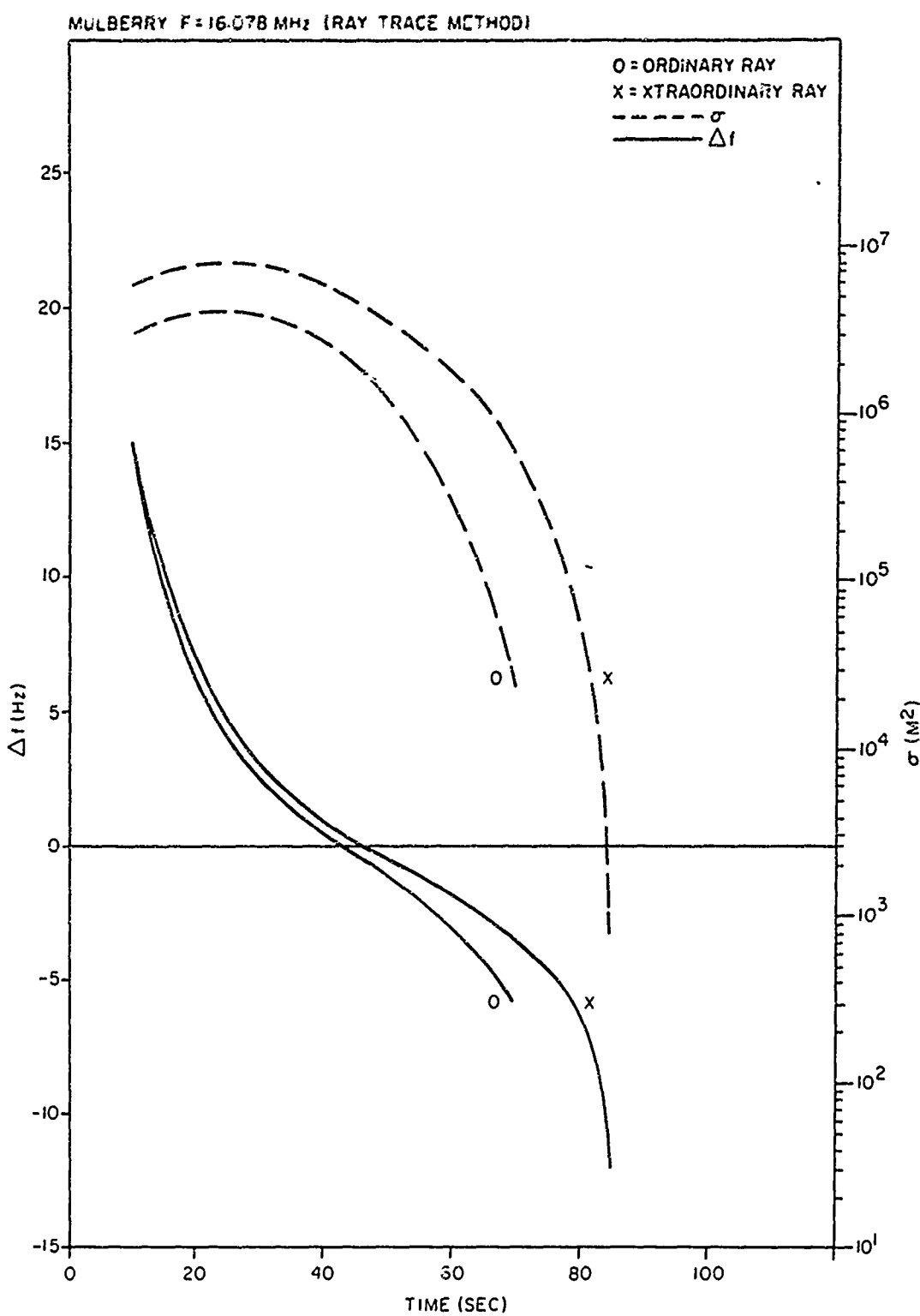


Figure 4-18 The Time History of the Doppler Shift and the Scattering Cross Section Synthesized by the Ray Tracing Method for Ordinary and Extraordinary Modes at $F = 16.078$ MHz

identical for all the three modes. The Doppler and the cross section variations for the X mode lag in time to that of the O mode. The lag in Doppler widens as the cutoff times are approached. The variations for the 'no field' (N) fall in between that of the O and X, but closer to the O mode. The differences between the O and X modes are primarily due to the fact that they are supported by two plasma frequency surfaces whose expansion rates are changing relative to each other with time. The plasma frequency contour supporting the O and N modes being the same, the differences between these two indicate the effects due to the magnetic field. At the operating frequency of 10.31 MHz the Doppler shift falls from 17 to -5 Hz in the time interval of 5 seconds after release to the cutoff. The cross-over from positive to the negative Doppler occurs roughly halfway in the time interval. The scattering cross section reaches a maximum of about $2 \times 10^{-7} \text{ m}^2$ within 20 to 30 seconds after release and thereafter falls continuously at a rate that increases rapidly with time. It implies that the signal drops out rather abruptly. The results for 16.078 MHz share all the basic features observed for 10.31 MHz. The peak scattering cross section at 16.078 MHz is found to be smaller than at 10.31 MHz by a factor 5 for the ordinary ray and 4 for the extraordinary ray.

4.3.2 COMPARISON WITH ELLIPSOID MODEL

The Doppler and the scattering cross section have been calculated also for the field aligned ellipsoid model using the method described in paragraph 4.2. The results are presented in Figures 4-19 and 4-20. The curves denoted by O and X in these figures represent two slightly different operating frequencies which correspond to the plasma frequencies appropriate to the ordinary and the extraordinary modes. The comparison between the ellipsoid model and the ray tracing is intended to bring out the effects on the Doppler and the scattering cross section due to magnetic field and the ionization lying below

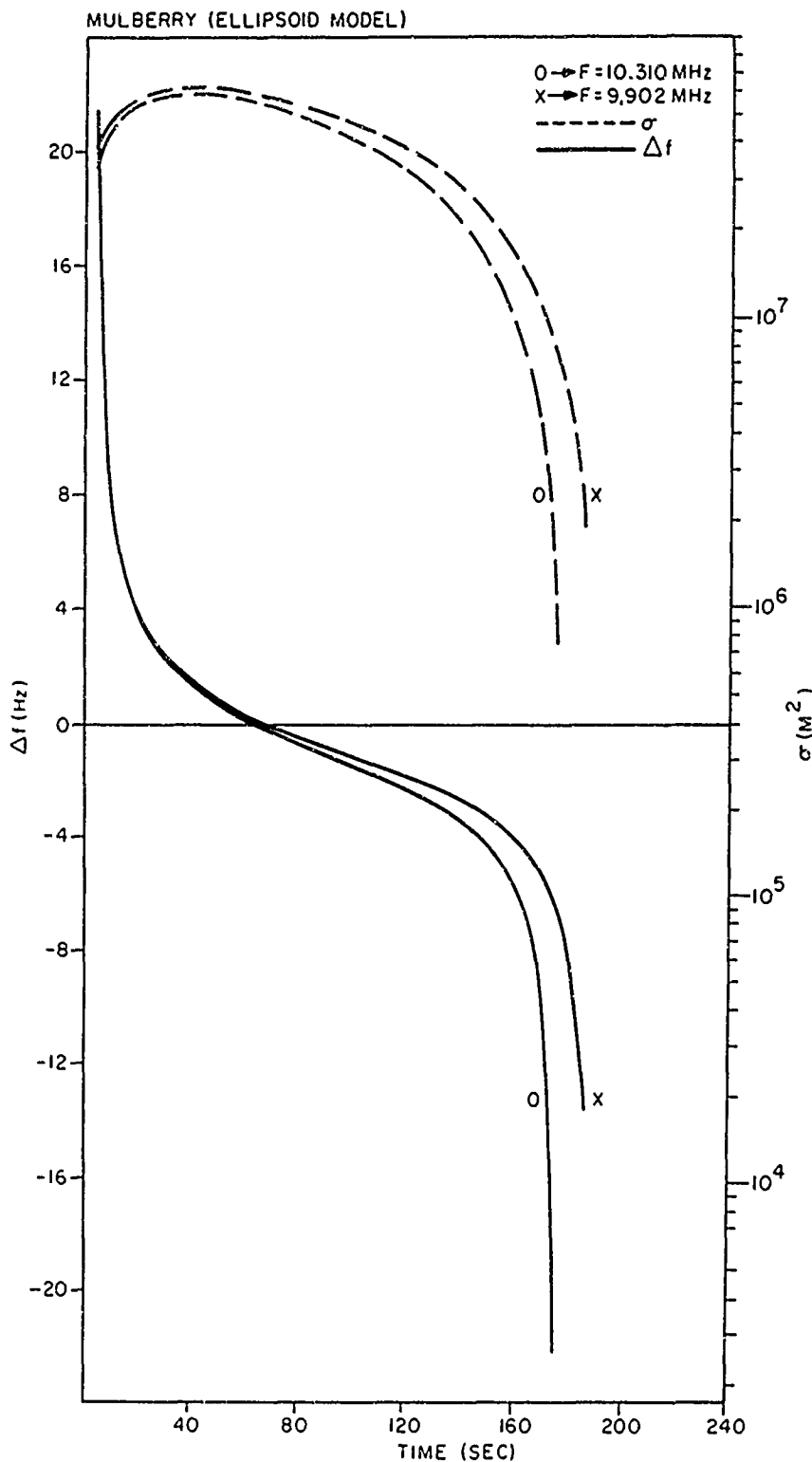


Figure 4-19 The Time History of the Doppler Shift and the Scattering Cross Section Synthesized by the Hard Ellipsoid Method for $F = 10.31$ and 9.902 MHz . (The Two Frequencies Correspond to the Plasma Frequencies that Support the O and X Modes)

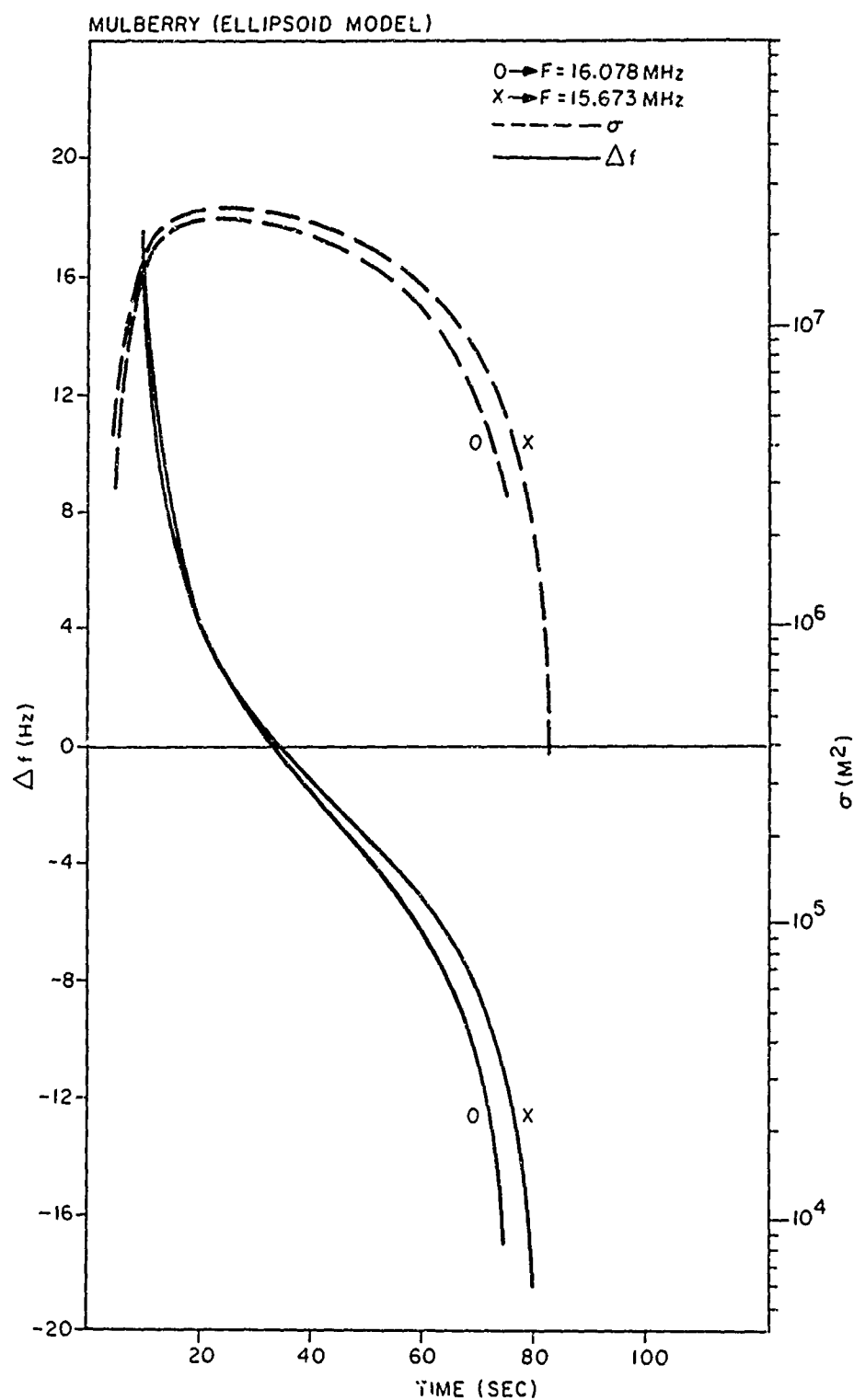


Figure 4-20 The Time History of the Doppler Shift and the Scattering Cross Section Synthesized by the Hard Ellipsoid Method for $F = 16.078$ and 15.673 MHz. (The Two Frequencies Correspond to the Plasma Frequencies that Support the O and X Modes)

the reflection level. The general shapes of the curves showing the temporal variations of the two parameters are similar for both the models. Considering in detail, the Doppler variations are significantly steeper for the ellipsoid model than for the ray tracing. The negative phase of the Doppler is much more pronounced for the ellipsoid model with the transition from positive to negative occurring significantly earlier than for ray tracing. The transition occurs for the ellipsoid model at about the same time as the scattering cross section begins to decrease whereas it lags a short while with ray tracing. This suggests that an effect of the underlying ionization is to hold the Doppler positive for a short duration even after the contraction phase of the reflection surface is initiated. It causes also the tailing effect of the Doppler to be significantly inhibited. The defocussing effects of the underlying ionization which enhance with time cause a remarkable reduction in the scattering cross section of the cloud. The ray tracing technique yields a cross section which is smaller by a factor that increases with time from 3 at the peak to 30 at the time just prior to penetration. The comparison thus leads to the conclusion that the simple hard ellipsoid model is inadequate for an accurate synthesis of the hf radar signatures.

SECTION 5. EXPERIMENTAL RESULTS

5.1 TEST GEOMETRY AND INSTRUMENTATION

The Pre-SECEDE Series of Barium release tests were conducted during the fall of 1969 at White Sands Missile Range, New Mexico. The releases were observed by nine hf radar systems of which eight (6 pulse and 2 cw) had been operated by Raytheon with transmitters located at Paxton Siding and receivers located at Twin Butes. Figure 5-1 shows the geometry of the radar sites with respect to the

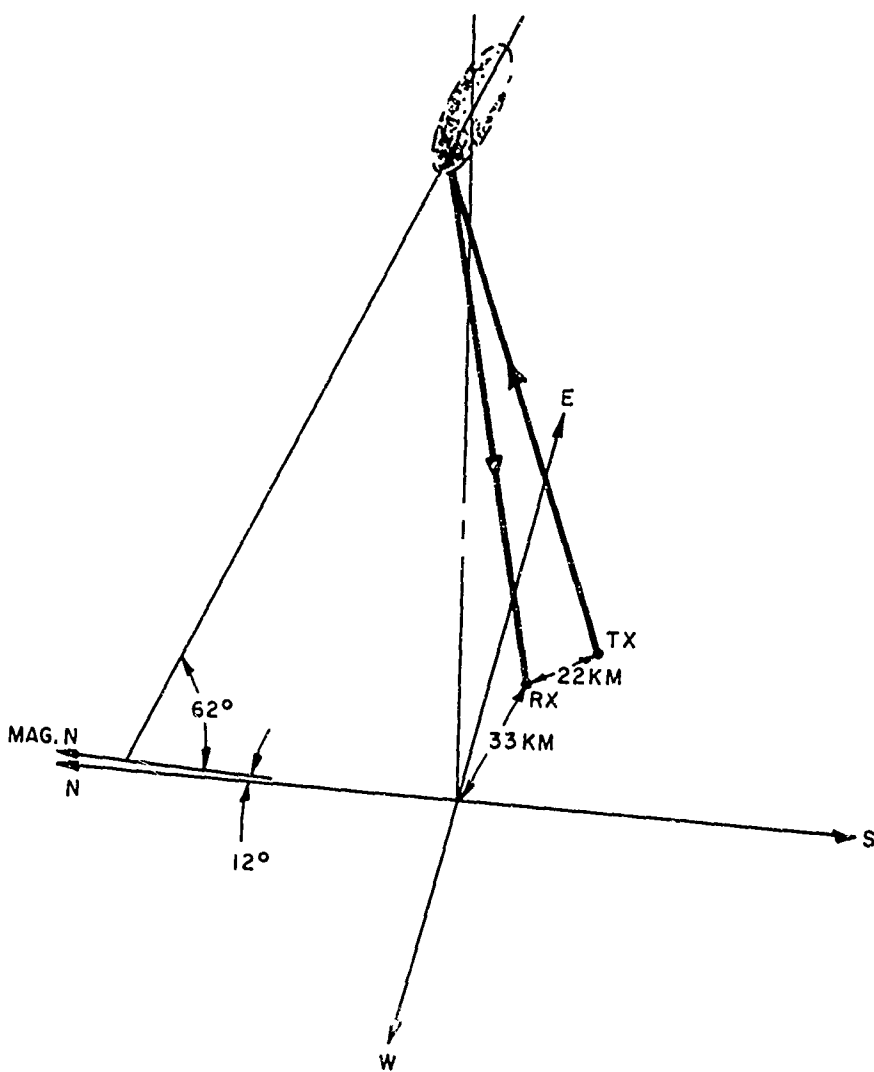


Figure 5-1 Illustration to Show the Cloud Geometry With Respect to the Transmitting (TX) and Receiving (RX) Stations

position of the plasma cloud at release for the test Mulberry. The discussion of the results presented in this section is limited to the pulse measurements made at 10.31 and 16.078 MHz for which the ray tracing synthesis has been done.

The radars employed in the experiments are the conventional Phase Path Sounders with the transmitting and the receiving systems phase locked to stable frequency standards at each site. This enables both phase and amplitude of the received signal to be obtained from the observations. The pulse radars had been operated at a 40 pps rate with a pulse width of 150 μ s. For receiving, a bandwidth 10 kHz was used and the output signal was recorded on analog magnetic tape at a 15 kHz i-f level for later processing. The antennas used for transmitting 10.31 and 16.078 MHz were vertically directed deltas. At the receiving site, a delta antenna was used for receiving at 10.31 MHz and a vertically directed log periodic antenna for receiving at 16.078 MHz.

5.2 EXPERIMENTAL DATA

The experimental data recorded on the tape is reduced to the form of doppler spectra. The signature display format is such that the time runs from left to right, Doppler shift runs from bottom to top and the strength of the echo is represented by the darkness of the trace. The signal processing involves phase detection of the i-f signal run off from the tape which is then range gated and sampled at the pulse repetition rate. The sampled signal results in a box-carved waveform which is fed into a UA-6A spectrum analyzer to obtain the desired Doppler signature display. The unambiguous window of the Doppler spectrum is equal to half the pulse repetition frequency which

in this case is 20 Hz. The Doppler components that fall outside the range fold back into the window and cause images to appear along with the real spectral components. Figure 5-2 shows the Doppler signatures obtained on 10.31 and 16.078 MHz for the test Mulberry. The true signature is simply a single monotonically descending tone and during the first few seconds when the Doppler falls outside the unambiguous window an image appears as labeled on the figure. The frequency folding takes place about 10 Hz instead of 20 Hz since the signal is phase detected with an offset frequency of 10 Hz. The periodic notches that appear on the traces were identified as due to Faraday fading of the received signal.

The spectrally analyzed signal can be displayed also in the form of amplitude spectral cuts in time to measure the received power of the signal and thereby determine the scattering cross section of the cloud as function of time. The sequence of spectra obtained have a time resolution of 1.5 seconds for both 10.31 and 16.078 MHz. Figures 5-3 and 5-4 show the spectral sweeps for selected times for the two frequencies. The signal spikes appear in pairs because of the imaging of the spectral components about the folding frequency of 10 Hz. The signal amplitudes are subject to nonuniform weighting in frequency imposed by the method of sampling. The weighting function is $\sin X/X$ where X is equal to $\omega\tau/2$ while ω is the angular frequency and τ is the sampling time. The amplitudes scaled from the spectra are corrected for the nonuniform response. A test signal injected into the receiver at the operating frequency in 5 dB steps from a reference power level is used for calibrating the amplitude scale. Figure 5-5 shows the calibration curves constructed for 10.31 and 16.078 MHz for converting the arbitrary amplitude readings to absolute signal power.

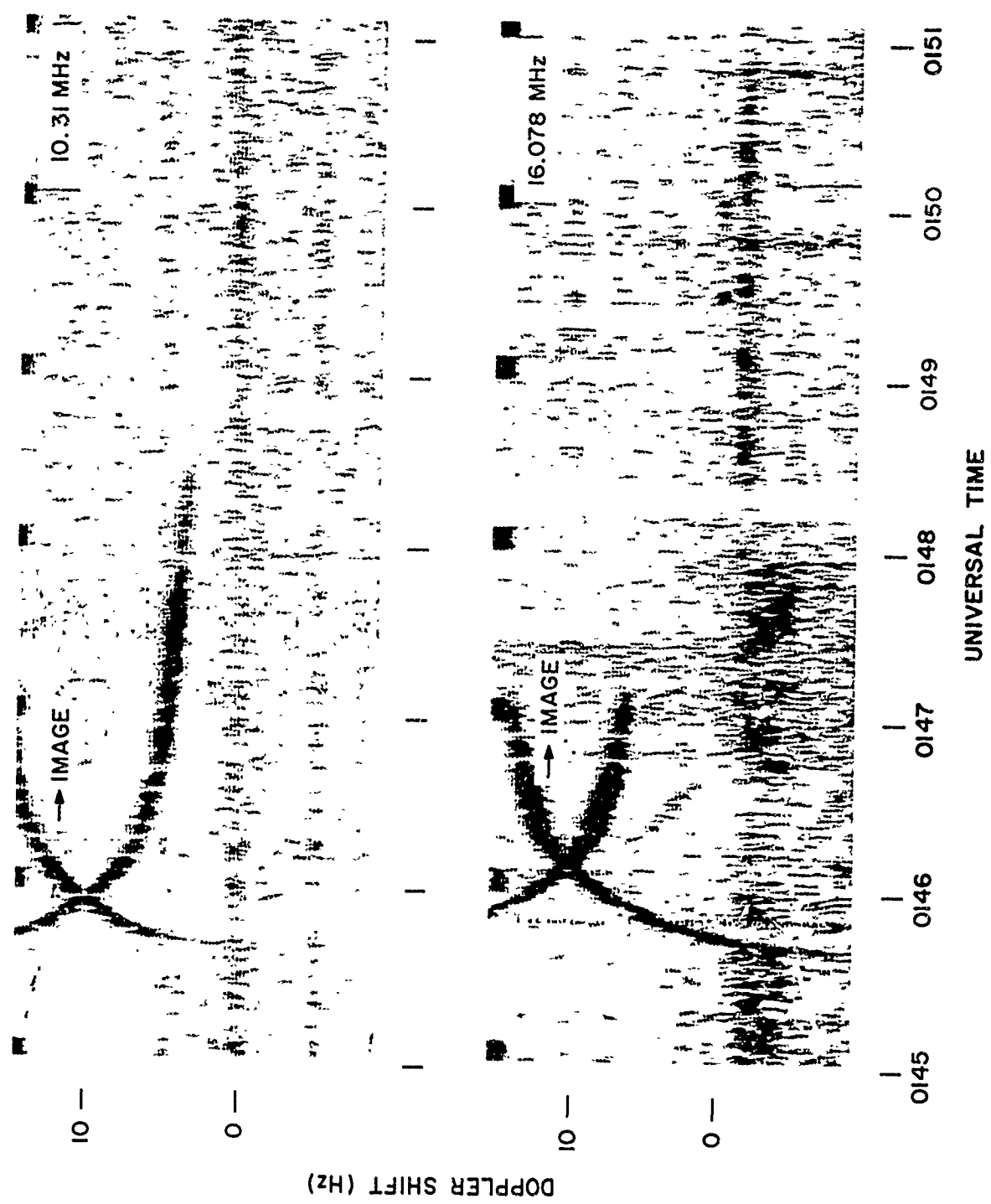


Figure 5-2 The Observed Doppler Signatures at $F = 10.31$ and 16.078 MHz for Test Mulberry

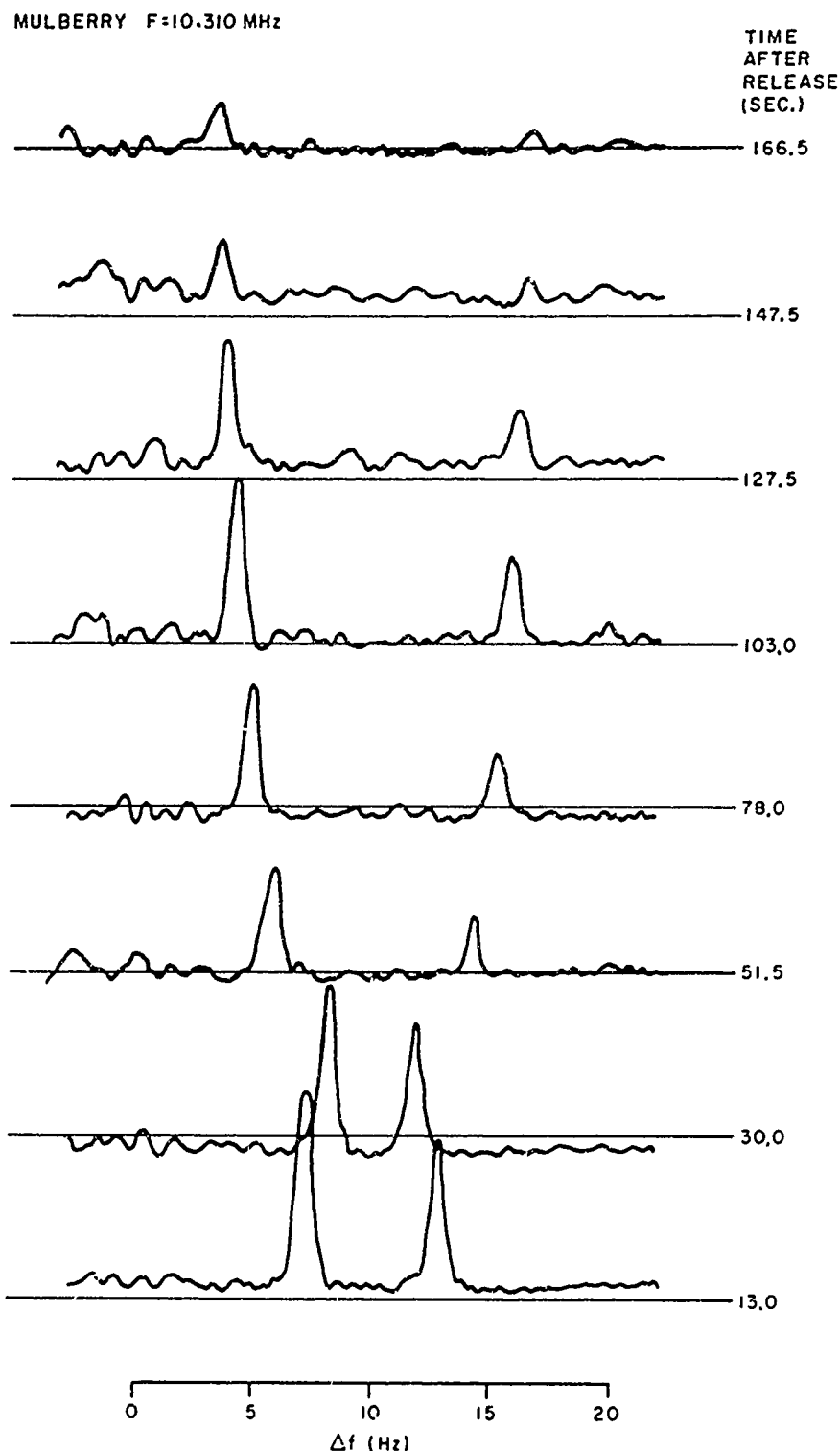


Figure 5-3 Selected Scans of the Amplitude Spectra of the Signal at $F = 10.31$ MHz for Test Mulberry. (The Folding of the Spectral Components Lying Outside the Unambiguous Doppler Window Causes Images to Appear on the Display.)

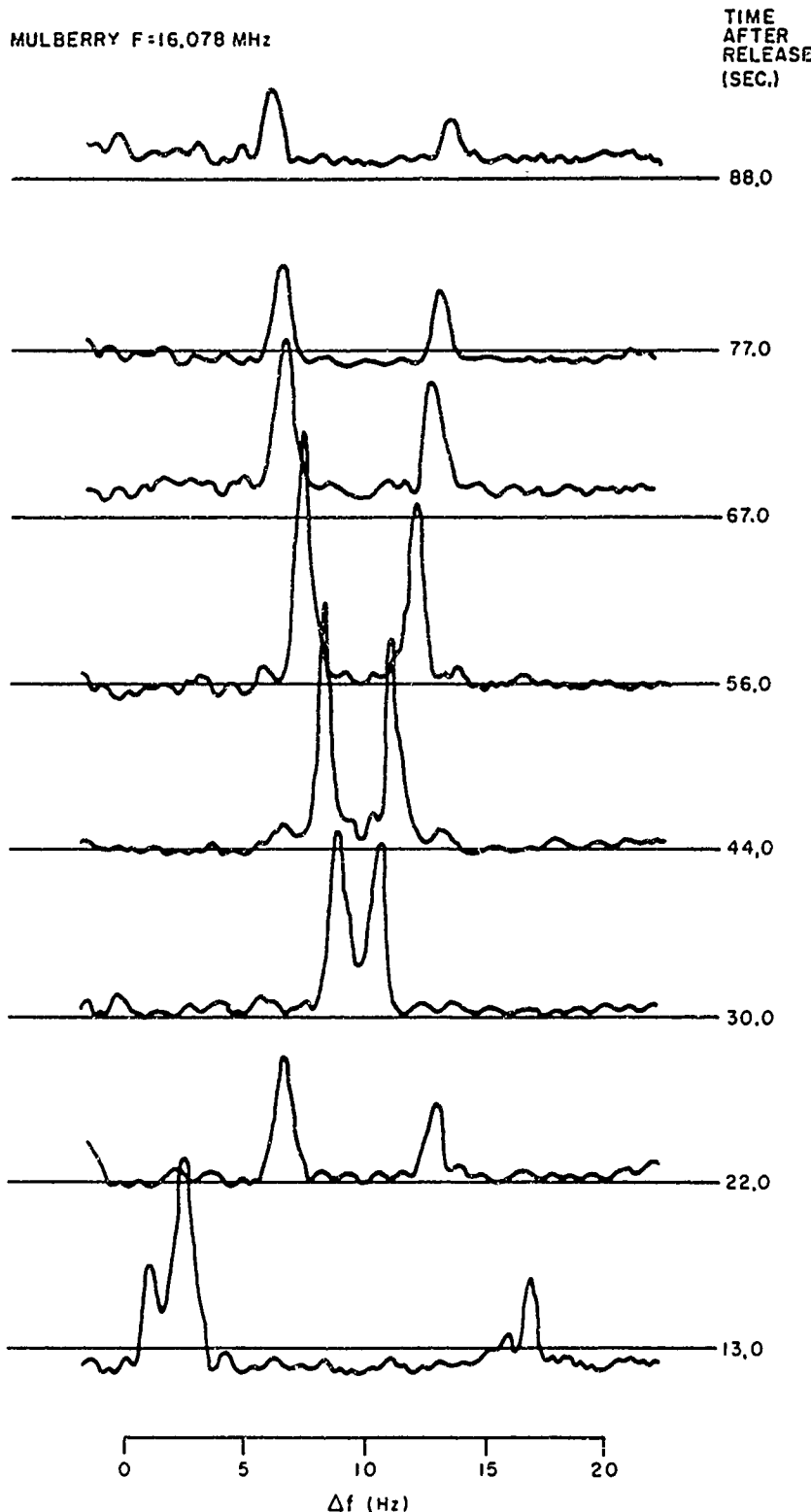


Figure 5-4 Selected Scans of the Amplitude Spectra of the Signal at $F = 16.078 \text{ MHz}$ for Test Mulberry. (The Folding of the Spectral Components Lying Outside the Unambiguous Doppler Window Causes Images to Appear on the Display.)

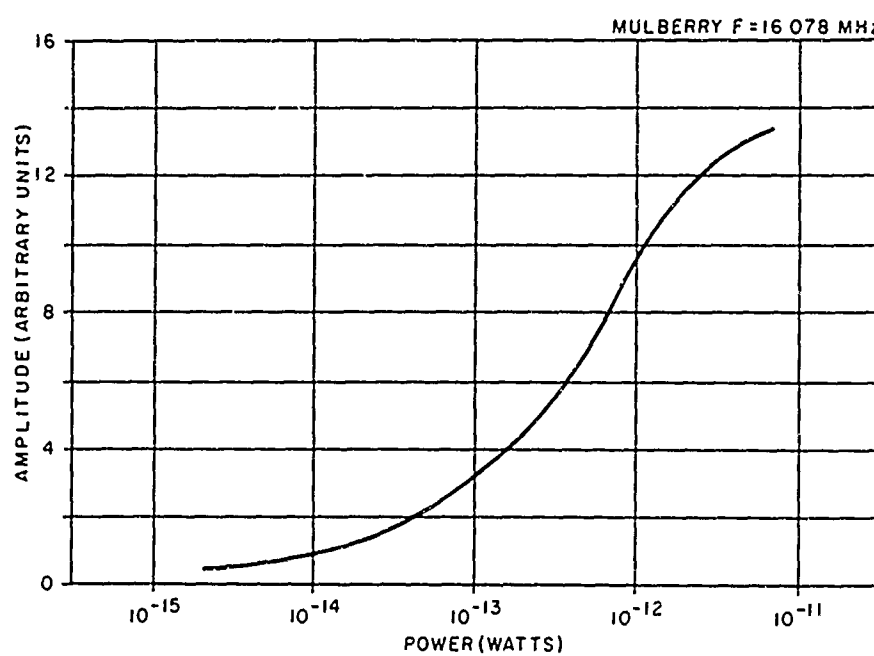
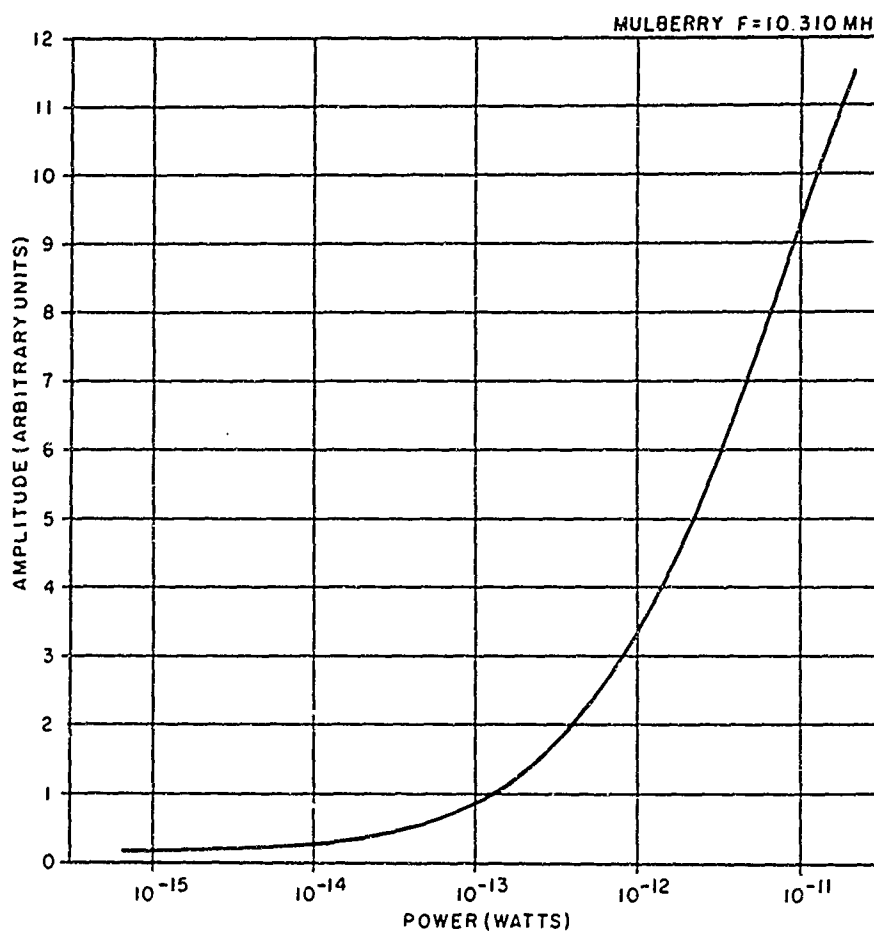


Figure 5-5 The Calibration Curves Used to Convert the Arbitrary Units of Amplitude to Absolute Signal Power

The amplitude and power plots for the two frequencies are presented in Figures 5-6 and 5-7. The dashed horizontal lines shown on the plots correspond to the average noise level and the minimum detectable signal level which is arbitrarily set at one standard deviation above the noise level. The systematic fading observed in the signal amplitude is considered as due to the interference between the ordinary and extraordinary modes of the echo. The power plots are constructed from the envelopes of the amplitude curves and hence represent the sum of the powers returned in the two modes.

5.3 RESULTS

The power measurements of the received signal are converted to the scattering cross sections of the plasma cloud using the radar equation

$$\sigma = \frac{64 \pi^3 R_1^2 R_2^2 P_r}{P_t G_t G_r \lambda^2} \quad (5-1)$$

The parameters of Equation 5-1 are the same as defined in paragraph 4.1.1. The gains G_t and G_r include the system losses and are given as $(g_t \gamma_t)$ and $(g_r \gamma_r)$ where g's and γ 's represent respectively the antenna gains and the efficiency factors. The system parameters used to calculate the scattering cross sections are listed in Table 5-1.

TABLE 5-1
SYSTEM PARAMETERS

λ (Meters)	P_t (Watts)	g_t	g_r	γ_t	γ_r
18.66	1.24×10^4	4.60	6.31	0.295	0.617
29.40	1.50×10^4	3.70	4.39	0.490	0.414

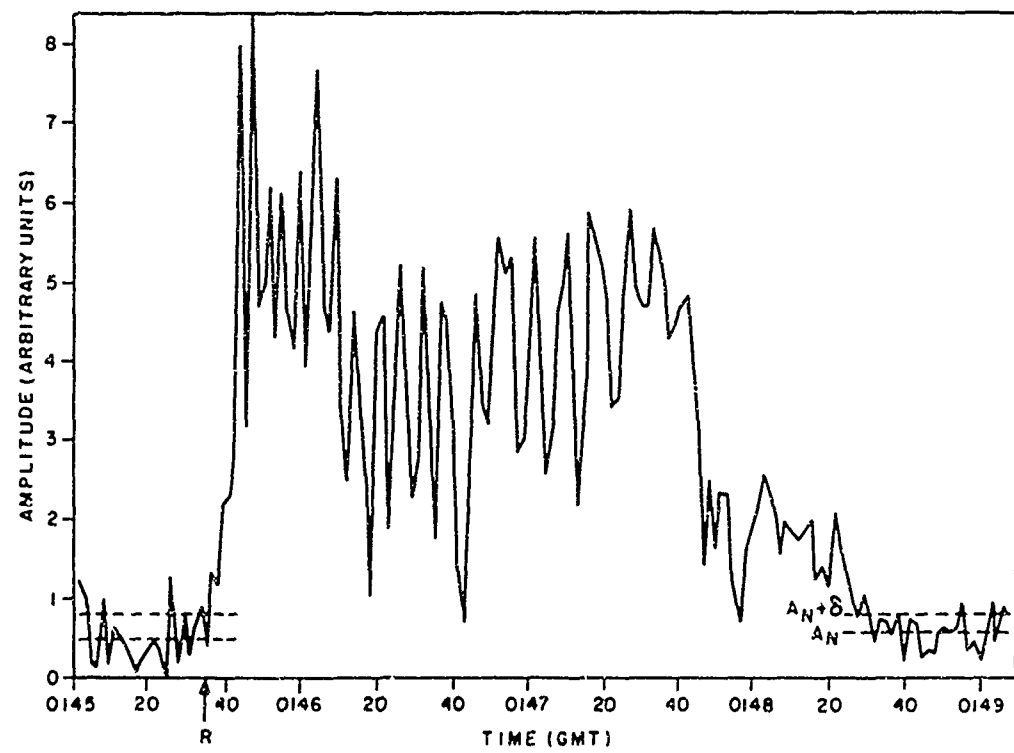
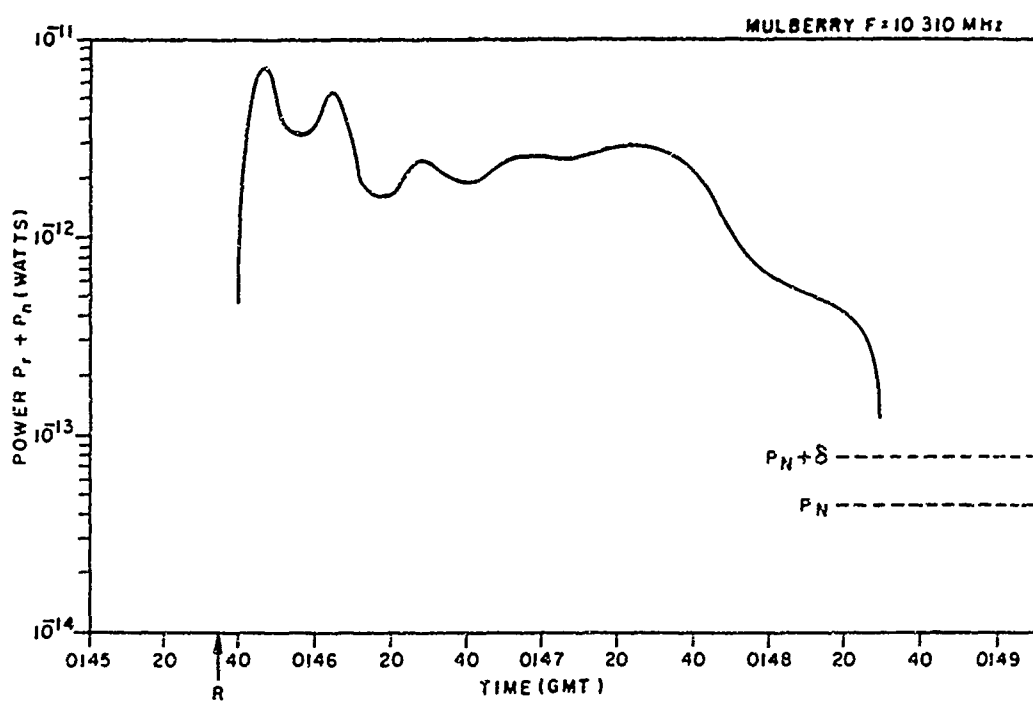


Figure 5-6 The Amplitude (Arbitrary Scale) and the Power Variations of the Signal at 10.31 MHz. The Power Curve is Constructed from the Envelope of the Amplitude Plot. The Horizontal Dashed Lines Indicate the Average Noise and the Minimum Detectable Signal Levels.

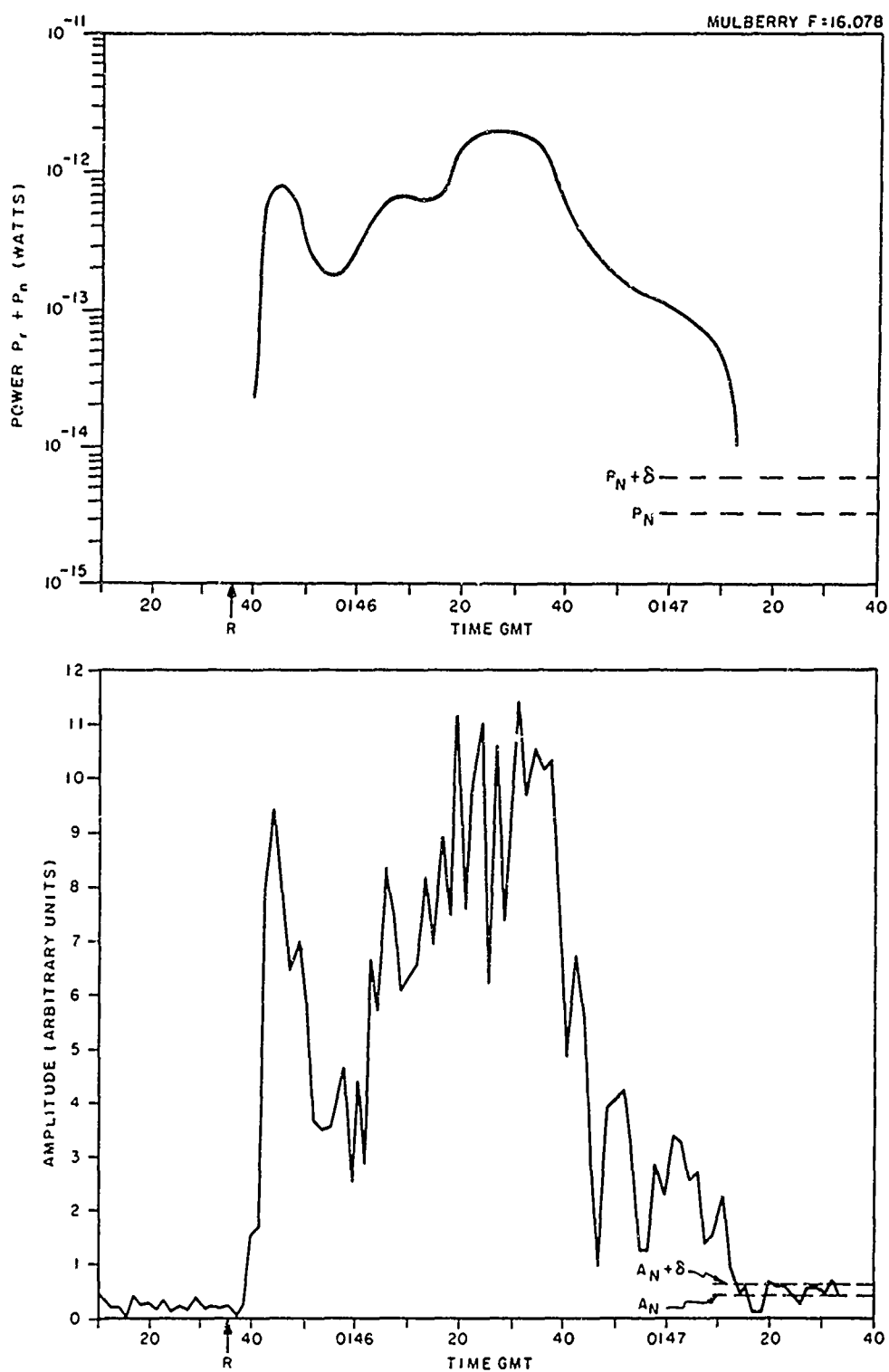


Figure 5-7 The Amplitude (Arbitrary Scale) and the Power Variations of the Signal at $F = 16.078$ MHz. The Power Curve is Constructed from the Envelope of the Amplitude Plot. The Horizontal Dashed Lines Indicate the Average Noise and the Minimum Detectable Signal Levels.

The antenna gains in the direction of the cloud for the deltas are obtained by computing the patterns for the configurations used in the experiments. An estimate of 8 dB is adopted, however, for the log periodic antenna. The efficiency factors γ_t and γ_r account for the cable and impedance mismatch losses. The ranges R_1 and R_2 to the reflection point of the cloud from the transmitter and the receiver are taken from the results of the ray tracing program. Figure 5-8 shows how the ranges vary with time as the reflection point moves out and then recedes toward the center of the cloud. The scattering cross sections, calculated on the basis of the above parameters and the power measurements of the received signals, are presented for the two frequencies in Figures 5-9 and 5-10 along with the Doppler information read out of the amplitude spectra. The minimum detectable cross section σ_{\min} is also indicated on the plots and it is about $3 \times 10^3 \text{ m}^2$ for 10.31 MHz and $4.4 \times 10^2 \text{ m}^2$ for 16.078 MHz. The initial maximum observed in the scattering cross sections on the two frequencies is believed to be due to thermal ionization that appears immediately on release. The following minimum which was reported to be more pronounced at higher frequencies is caused apparently by the decay of the thermal ionization before the photoionization builds up significantly. The maximum that is associated with the photoionization occurs at about 110 seconds for 10.31 MHz and 50 seconds for 16.078 MHz. The observed Doppler behavior is characteristic of an expanding cloud with the rate of expansion decreasing continuously with time. Further discussion of the results is deferred to the next section where they are compared with those synthesized by ray tracing through Gaussian clouds.

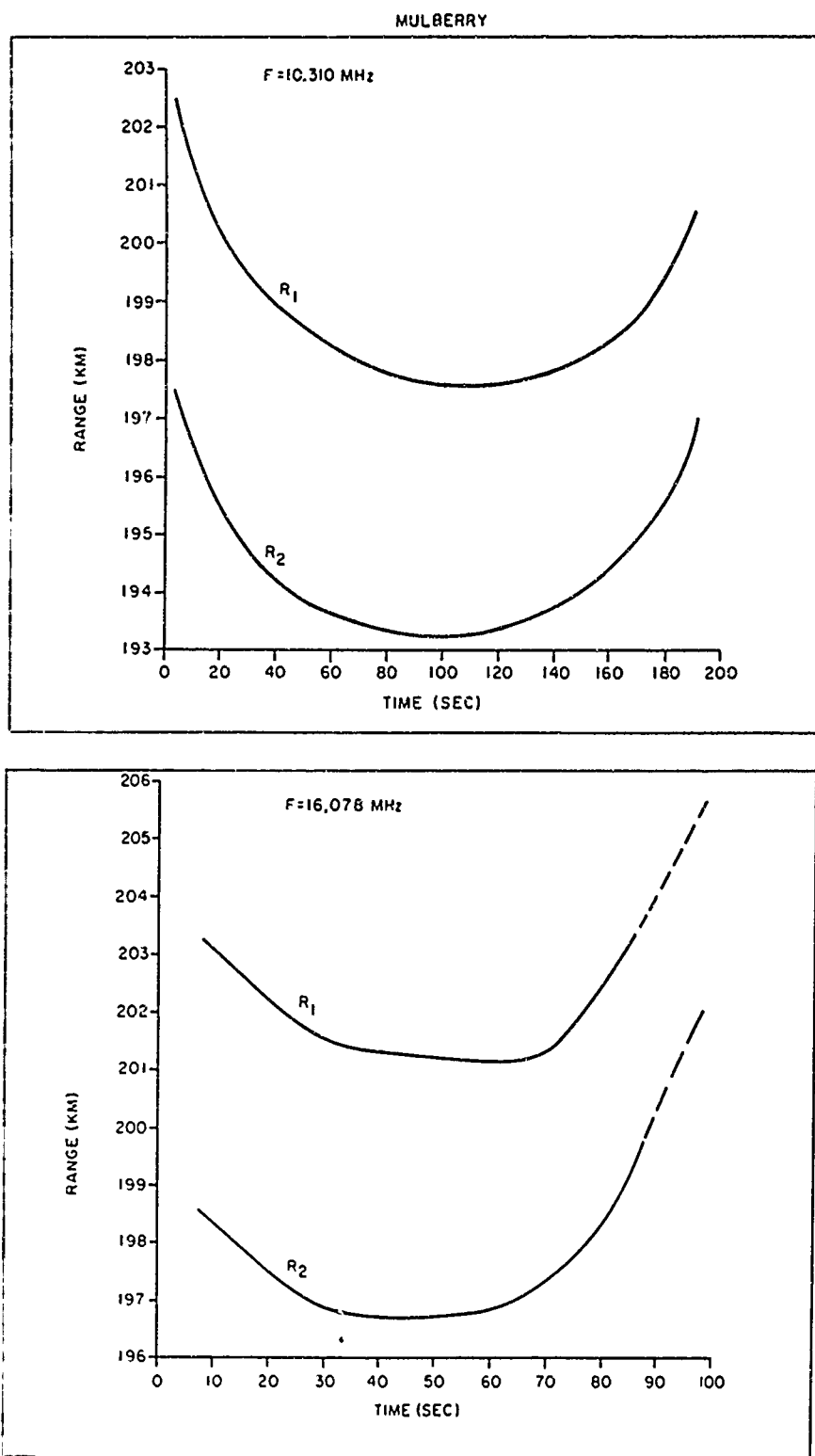


Figure 5-8 The Variation With Time Of The Ranges R_1 and R_2 To The Reflection Point Respectively From The Transmitter And Receiver

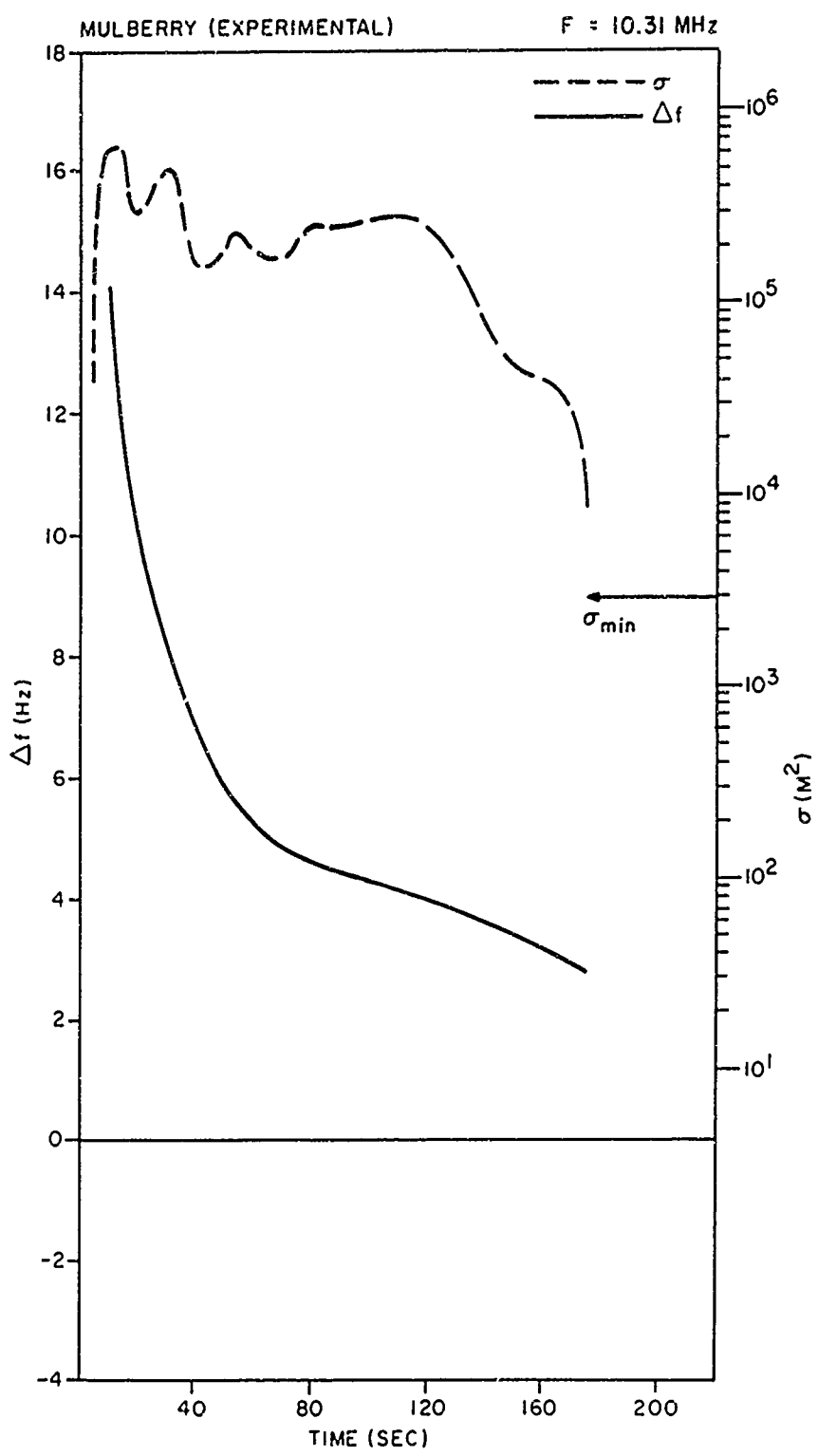


Figure 5-9 Time History of the Doppler Shift and the Scattering Cross-Section Derived from the HF Measurements at $F = 10.31 \text{ MHz}$

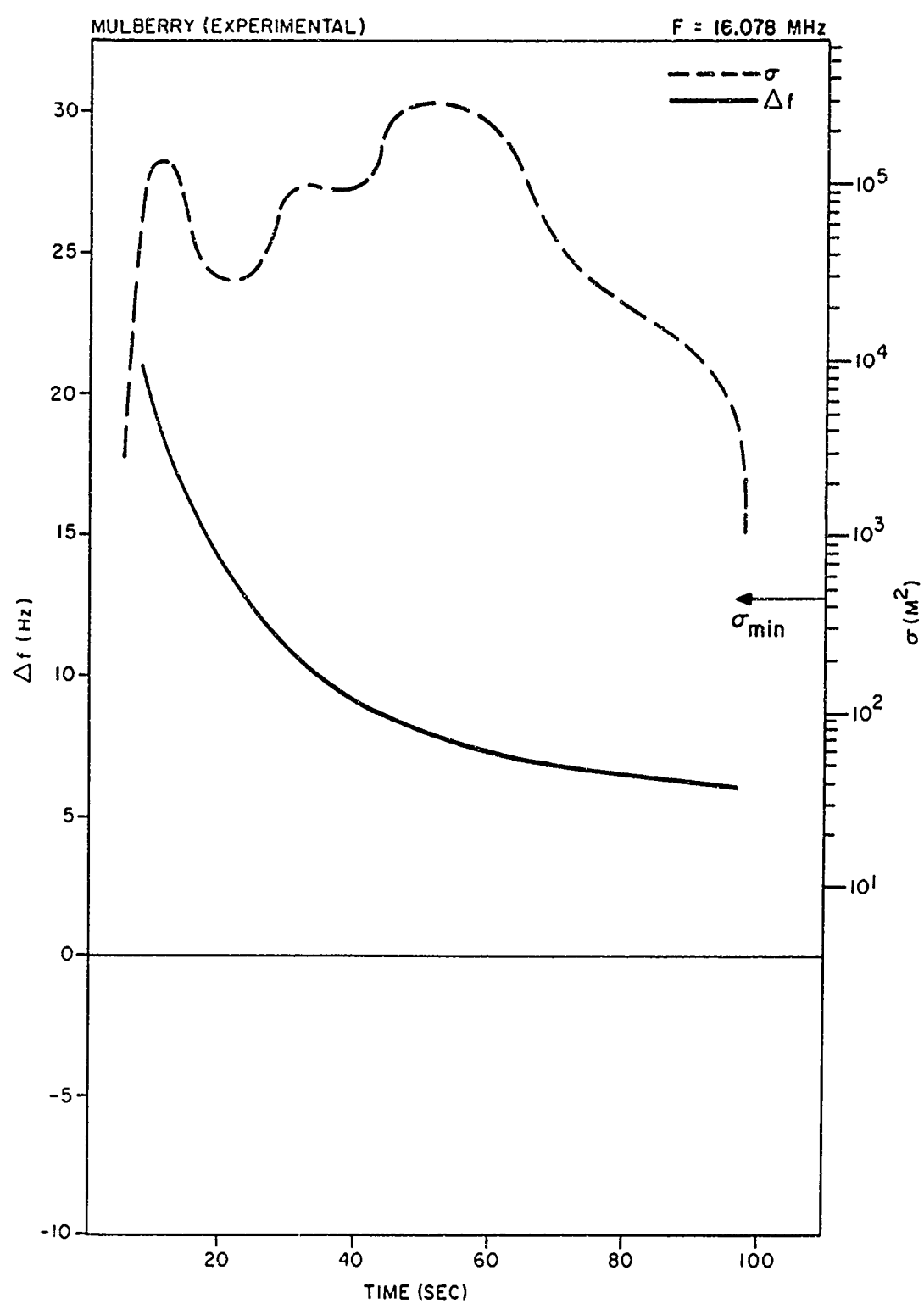


Figure 5-10 Time History of the Doppler Shift and the Scattering Cross-Section Derived from the HF Measurements at $F = 16.078 \text{ MHz}$

SECTION 6. COMPARISON BETWEEN EXPERIMENTAL AND RAY TRACING RESULTS

The time dependent Gaussian model adopted for the ray tracing, while permitted to change its origin from one time to another on the basis of the optical trajectory data, had been kept stationary at any given time as the rays were traced. Since the cloud was observed to drift continuously in position, there is a Doppler component associated with this bodily motion which should be added to that computed for the expanding stationary cloud to allow a comparison between the theory and the observations. A computer program is available which calculates the drift Doppler when the coordinates of the cloud as a function of time and the operating frequency are given. Figure 6-1 shows the drift Doppers as function of time at 10.31 and 16.078 MHz for the test Mulberry. Using these values, the computed Doppers have been

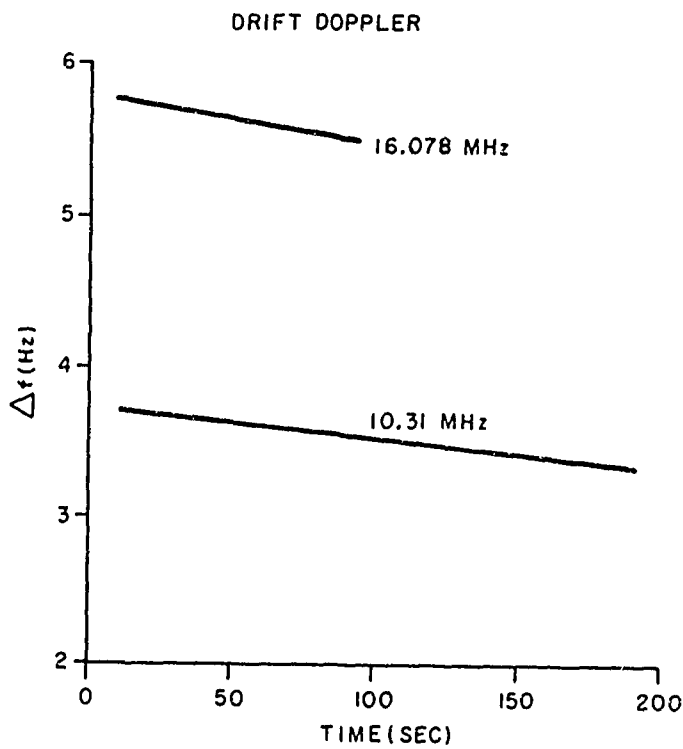


Figure 6-1 The Doppler Shift Associated With the Drift of the Plasma Cloud for $F = 10.31$ and 16.078 MHz

corrected and are presented along with the scattering cross sections and the corresponding experimental results in Figures 6-2 and 6-3. The synthesized curves of the extraordinary mode are selected for comparison since they represent the actual conditions at the time of the signal drop-out which is of maximum importance. There is an apparent discrepancy in the cutoff times indicated by the experimental and the synthesized curves. This seems to be due to the fact that the parameters, the total ion content and the diffusion coefficients, which determine the lifetime of the cloud for different operating frequencies have been kept constant in ray tracing synthesis where in fact they change with time. The discrepancy can be removed by adjusting the time scales of the synthesized curves to match with that of the experimental curves. The adjustment is not made, however, in Figures 6-2 and 6-3.

The Doppler and the scattering cross section synthesized by ray tracing are found to differ quite significantly from those measured experimentally. The differences are consistent for both the operating frequencies, 10.31 and 16.078 MHz. The most important difference in the Doppler behavior is that the synthesized Doppler based on a Gaussian model has a tail at the time of signal drop-out which is not experimentally observed. It has been speculated that the signal might be below the level of system sensitivity and could have been lost in the background noise at the time when the Doppler tail is expected to be seen. The estimated minimum detectable cross section σ_{\min} and the ray tracing results, however, clearly show that the signal level is above the system sensitivity and the doppler tail should have been observed if the distribution were truly Gaussian. Even if σ_{\min} were greater by two orders of magnitude than estimated, still the signal

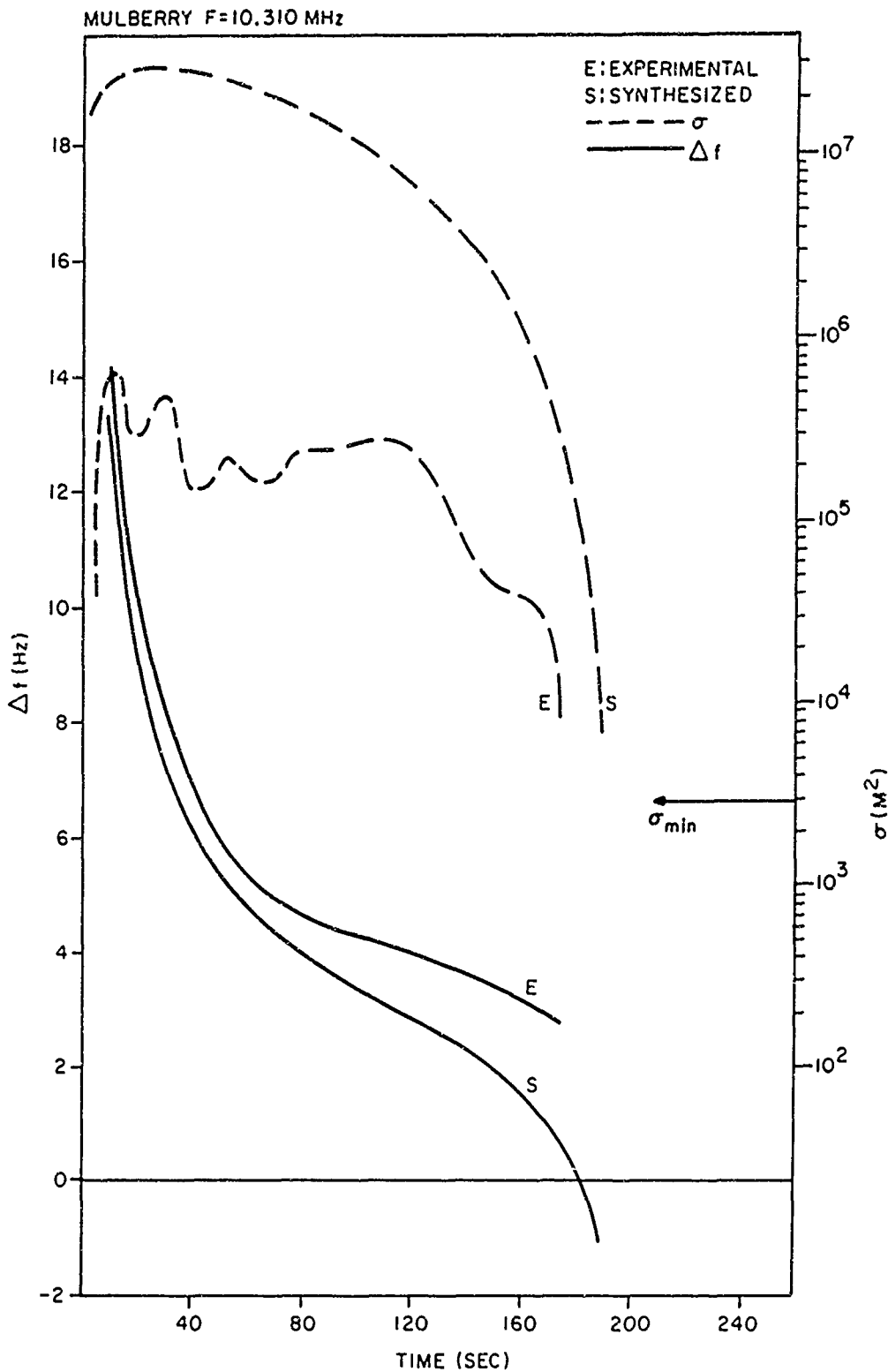


Figure 6-2 Comparison Between The Experimental And The Synthesized Time Histories Of The Doppler Shift And The Scattering Cross Section At $F = 10.31$ MHz

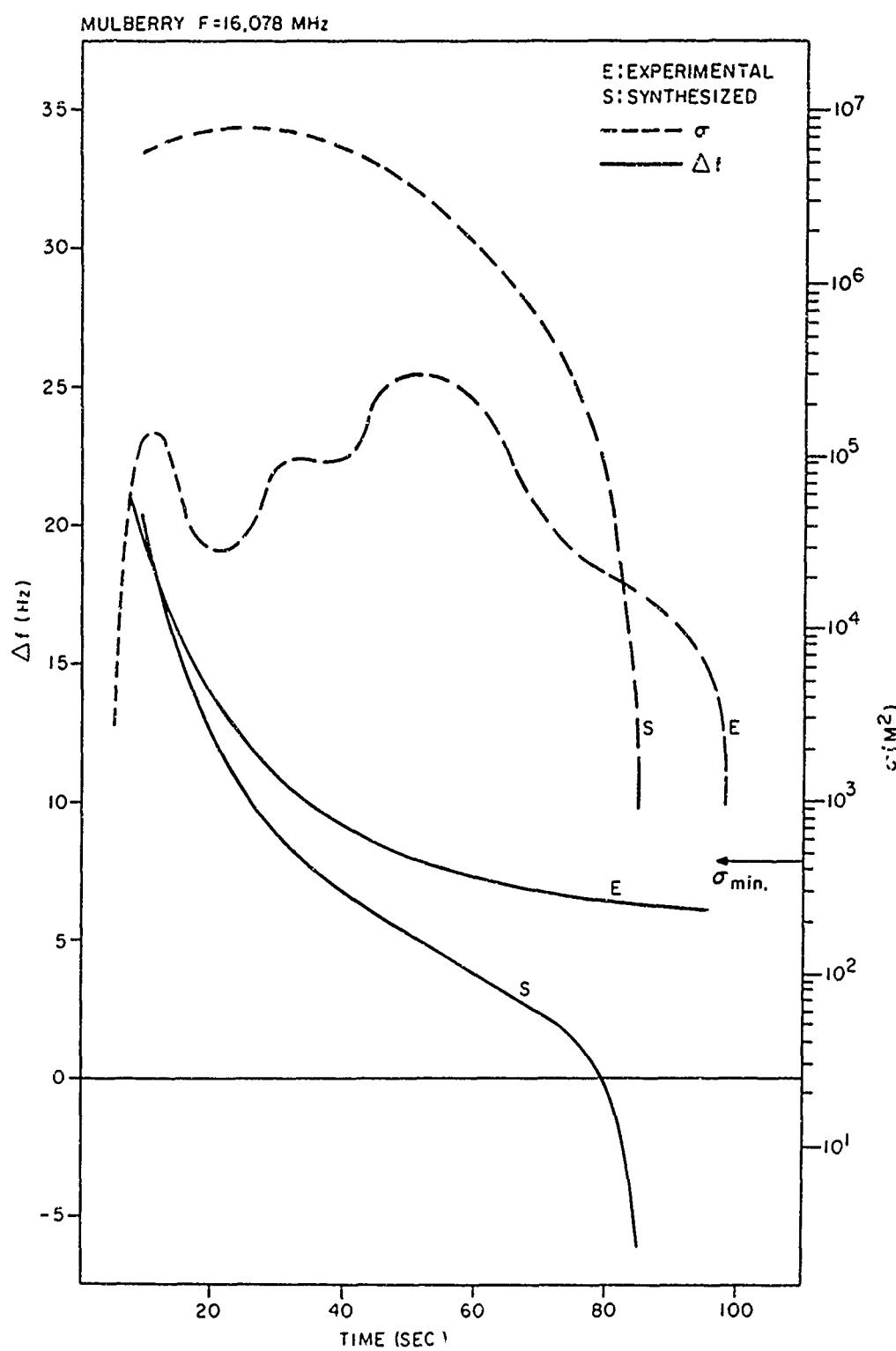


Figure 6-3 Comparison Between the Experimental And The Synthesized Time Histories Of The Doppler Shift And The Scattering Cross Section At $F = 16.078$ MHz

should be detectable over a significant portion of the Doppler tail. Since the uncertainties in the system losses are not likely to be greater than 20 dB, the ray tracing results lead to the conclusion that the electron density distribution is unlike Gaussian during the late time evolution of the cloud. Considering the general behavior, the experimental Doppler is found to be consistently greater than that synthesized. It was noted earlier from a comparison of the Doppers by hard ellipsoid and ray tracing methods that the effect of the 'softness' of the cloud is to contribute some positive Doppler. In analogy to that, the comparison between the experimental and the ray tracing Doppler suggests that the cloud is softer than that implied by the adopted Gaussian distribution. The scattering cross sections synthesized by ray tracing are 10 to 20 dB greater than those derived from the experimental data. Since the uncertainties in antenna gains and system losses are not likely to add up to this magnitude, the true cross sections of the cloud seem to be lower than that predicted by the Gaussian model. This suggests that the cloud is softer than the Gaussian causing a greater defocusing and thereby a reduction in the cross section which is consistent with the Doppler behavior. The general trend in the variation with time is such that the experimental cross sections hold up closer to the peak for longer time than the synthesized. This could happen if the expansion phase of the plasma frequency contour supporting the reflection lasts longer than that associated with the Gaussian model. The defocussing effects of the underlying ionization which build up in time are expected to offset to some extent the increase in the cross section associated with the extended phase of expansion and thus can lead to the observed slow variation. It emerges from the comparison that the true distribution of the cloud tends to become flatter in the sense that the density falls off much more gradually from the center than that in the adopted Gaussian model as the time progress towards the signal drop-out.

SECTION 7. SUMMARY AND CONCLUSIONS

A three dimensional ray tracing program has been used to synthesize hf radar signatures from Gaussian plasma clouds. The prime objective of the investigation is to test the validity of the assumed Gaussian model by comparing the synthesized signatures with the experimental observations. The ray tracing results have been compared also to that computed for the case of a hard expanding ellipsoid model to study the effects of the ionization lying below the level of reflection.

The 3D ray tracing program used in this study has been developed at ESSA by Dr. R.M. Jones and is based on a set of six partial differential equations similar to that of Haselgrave (1954). The program can take the electron collisions and the Earth's magnetic field into account and trace ray paths for both ordinary and extraordinary modes.

The Gaussian distribution of electron (ion) density in the plasma cloud used for synthesizing the radar signatures is based on the ambipolar diffusion model given by Holway (1965). The Gaussian parameters adopted for the synthesis are that appropriate to the test Mulberry of Pre-SECEDE series conducted at White Sands, New Mexico (Minkoff, 1970).

The ray tracing method of synthesizing a radar signature from the cloud involves first the determination of the 'homing' ray when the transmitter-cloud-receiver configuration is given. The Doppler shift of interest is the one associated with this ray and it is recorded. The next step is to evaluate the scattering cross section of the cloud which has been done by following the technique described by Croft (1967) and Georges and Stephenson (1969). It involves transmission of a narrow bundle of rays and the determination of the area

of their impact on the ground. The radar signature synthesis by the hard ellipsoid method involves the determination of the specular point from the radar. A method to find the specular point on the cloud and to evaluate the Doppler shift and the scattering cross section has been described.

The experimental data for which the ray tracing simulation has been made was collected by operating hf phase path sounders at 10.31 and 16.078 MHz during test Mulberry of Pre-SECEDE series. The data has been reduced to the form of power spectra to measure the Doppler shifts and to estimate the radar scattering cross sections of the cloud.

The following conclusions can be drawn from the foregoing study of the synthesized and the observed radar signatures from the plasma clouds:

The radar signatures synthesized by ray tracing for the Gaussian plasma clouds are found to be significantly different from those observed experimentally. The synthesized Doppler shifts are somewhat lower and reveal a negative tail in contrast to the observed Doppler behavior. The scattering cross sections, however, are 10 to 20 dB greater than those derived from the observations. These differences tend to suggest that the electron density variation outward from the center of the cloud is more gradual than that in the adopted Gaussian model.

The comparison between the signatures synthesized by the ray tracing and the hard ellipsoid model shows that the effect of the ionization below the reflection level is to introduce a significant positive shift in Doppler and a considerable reduction in the scattering cross section by way of defocusing. The factor by which the scattering cross section is reduced is found to vary from about 3 at the time

cf Peak cross section to 30 just prior to the signal dropout. It is, therefore, concluded that a simple hard ellipsoid model is inadequate for a satisfactory synthesis of hf radar signatures.

APPENDIX A. GAUSS X ROUTINE AND SAMPLE RAY TRACE

The subroutine Gauss X listed here calculated the Appleton Parameter X ($= f_n^2/f^2$) and its time and spatial derivatives in geomagnetic dipole coordinate system. The table that follows the routine shows the sample printout of the ray tracing program. The results are for the homing extraordinary ray at the operating frequency of 10.31 MHz and at the time 180 seconds after the release of the cloud. Figure A-1 shows the corresponding ray plot in the vertical plane defined by the line joining the transmitter and the receiver. The portion of the ray path within the cloud where there is significant bending is shown alongside on an enlarged scale.

```

1  SUBROUTINE GAUSSX
2  DATA PI/3.14159265/
3  REAL NO,K,I,N,D(15),NLO,NLN
4  COMMON R(6)/WW/1D(14),DUM,W(400)/XX/X,PXPR(3),PXPT
5  EQUIVALENCE (F,W(3)),(PHN,W(13)),(THN,W(15)),(RE,W(19)),(NO,W(20))
6  I,(T,W(202)),(TAU,W(203)),(HO,W(204)),(DR,W(205)),(DL,W(206)),
7  2(K,W(207)),(THO,W(208)),(PHO,W(209)),(I,W(210)),(H,W(211))
8  ENTRY ELECTX
9  IF(W(301).GT.0.) GO TO 1
10 W(301)=1.
11 RCOSQ=HO**2+4.*DR*T
12 ZCO=SQRT(HO**2+4.*DZ*T)
13 CTHMO=SIN(THO)*SIN(THN)+COS(THO)*COS(THN)*COS(PHO-PHN)
14 STHMO=SQRT(1.00-CTHMO**2)
15 SPHMO=COS(THO)*SIN(PHO-PHN)/STHMO
16 CPHMO=SQRT(1.00-SPHMO**2)
17 XMO=(RE+H)*STHMO*CPHMO
18 YMO=(RE+H)*STHMO*SPHMO
19 ZMO=(RE+H)*CTHMO
20 CHIMO=PI/2.-I+ACOS(CTHMO)
21 CCHIMO=COS(CHIMO)
22 SCHIMO=SIN(CHIMO)
23 CPCX=CPHMO*CCHIMO
24 SPCX=SPHMO*CCHIMO
25 CPSX=CPHMO*SCHIMO

```

```

26 SPSX=SPHMO*SCHIMO
27 FT=(1.-EXP(-T/TAU))/IZC0*RCOSQ)
28 DFDT=1./ (TAU+ZC0*RCOSQ )-FT*(1./TAU+4.*DR/RCOSQ+2.*DZ/ZC0**2)
29 CONSTK=F9.02
30 CNST1=NO/P1**1.5
31 CNST2=CONST*CNST1
32 CR2=COS(R(2))
33 SR2=SIN(R(2))
34 CR3=COS(R(3))
35 SR3=SIN(R(3))
36 XM=R(1)*SR2*CR3
37 YM=R(1)*SR2*SR3
38 ZM=R(1)*CR2
39 XC=CPCX*(XM-XMO)+SPCX*(YM-YMO)-SCHIMO*(ZM-ZMO)
40 YC=-SPHMO*(XM-XMO)+CPHMO*(YM-YMO)
41 ZC=CPSX*(XM-XMO)+SPSX*(YM-YMO)+CCHIMO*(ZM-ZMO)
42 GT=EXPI-(XC**2+YC**2)/RCOSQ)
43 HT=EXP(-(ZC/ZC0)**2)
44 N=CNST1*FT*GT*HT
45 X=CONST*N
46 D(10)=-N*2.*XC/RCOSQ
47 D(11)=-N*2.*YC/RCOSQ
48 D(12)=-N*2.*ZC/ZC0**2
49 D(13)=CPCX*D(10)-SPHMO*D(11)+CPHX*D(12)
50 D(14)=SPCX*D(10)+CPHMO*D(11)+SPSX*D(12)
51 D(15)=-SCHIMO*D(10)+CCHIMO*D(12)
52 D(1)=SR2*CR3
53 D(2)=R(1)*CR2*CR3
54 D(3)=R(1)*SR2*SR3
55 D(4)=SR2*SR3
56 D(5)=R(1)*CR2*SR3
57 D(6)=R(1)*SR2*CR3
58 D(7)=CR2
59 D(8)=R(1)*SR2
60 C D(9)=0.
61 PXPR(1)=CONST*(D(13)*D(1)+D(14)*D(4)+D(15)*D(7))
62 PXPR(2)=CONST*(D(13)*D(2)+D(14)*D(5)+D(15)*D(8))
63 PXPR(3)=CONST*(D(13)*D(3)+D(14)*D(6))
64 D(2)=GT*4.*DR*((XC**2+YC**2)/RCOSQ**2)
65 D(3)=HT*4.*DZ*(ZC/ZC0**2)**2
66 PXPT=CNST2*(GT*HT*DFDT+FT*HT*D(2)+FT*GT*D(3))
67 RETURN
68 END

```

EXPLANATION											
ELEVATION-ANGLE OF TRANSMISSION = -75°29'782° DEG						ELEVATION-ANGLE OF TRANSMISSION = 306°87'600 DEG					
X EXTRAORDINARY						NO COLLISIONS					
HEIGHT	RANGE	DEVIATION	XTR LOCAL	COPLEX	GROUP	PATH	PHASE	PATH	ABSORPTION	DOPPLER	C.S.
KM	KM	DEG	DEG	DEG	DEG	KM	KM	KM	KM	KM	KM
0.0	km	-0.000	-0.000	-0.000	-0.000	75.297	75.667	0.0	-1.03	166.036	166.036
-0.01	km	1.00	71.3m	1.1247	-0.000	75.297	75.667	0.0	-1.03	167.7635	167.7635
-0.02	km	1.02	40.939	1.1291	-0.000	75.297	75.671	0.0	-1.03	168.7636	168.7636
-0.03	km	1.05	3.778	1.1364	-0.000	75.297	75.673	0.0	-1.03	169.7636	169.7636
-0.04	km	1.08	3.467	1.1426	-0.000	75.297	75.675	0.0	-1.03	170.7636	170.7636
-0.05	km	1.10	3.126	1.1485	-0.000	75.297	75.677	0.0	-1.03	171.7636	171.7636
-0.06	km	1.12	2.845	1.1543	-0.000	75.297	75.679	0.0	-1.03	172.7636	172.7636
-0.07	km	1.15	2.525	1.1610	-0.000	75.297	75.680	0.0	-1.03	173.7636	173.7636
-0.08	km	1.18	2.205	1.1673	-0.000	75.297	75.681	0.0	-1.03	174.7636	174.7636
-0.09	km	1.20	1.873	1.1736	-0.000	75.297	75.682	0.0	-1.03	175.7636	175.7636
-0.10	km	1.23	1.543	1.1794	-0.000	75.297	75.683	0.0	-1.03	176.7636	176.7636
-0.11	km	1.25	1.213	1.1857	-0.000	75.297	75.684	0.0	-1.03	177.7636	177.7636
-0.12	km	1.27	0.882	1.1919	-0.000	75.297	75.685	0.0	-1.03	178.7636	178.7636
-0.13	km	1.30	0.552	1.1981	-0.000	75.297	75.686	0.0	-1.03	179.7636	179.7636
-0.14	km	1.32	0.221	1.2043	-0.000	75.297	75.687	0.0	-1.03	180.7636	180.7636
-0.15	km	1.35	-0.101	1.2105	-0.000	75.297	75.688	0.0	-1.03	181.7636	181.7636
-0.16	km	1.37	-0.431	1.2167	-0.000	75.297	75.689	0.0	-1.03	182.7636	182.7636
-0.17	km	1.40	-1.101	1.2229	-0.000	75.297	75.690	0.0	-1.03	183.7636	183.7636
-0.18	km	1.42	-1.771	1.2291	-0.000	75.297	75.691	0.0	-1.03	184.7636	184.7636
-0.19	km	1.45	-2.440	1.2353	-0.000	75.297	75.692	0.0	-1.03	185.7636	185.7636
-0.20	km	1.48	-3.110	1.2415	-0.000	75.297	75.693	0.0	-1.03	186.7636	186.7636
-0.21	km	1.50	-3.780	1.2476	-0.000	75.297	75.694	0.0	-1.03	187.7636	187.7636
-0.22	km	1.52	-4.449	1.2538	-0.000	75.297	75.695	0.0	-1.03	188.7636	188.7636
-0.23	km	1.55	-5.119	1.2599	-0.000	75.297	75.696	0.0	-1.03	189.7636	189.7636
-0.24	km	1.57	-5.789	1.2661	-0.000	75.297	75.697	0.0	-1.03	190.7636	190.7636
-0.25	km	1.60	-6.459	1.2723	-0.000	75.297	75.698	0.0	-1.03	191.7636	191.7636
-0.26	km	1.62	-7.128	1.2785	-0.000	75.297	75.699	0.0	-1.03	192.7636	192.7636
-0.27	km	1.65	-7.797	1.2847	-0.000	75.297	75.700	0.0	-1.03	193.7636	193.7636
-0.28	km	1.67	-8.467	1.2909	-0.000	75.297	75.701	0.0	-1.03	194.7636	194.7636
-0.29	km	1.70	-9.136	1.2971	-0.000	75.297	75.702	0.0	-1.03	195.7636	195.7636
-0.30	km	1.72	-9.806	1.3033	-0.000	75.297	75.703	0.0	-1.03	196.7636	196.7636
-0.31	km	1.75	-10.475	1.3095	-0.000	75.297	75.704	0.0	-1.03	197.7636	197.7636
-0.32	km	1.77	-11.145	1.3157	-0.000	75.297	75.705	0.0	-1.03	198.7636	198.7636
-0.33	km	1.80	-11.814	1.3219	-0.000	75.297	75.706	0.0	-1.03	199.7636	199.7636
-0.34	km	1.82	-12.484	1.3281	-0.000	75.297	75.707	0.0	-1.03	200.7636	200.7636
-0.35	km	1.85	-13.153	1.3343	-0.000	75.297	75.708	0.0	-1.03	201.7636	201.7636
-0.36	km	1.87	-13.822	1.3405	-0.000	75.297	75.709	0.0	-1.03	202.7636	202.7636
-0.37	km	1.90	-14.491	1.3467	-0.000	75.297	75.710	0.0	-1.03	203.7636	203.7636
-0.38	km	1.92	-15.160	1.3529	-0.000	75.297	75.711	0.0	-1.03	204.7636	204.7636
-0.39	km	1.95	-15.829	1.3591	-0.000	75.297	75.712	0.0	-1.03	205.7636	205.7636
-0.40	km	1.97	-16.499	1.3653	-0.000	75.297	75.713	0.0	-1.03	206.7636	206.7636
-0.41	km	2.00	-17.168	1.3715	-0.000	75.297	75.714	0.0	-1.03	207.7636	207.7636
-0.42	km	2.02	-17.837	1.3777	-0.000	75.297	75.715	0.0	-1.03	208.7636	208.7636
-0.43	km	2.05	-18.506	1.3839	-0.000	75.297	75.716	0.0	-1.03	209.7636	209.7636
-0.44	km	2.07	-19.175	1.3891	-0.000	75.297	75.717	0.0	-1.03	210.7636	210.7636
-0.45	km	2.10	-19.844	1.3953	-0.000	75.297	75.718	0.0	-1.03	211.7636	211.7636
-0.46	km	2.12	-20.513	1.4015	-0.000	75.297	75.719	0.0	-1.03	212.7636	212.7636
-0.47	km	2.15	-21.182	1.4077	-0.000	75.297	75.720	0.0	-1.03	213.7636	213.7636
-0.48	km	2.17	-21.851	1.4139	-0.000	75.297	75.721	0.0	-1.03	214.7636	214.7636
-0.49	km	2.20	-22.520	1.4201	-0.000	75.297	75.722	0.0	-1.03	215.7636	215.7636
-0.50	km	2.22	-23.189	1.4263	-0.000	75.297	75.723	0.0	-1.03	216.7636	216.7636
-0.51	km	2.25	-23.858	1.4325	-0.000	75.297	75.724	0.0	-1.03	217.7636	217.7636
-0.52	km	2.27	-24.527	1.4387	-0.000	75.297	75.725	0.0	-1.03	218.7636	218.7636
-0.53	km	2.30	-25.196	1.4449	-0.000	75.297	75.726	0.0	-1.03	219.7636	219.7636
-0.54	km	2.32	-25.865	1.4511	-0.000	75.297	75.727	0.0	-1.03	220.7636	220.7636
-0.55	km	2.35	-26.534	1.4573	-0.000	75.297	75.728	0.0	-1.03	221.7636	221.7636
-0.56	km	2.37	-27.203	1.4635	-0.000	75.297	75.729	0.0	-1.03	222.7636	222.7636
-0.57	km	2.40	-27.872	1.4697	-0.000	75.297	75.730	0.0	-1.03	223.7636	223.7636
-0.58	km	2.42	-28.541	1.4759	-0.000	75.297	75.731	0.0	-1.03	224.7636	224.7636
-0.59	km	2.45	-29.210	1.4821	-0.000	75.297	75.732	0.0	-1.03	225.7636	225.7636
-0.60	km	2.47	-29.879	1.4883	-0.000	75.297	75.733	0.0	-1.03	226.7636	226.7636
-0.61	km	2.50	-30.548	1.4945	-0.000	75.297	75.734	0.0	-1.03	227.7636	227.7636
-0.62	km	2.52	-31.217	1.5007	-0.000	75.297	75.735	0.0	-1.03	228.7636	228.7636
-0.63	km	2.55	-31.886	1.5069	-0.000	75.297	75.736	0.0	-1.03	229.7636	229.7636
-0.64	km	2.57	-32.555	1.5131	-0.000	75.297	75.737	0.0	-1.03	230.7636	230.7636
-0.65	km	2.60	-33.224	1.5193	-0.000	75.297	75.738	0.0	-1.03	231.7636	231.7636
-0.66	km	2.62	-33.893	1.5255	-0.000	75.297	75.739	0.0	-1.03	232.7636	232.7636
-0.67	km	2.65	-34.562	1.5317	-0.000	75.297	75.740	0.0	-1.03	233.7636	233.7636
-0.68	km	2.67	-35.231	1.5379	-0.000	75.297	75.741	0.0	-1.03	234.7636	234.7636
-0.69	km	2.70	-35.899	1.5441	-0.000	75.297	75.742	0.0	-1.03	235.7636	235.7636
-0.70	km	2.72	-36.568	1.5503	-0.000	75.297	75.743	0.0	-1.03	236.7636	236.7636
-0.71	km	2.75	-37.237	1.5565	-0.000	75.297	75.744	0.0	-1.03	237.7636	237.7636
-0.72	km	2.77	-37.906	1.5627	-0.000	75.297	75.745	0.0	-1.03	238.7636	238.7636
-0.73	km	2.80	-38.575	1.5689	-0.000	75.297	75.746	0.0	-1.03	239.7636	239.7636
-0.74	km	2.82	-39.244	1.5751	-0.000	75.297	75.747	0.0	-1.03	240.7636	240.7636
-0.75	km	2.85	-39.913	1.5813	-0.000	75.297	75.748	0.0	-1.03	241.7636	241.7636
-0.76	km	2.87	-40.582	1.5875	-0.000	75.297	75.749	0.0	-1.03	242.7636	242.7636
-0.77	km	2.90	-41.251	1.5937	-0.000	75					

MULBERRY.T=180.F=10.310
F = 10.31 XTRAORDINARY

10.00 KM BETWEEN TICK MARKS

2.00 KM BETWEEN TICK MARKS

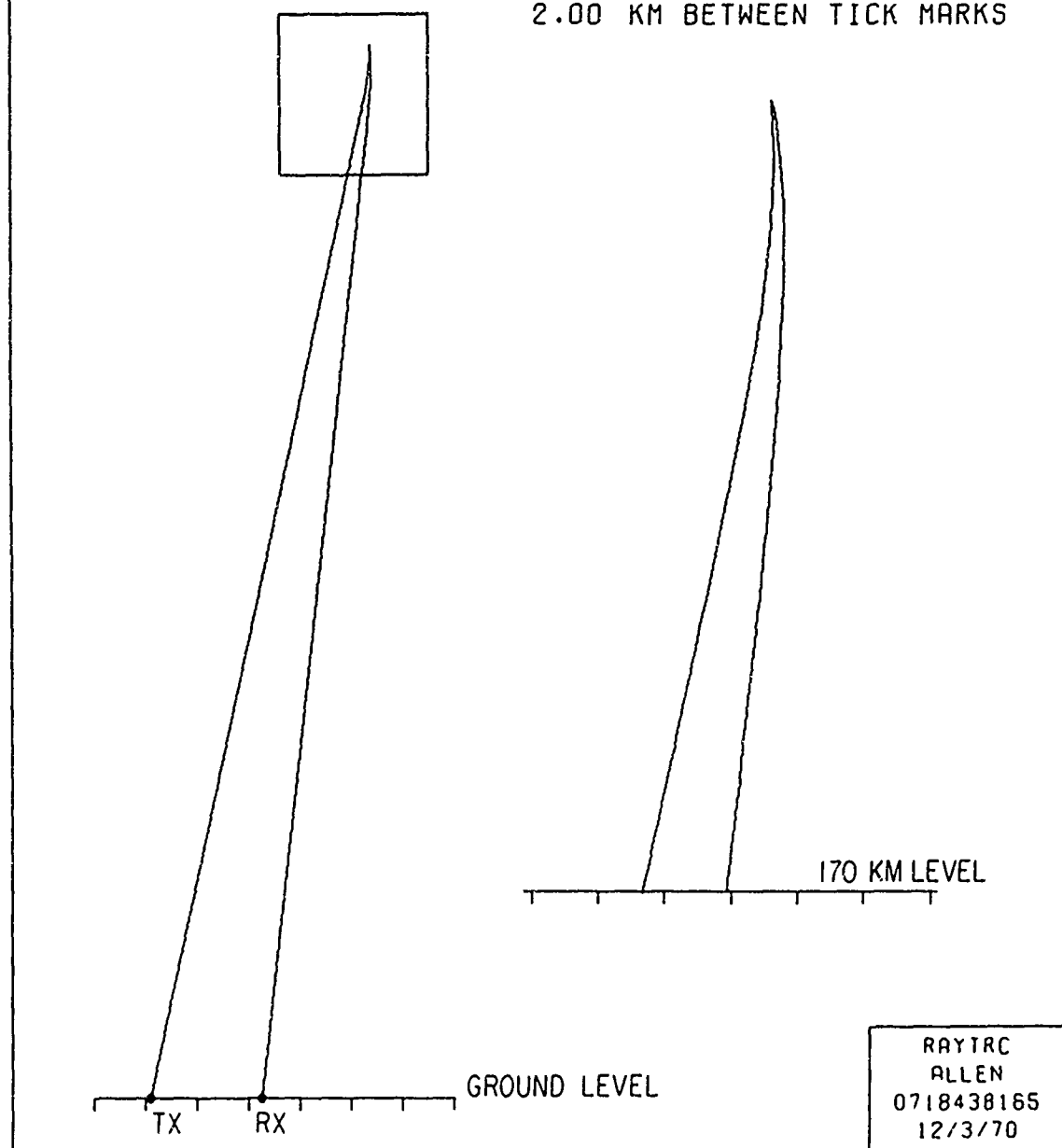


Figure A-1 A Sample Ray Trace Projection Plot In A Vertical Plane Defined By The Line Joining The Transmitter And The Receiver. The Boxed Segment Where The Ray Suffers Significant Bending Is Shown On An Enlarged Scale

APPENDIX B. A VECTOR METHOD TO CALCULATE CLOUD TRAJECTORY

The vector method described below determines the coordinates of the cloud using the line of sight data given in azimuth and elevation angles from a pair of observing stations. The cloud position is defined ideally by the intersection point of the lines of sight from the two sites. In practice, however, slight errors in sighting cause the two lines to miss each other and in this case the midpoint of the common perpendicular to the two lines of sight is taken to be the best estimate for the cloud position.

Let \vec{I} and \vec{J} be the unit vectors along the two lines of sight and \vec{N} be the unit vector along the common perpendicular to the two lines such that

$$\vec{N} = \frac{\vec{I} \times \vec{J}}{|\vec{I} \times \vec{J}|} \quad (B-1)$$

\vec{R}_1 and \vec{R}_2 represent the vectors to the two observing sites from the center of the earth; \vec{X} denote the vector to the cloud center. B_1 and B_2 are the scalar distances from the two sites to the points joined by the common perpendicular. D is the distance between the two lines along the perpendicular. Then from the geometry shown in Figure B-1 we have:

$$\vec{R}_1 + B_1 \vec{I} + \frac{D}{2} \vec{N} = \vec{X} \quad (B-2)$$

$$\vec{R}_2 + B_2 \vec{J} - \frac{D}{2} \vec{N} = \vec{X} \quad (B-3)$$

Taking the scalar product of Equations B-2 and B-3 with \vec{N} and subtracting one from the other would result in the relation

$$(\vec{R}_1 - \vec{R}_2) \cdot (\vec{N}) = D \quad (B-4)$$

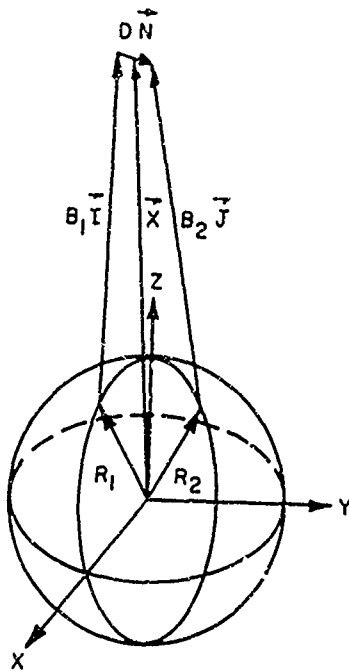


Figure B-1 Geometry for the Vector Determination of the Cloud Coordinates

It is required now to evaluate either B_1 or B_2 to obtain the position vector \vec{X} of the cloud. This can be done, for example, by vector multiplication of Equations B-2 and B-3 with the unit vector \vec{I} which yields the following expression for B_2 on making use of Equation B-1.

$$B_2 \left| \vec{I} \times \vec{J} \right| \vec{N} = \vec{I} \times \left[\vec{R}_1 - \vec{R}_2 \right] - D \left[\vec{N} \times \vec{I} \right] \quad (B-5)$$

Using Equations B-4 and B-5, the vector \vec{X} can be expressed in terms of \vec{I} , \vec{J} , \vec{N} , \vec{R}_1 and \vec{R}_2 which can be evaluated from the known quantities, the coordinates of the observing sites and the look angles to the cloud, as follows:

Let (θ_1, ϕ_1) and (θ_2, ϕ_2) be the co-latitude and east longitude of the two stations in the geographic co-ordinate system. The azimuth and elevation angles to the cloud from the two stations are

denoted as (α_1, β_1) and (α_2, β_2) , respectively. Define two Cartesian coordinate systems, (x, y, z) an Earth centered system and (x_1, y_1, z_1) with its origin at one of the observing stations (say site 1) as shown in Figure B-2. (x, y, z) is such that z is pointed toward north and (x, z) defines the reference meridian plane. (x_1, y_1, z_1) is tilted with respect to (x, y, z) by ϕ_1 in longitude and $(90 - \theta_1)$ in latitude. $(\hat{i}, \hat{j}, \hat{k})$ and $(\hat{i}_1, \hat{j}_1, \hat{k}_1)$ are the unit vectors along (x, y, z) and (x_1, y_1, z_1) , respectively. They are related by a transformation matrix as:

$$\begin{bmatrix} \hat{i}_1 \\ \hat{j}_1 \\ \hat{k}_1 \end{bmatrix} = \begin{bmatrix} \sin \theta_1 & \cos \phi_1 & \sin \theta_1 & \sin \phi_1 & \cos \theta_1 \\ -\sin \phi_1 & & \cos \phi_1 & & 0 \\ -\cos \theta_1 & \cos \phi_1 & -\cos \theta_1 & \sin \phi_1 & \sin \theta_1 \end{bmatrix} \begin{bmatrix} \hat{i} \\ \hat{j} \\ \hat{k} \end{bmatrix} \quad (B-6)$$

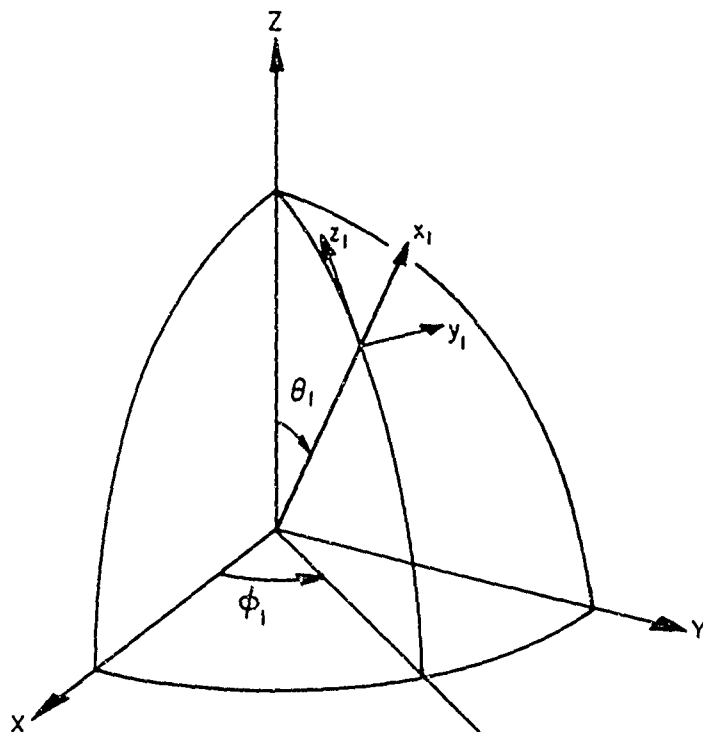


Figure B-2 The coordinate systems involved in the transformation of various vectors. (x, y, z) is an Earth centered system and (x_1, y_1, z_1) is centered at an observation site.

The unit vector \vec{t} along the line of sight from station 1 is given in (x_1, y_1, z_1) system in terms of the look angles as:

$$\vec{t} = \sin \beta_1 \hat{i}_1 + \cos \beta_1 \sin \alpha_1 \hat{j}_1 + \cos \beta_1 \cos \alpha_1 \hat{k}_1 \quad (B-7)$$

substituting Equation B-6 into B-7 leads to:

$$\begin{aligned} \vec{t} &= (\sin \beta_1 \sin \theta_1 \cos \phi_1 - \cos \beta_1 \sin \alpha_1 \sin \phi_1 \\ &\quad - \cos \beta_1 \cos \alpha_1 \cos \theta_1 \cos \phi_1) \hat{i} \\ &\quad + (\sin \beta_1 \sin \theta_1 \sin \phi_1 + \cos \beta_1 \sin \alpha_1 \cos \phi_1 \\ &\quad - \cos \beta_1 \cos \alpha_1 \cos \theta_1 \sin \phi_1) \hat{j} \\ &\quad + (\sin \beta_1 \cos \theta_1 + \cos \beta_1 \cos \alpha_1 \sin \theta_1) \hat{k} \\ &= a_1 \hat{i} + b_1 \hat{j} + c_1 \hat{k} \end{aligned} \quad (B-8)$$

\vec{J} , the unit vector from the second site, can be similarly expressed; replacing the subscript 1 in Equation B-8 by 2 one gets:

$$\vec{J} = a_2 \hat{i} + b_2 \hat{j} + c_2 \hat{k} \quad (B-9)$$

From Equation B-1

$$\vec{N} = \begin{bmatrix} \hat{i} & \hat{j} & \hat{k} \\ a_1 & b_1 & c_1 \\ a_2 & b_2 & c_2 \end{bmatrix} \begin{bmatrix} \vec{I} \times \vec{J} \end{bmatrix}^{-1} = N_1 \hat{i} + N_2 \hat{j} + N_3 \hat{k} \quad (B-10)$$

The vectors \vec{R}_1 and \vec{R}_2 are given in terms of the coordinates of the stations as

$$\vec{R}_1 = R_E \left[\sin \alpha_1 \cos \phi_1 \hat{i} + \sin \theta_1 \sin \phi_1 \hat{j} + \cos \alpha_1 \hat{k} \right] \quad (B-11)$$

$$\vec{R}_2 = R_E (\sin \theta_2 \cos \phi_2 \hat{i} + \sin \theta_2 \sin \phi_2 \hat{j} + \cos \theta_2 \hat{k}) \quad (B-12)$$

using Equations B-4, B-5, and B-8 to B-12, the position vector of the cloud can be expressed in the Earth centered coordinate system in the form:

$$\vec{x} = U \hat{i} + V \hat{j} + W \hat{k} \quad (B-13)$$

Where U , V and W are functions of the parameters θ_1 , θ_2 , ϕ_1 , ϕ_2 , α_1 , α_2 , β_1 and β_2 and can be calculated. If h , θ , and ϕ denote the altitude, latitude and longitude of the cloud position, they are given as:

$$h = (U^2 + V^2 + W^2)^{1/2} - R_E$$

$$\theta = \sin^{-1} (W(U^2 + V^2 + W^2)^{-1/2})$$

$$\phi = \tan^{-1} (V/U)$$

The method described here has been used to calculate the trajectory of the cloud shown in Figure 3-2.

ACKNOWLEDGMENTS

We are grateful to Dr. R.M. Jones and Mrs. Judith J. Stephenson of ESSA for supplying us with a FORTRAN deck of the 3D ray tracing program and the instructions to use it. We would like to thank Tom Boak for adapting the program to Univac 1108, Dave Blood for the help in preparing the section on experimental results and Bill Russell for the assistance at the time of publication.

REFERENCES

Crispin, Jr., J.W. and Maffett, A.L., RCS Calculation of Simple Shapes-Monostatic, P.83 in Methods of Radar Cross-Section Analysis edited by Crispin, Jr. J.W., and Siegel, K.M., Academic Press, New York, 1968.

Croft, T.A., Computation of HF Ground Backscatter Amplitude, Radio Science, 2, No. 7, 739, 1967.

Georges, T.M. and Stephenson, J.J., HF Radar Signatures of Travelling Ionospheric Irregularities, 3D Ray Tracing Simulation, Radio Science, 4, No. 8, 679, 1969.

Haerendel, G. and Lüst, R., Artificial Plasma Clouds in Space, Sci. Amer., 219, 81, 1968.

Haselgrove, J., Ray Theory and a New Method for Ray Tracing, Proceedings of the Conference on the Physics of the Ionosphere, Physical Society, London, P. 355, 1954.

Holway, Jr., L.H., Ambipolar Diffusion in the Geomagnetic Field, J. Geophys. Res., 70, No. 15, 3635, 1965.

Jones, R.M., A Three Dimensional Ray Tracing Computer Program, ESSA Technical Report IER17-ITSA17, 1966 (see also ESSA Technical Memorandum ERLTM-ITS134, 1968).

Jones, R.M., A Three Dimensional Ray Tracing Computer Program, Radio Science, 3, No. 1, 93, 1968.

Lemanski, T.J., An Evaluation of the ITSA 3-D Ray Trace Program, Radio Science, 3, No. 1, 95, 1968.

Minkoff, J.B., Calculation of Ion Inventories and Observations of Cloud Dynamics, In Report on Pre-SECEDE Experiments, Edited by Minkoff, J.B., Technical Report T-27/068-4-00, Riverside Research Institute, 1970.

Oetzel, G.N. and Chang, N.J.F., Analysis of SECEDE 111 HF Data, Technical Report 3, Contract F30602-68-C-0076, SRI Project 6851, Stanford Research Institute, Menlo Park, California, 1969.

REFERENCES

Crispin, Jr., J.W. and Maffett, A.L., RCS Calculation of Simple Shapes-Monostatic, P.83 in Methods of Radar Cross-Section Analysis edited by Crispin, Jr. J.W., and Siegel, K.M., Academic Press, New York, 1968.

Croft, T.A., Computation of HF Ground Backscatter Amplitude, Radio Science, 2, No. 7, 739, 1967.

Georges, T.M. and Stephenson, J.J., HF Radar Signatures of Travelling Ionospheric Irregularities, 3D Ray Tracing Simulation, Radio Science, 4, No. 8, 679, 1969.

Haerendel, G. and Lüst, R., Artificial Plasma Clouds in Space, Sci. Amer., 219, 81, 1968.

Haselgrave, J., Ray Theory and a New Method for Ray Tracing, Proceedings of the Conference on the Physics of the Ionosphere, Physical Society, London, P. 355, 1954.

Holway, Jr., L.H., Ambipolar Diffusion in the Geomagnetic Field, J. Geophys. Res., 70, No. 15, 3635, 1965.

Jones, R.M., A Three Dimensional Ray Tracing Computer Program, ESSA Technical Report IER17-ITSA17, 1966 (see also ESSA Technical Memorandum ERLTM-ITS134, 1968).

Jones, R.M., A Three Dimensional Ray Tracing Computer Program, Radio Science, 3, No. 1, 93, 1968.

Lemanski, T.J., An Evaluation of the ITSA 3-D Ray Trace Program, Radio Science, 3, No. 1, 95, 1968.

Minkoff, J.B., Calculation of Ion Inventories and Observations of Cloud Dynamics, In Report on Pre-SECEDE Experiments, Edited by Minkoff, J.B., Technical Report T-27/068-4-00, Riverside Research Institute, 1970.

Oetzel, G.N. and Chang, N.J.F., Analysis of SECEDE 111 HF Data, Technical Report 3, Contract F30602-68-C-0076, SRI Project 6851, Stanford Research Institute, Menlo Park, California, 1969.